A STUDY OF SMALL HEAT SHOCK PROTEINS STRUCTURE AND FUNCTION BY CRYO-ELECTRON MICROSCOPY

By

Jian Shi

Dissertation

Submitted to the Faculty of the

Graduate School of Vanderbilt University

in partial fulfillment of the requirements

for the degree of

DOCTOR OF PHILOSOPHY

in

Molecular Physiology and Biophysics
May, 2008

Approved:

Professor Albert H. Beth

Professor Roger J. Colbran

Professor Anne Kenworthy

Professor Charles R. Sanders, II

Professor Jens Meiler

DEDICATION

To my parents, SHI, DaoZhou and CHE, Lanyun

And my wife, HONG, Xin

ACKNOWLEDGEMENTS

I would like to express my sincere appreciation to my mentor, Dr. Phoebe Stewart, for leading me into the field of cryoEM, providing me the exceptional chance to work with state-of-the-art microscopes and supporting me throughout the graduate research. My graduate studentship has been an enjoyable and fruitful journey under her guidance. The work presented in this thesis would have not been initiated and accomplished without the enlightening ideas and unlimited support from my co-advisor, Dr. Hassane Mchaourab. I appreciate the feedback my thesis committee has given along the way, which has helped me to develop scientifically.

I am grateful to the fellow members of the Stewart Laboratory and Mchaourab Laboratory for their encouragement and practical assistance. Dewight's dedication to research set an excellent example for me. His critical comments on my writing and presentations were invaluable. I am grateful to GuanYong for teaching me protein purification step by step. I could not have completed the project in time without his help. I am thankful to Dr. Hanane Koteiche for her help with fluorescence experiments. Special thanks to other members in the laboratories and the MPB department, Susan Saban, Zheng Zhou, Jinghui Dong, Zhibo An, Steffen Lindert, Mariena Silverstry, whose friendship gave me the strength to move forward.

This work is dedicated to my parents, Shi, DaoZhou, Che, LanYun and my wife, Hong, Xin. Their endless love was, is and will be persistently inspiring me in pursuit of a meaningful life.

LIST OF FIGURES

Figure Page

Figure I-1 12
Figure I-2 13
Figure I-3 14
Figure II-1 26
Figure II-2 31
Figure II-3 34
Figure II-4 36
Figure III-1 51
Figure III-2 53
Figure III-3 55
Figure III-4 57
Figure III-5 59
Figure III-6 61
Figure III-7 64
Figure III-8 65
Figure III-9 68
Figure IV-1 80
Figure IV-2 84
Figure IV-3 88
Figure IV-4 89
Figure IV-5 92
Figure IV-6 93
Figure V-1 109
Figure V-2 112
Figure V-3 113
Figure V-4 115

Figure V-5 118

Figure V-6 121

TABLE OF CONTENTS

Page

DEDICATION ii

ACKNOWLEDGEMENTS iii

LIST OF FIGURES v

Chapter

I. INTRODUCTION TO SMALL HEAT SHOCK PROTEINS 1

1.1 Small heat shock proteins are part of a molecular chaperone network inside the cell 1
Brief history of the discovery of the heat shock response and molecular chaperones 1
Heat-shock protein families 3
Small heat shock proteins 4
1.2 Roles of small heat shock proteins in human disease 5
Cataracts 6
αB-crystallin in other human diseases 8
Hsp27 in human disease 9
1.3 The structure of small heat shock proteins 10
1.4 The mechanism of small heat shock protein function 16

II. INTRODUCTION TO THE CRYOELECTRON MICROSCOPY METHOD ... 21

2.1 A brief history of cryoelectron microscopy 21
Development of the electron microscope 21
Negative Staining 22
Sample preparation methods without staining 23
Problems in cryo-EM methods 24
2.2 Introduction to image formation in electron microscopy 27
Amplitude contrast 27
Phase contrast and phase contrast transfer function 28
CTF determination and correction 32
2.3 Introduction to three-dimensional image reconstruction theory 35
2.4 Materials and methods for experiments 39

III. CRYOEM AND EPR ANALYSIS OF ENGINEERED SYMMETRIC AND POLYDISPERSE HSP16.5 ASSEMBLIES REVEALS DETERMINANTS OF POLYDISPERSITY AND SUBSTRATE BINDING 45

3.1 Abstract 45
3.2 Introduction 46
3.3 Results 49
Flexible peptide insertions in Hsp16.5 lead to novel structural assemblies 49
CryoEM reveals a highly fenestrated and symmetrical structure for Hsp16.5-P1 52
Preservation of the dimeric building block in Hsp16.5-P1 54
A pseudoatomic model of Hsp16.5-P1 reveals two non-equivalent subunit positions 56
Validation of the Hsp16.5-P1 pseudoatomic model by SDSL-EPR 58
The C-terminal extension is a flexible tether that enables repacking 60
Plasticity at the dimer-dimer interface can lead to polydispersity 62
Oligomer expansion enhances substrate binding 66
3.4 Discussion 69
IV. INSIGHTS INTO THE MECHANISM OF SHSP CHAPERONE FUNCTION ARE REVEALED BY CRYO-ELECTRON MICROSCOPY AND SINGLE PARTICLE ANALYSIS 73
4.1 Introduction 73
4.2 Results 77
Hsp16.5-Truncation (TR) and Hsp16.5-TR/T4L complex 77
Hsp16.5-P1 and Hsp16.5-P1/T4L complex 81
Hsp16.5-WT and Hsp16.5-WT/T4L complex 85
Hsp16.5-R107G 90
4.3 Discussion 94
Enclosed substrate and dynamic oligomeric structure 95
Activation of sHSPs 97
V. SCRIPT ASSISTED MICROSCOPY (SAM) IMPROVES DATA ACQUISITION RATES ON FEI TECNAI ELECTRON MICROSCOPES EQUIPPED WITH GATAN CCD CAMERAS 101
5.1 Abstract 101
5.2 Introduction 102
5.3 Methods 105
5.4 Results 107
Strategy 107
Targeting 110
Image Acquisition 114
Calibration 116
Evaluation and Saving 117
Resolution Test 119
Efficiency 122
5.5 Discussion 123

VI. SUMMARY AND CONCLUSIONS 126
6.1 Review of the function and therapeutic potential of sHSPs 126
6.2 Mechanism of sHSPs function revealed by cryoEM.. 128
REFERENCES 133

CHAPTER I

INTRODUCTION TO SMALL HEAT SHOCK PROTEINS

1.1 Small heat shock proteins are part of a molecular chaperone network inside the cell

Brief history of the discovery of the heat shock response and molecular chaperones

Ferrucio Ritossa (Ritossa, 1964) observed that the chromosome puffing pattern of Drosophila salivary glands cell changed in response to elevated temperature, suggesting that overall gene expression patterns adopt to the stressors (Ritossa & Vonborstel, 1964). One decade later, Alfred Tisseres (Tissieres et al., 1974) observed a number of new protein bands from salivary glands tissue after heat shock treatment, indicating dramatically increased protein synthesis. Gerner *et al.* observed that the thermo-resistance of HeLa cell is improved after a short period of non-lethal hyper-thermal treatment, which is ascribed to the enhanced expression of a specific subset of genes (Gerner & Schneider, 1975). This adaptive response is now known as the heat shock response and exists in a wide range of organisms from Bacteria, Archaea and Eukarya. The stressors that induce the heat shock response include, but are not limited to, temperature increase, high or low pH and extreme osmolarity, oxidative reagents, DNA damage agents, heavy metals, as well as ethanol, and amino acid starvation. The products of the heat shock response are heat shock proteins, which are classified into two categories, molecular chaperones and proteases, based on their function (Ellis, 2007). To deliver thermal resistance to cells, molecular chaperones transiently bind non-native proteins to assist them in folding correctly, whereas proteases digest non-native proteins into peptides and amino acids for reuse in protein synthesis.

Proteins play a central role in cellular functions, and their intricate functions rely on correct three-dimensional folding and assembly. Anfinsen (Anfinsen, 1973) showed that protein three-dimensional folding is dictated by its linear amino acid sequence using ribonuclease renaturation experiments *in vitro*. During the translation process, the peptide chain starts to fold as soon as it emerges from the ribosome. Nevertheless, before the completion of the folding process, the partially exposed hydrophobic sites could form inappropriate contacts and generate adverse products. In addition, the crowded *in vivo* environment creates great competition of such unfavorable intermolecular interactions with the correct folding processes (Ellis & Minton, 2003). Extrinsic factors exist in cells to ensure productive protein folding and assembly. Laskey discovered that nucleoplasmin is required for the correct assembly of nucleosomes in reconstitution experiments with histones and DNA and invented the term “molecular chaperone” (Laskey et al., 1978). A protein named immunoglobin heavy-chain binding protein (BiP) was reported (Haas & Wabl, 1983) to prevent the aggregation of free heavy-chain and aid the assembly of immunoglobin without the interaction of light-chain. Based on cumulative evidence, Ellis RJ proposed a definition of ***molecular chaperone*** as: “a class of cellular proteins whose function is to ensure that the folding of certain other polypeptide chains and their assembly into oligomeric structures occur correctly, but they do not form part of the final structure nor do they necessarily possess steric information specifying assembly” (Ellis, 1987).

Heat-shock protein families

Heat shock and other stress conditions affect protein stability, i.e. the folding equilibrium, and as a consequence a higher proportion of proteins are found in unfolded states, leading to increased opportunity for aggregation. Being part of the exquisite protein quality control mechanism, molecular chaperones serve a common purpose that is to protect non-native proteins from unfavorable hydrophobic interactions and to assist them in folding correctly under physiological conditions as well as under adverse circumstances. Molecular chaperones fall into different families based on phylogeny, structure, molecular mass, and functions, which may or may not require ATP hydrolysis (Arrigo, 2007; Haslbeck, 2002). Many molecular chaperones are also heat shock proteins in that their expression is up-regulated by the heat shock response. The most extensively studied families include Hsp100, Hsp90, Hsp70, Hsp60, and small heat shock proteins (Narberhaus, 2002).

The DnaK chaperone system in *E. coli*, which is composed of the well-studied Hsp70 family members DnaK, DnaJ, and GrpE, binds nascent peptides emerging from the ribosome through the stimulation of ATP-hydrolysis and allows folding of non-native proteins during several cycles of binding and releasing (Young et al., 2004). In eukaryotes, Hsp70 alone can bind non-native proteins but requires co-chaperone Hsp40 for substrate folding, as well as modulators for positive or negative regulation of activities (Young et al., 2004). As representative of the Hsp60 family, the GroEL/GroES system in *E. coli* draws much interest from researchers. GroEL forms a back-to-back double-ring structure, consisting of seven subunits and a central secluded chamber for each ring (Radford, 2006). The co-chaperone GroES is a heptameric ring-like lid and binds to the opening of GroEL to close the cavity. Through cycles of ATP hydrolysis and GroES binding, GroEL attracts non-native protein into one of its two cavities and allows the protein to fold into its native state. This process can be iterated as many times as necessary for completion of the correct folding of a non-native state substrate (Tang et al., 2006). Hsp100 family members (Clp) in prokaryotes are similar to GroEL in structure, which consists of a ring of subunits and an interior cavity. Hsp100 family members function as chaperones as well as proteases and target protein aggregates instead of unstable aggregation-prone states of proteins (Bukau et al., 2006; Horwich, 2004). Among the heat shock protein families, Hsp90 chaperones are the most constitutively abundant in the cytosol, nevertheless they can be further up-regulated under stress conditions. The housekeeping function of Hsp90 is exemplified by the competent conformation of the steroid hormone receptor held by the association of Hsp90 and co-chaperones (Caplan et al., 2007).

Small heat shock proteins

Small heat shock proteins (sHsps) are named due to their small monomeric molecular mass (12-40 kDa), but physiologically they exist as large oligomers consisting of 4 to 40 subunits. SHsps are the most widespread molecular chaperones throughout all kingdoms, and their expression is most up-regulated upon heat shock, manifesting their essential role in maintaining cell homeostasis under adverse conditions (de Jong et al., 1998; Haslbeck et al., 2005). SHsps share a loosely conserved region of ~90 residues close to their C-termini, named the α-crystallin domain, but their flanking N-termini and C-termini are variable in sequence and length (Kappe et al., 2003). The interaction between sHsps and non-native state protein substrates is characterized by substrates promiscuity, high capacity, and ATP-independence (Haslbeck et al., 2005). The heat shock exerts damage to cellular proteins on a non-discriminative basis, and the degree of damage increases exponentially with the harshness of the stress. ATP becomes a limited resource because of both greater demand and reduced production due to decreased enzymatic activity. Therefore, the properties of sHsps enable them to be the major driving force in maintaining order of cellular components. We may regard the sHsps as a dam in the cell controlling the flood of unfolded proteins, providing a reservoir of re-foldable proteins, which can be revived by other ATP-dependent molecular chaperone machineries when the conditions permit. The dysfunction of sHsps in the cell is associated with the pathology of human diseases, particularly diseases due to protein folding problems.

1.2 Roles of small heat shock proteins in human disease

A broad range of human diseases are associated with problems in protein folding. Alzheimer's, Huntington's, and prion diseases are characterized by amyloid aggregates, and Amyotrophic Lateral Sclerosis, Parkinson's disease, and cataracts are associated with amorphous protein aggregates. Such protein aggregation diseases may share similar molecular mechanisms of pathogenesis and cell damages. For instance, the toxic oxidative free radicals generated by protein amyloids are implicated to be common in the pathology of several different neurodegenerative diseases (Tabner et al., 2005). Avoiding, slowing, or reversing such protein aggregate formation through boosting cellular protein control system, including molecular chaperones, ubtiquitination enzyme and proteasomes, may hold therapeutic potential for these diseases (Bucciantini et al., 2002; Kayed et al., 2003). Therapeutic strategies that are designed for one disorder may also be applicable to other diseases sharing common mechanism of pathogenesis.

Cataracts

The most common human disorder related to sHsps is cataracts in the eye lens, a leading cause of blindness worldwide. The cytosolic protein concentration in a lens fiber cell is about 400mg/ml, almost double than that of somatic cells. The predominant proteins in lens fiber cells are α, β, and γ crystallins (>90%), which are highly stable and water-soluble. The short-range, liquid-like interactions of highly concentrated crystallins greatly reduces light scattering and renders the transparency and refractivity of lens (Bloemendal et al., 2004). Because lens fiber cells lose all cellular organelles during development, there is no protein turn over in lens fiber cells due to loss of ribosomes. To ensure a normal, clear lens, the lens crystallins have to be kept free from denaturation and aggregation throughout the lifetime of the individual. Protein post-translation modifications, such as deamidation, oxidation, glycation, truncation, and phosphorylation, happen to lens proteins with aging and disrupt their solubility (Harding, 2007; Truscott, 2007). Over time, these modifications lead to progressive protein aggregation in the lens, which results in cataracts due to increasing light scattering and lens opacity. Thus, it is easy to understand that cataract is typically prevalent in the elderly population (Bloemendal et al., 2004). The World Health Organization estimates that 18 million people are blind from cataracts (http://www.who.int). Currently the only effective treatment of cataract is lens surgery, a procedure that accounts for 12% of the entire Medicare budget in the United States (http://www.ncbi.nlm.nih.gov).

Identified as a member of sHsp family, α-crystallin maintains the solubility of lens proteins as well as plays a role as a structural protein, representing approximately one third of the total protein in the human lens (Horwitz, 1992; Ingolia & Craig, 1982). The biological functions of β and γ-crystallin remain unclear. The human α-crystallins are hetero-oligomers, composed of two homologous polypeptides, αA-crystallin and αB-crystallin. They share 57% sequence homology and present in the lens at a molar ratio of 3:1 (Horwitz et al., 1999). Human αA-crystallin is only found in the lens, whilst αB-crystallin is also expressed in the heart, skeletal muscle, and kidney and its expression can be enhanced by stressors. Late-onset cataracts normally results from cumulative damage to lens proteins following post-translational modifications and exposure to environmental stressors, such as ultraviolet radiation, smoking, and oxidative agents. Cataracts could be associated with complications of chronic diseases, such as diabetes and/or hypertension, which cause modifications (glycation and/or truncation) of lenticular α-crystallin (Harding, 2007; Thampi et al., 2002). It is suggested that impaired chaperone function of α-crystallin contributes to the general mechanism of cataract progression (Horwitz, 2003).

Cataracts can also be congenitally acquired due to loss or mutation of α-crystallin. At present, several cataractogenic mutations have been identified in αA-crystallin (W9X, R49C, G98R, and R116C) and αB-crystallin (Δ450A, D104N and R120G) (Andley, 2006; Singh et al., 2006). Most of them are dominant mutations and interfere the chaperone activity of α-crystallin (Andley, 2006). The αA-crystallin knockout mouse is born with cataract, and is characterized by inclusion bodies of αB-crystallin (Brady et al., 1997). The absence of αB-crystallin in the mouse causes progressive muscular dystrophy rather than the cataract phenotype (Brady et al., 2001). Double knockout of both αA-crystallin and αB-crystallin results in abnormal fiber cells during lens development, suggesting other cellular functions of α-crystallin in addition to protein protection (Boyle et al., 2003). The pathogenesis of cataract result from R116C mutation of αA-crystallin has been proposed to be related to enhanced binding ability to substrates (Koteiche & Mchaourab, 2006).

αB-crystallin in other human diseases

Beside its maintenance role in the lens, αB-crystallin is expressed in other tissues and plays physiological roles under normal and pathological conditions. αB-crystallin is known to be a key element of the tubulin quality control system and affects the cytoskeletal assembly and disassembly equilibrium through the interaction with microtubule association proteins (MAPs) (Ghosh et al., 2006). The expression pattern of αB-crystallin in heart muscle cells is coincident with that of desmin, an intermediate filament protein, during embryo development (Goldfarb et al., 2004). The cataractogenic αB-crystallin R120G mutation is also related to desmin-related cardiomyopathy (DRM) (Vicart et al., 1998), which is characterized by late-onset accumulation of aggregates containing both desmin and αB-crystallin. The pathology of DRM may be related to cytoskeletal defects, changes in the architecture of mitochondria, and heart failure caused by the mutant αB-crystallin expression (Maloyan et al., 2005) and/or hyperphoshorylation of αB-crystallin (den Engelsman et al., 2005). In addition, αB-crystallin is also found in the inclusion bodies, Rosenthal fibers, and Mallory bodies in neurodegenerative disorders (Liu et al., 2004; Maloyan et al., 2005; Mehlen et al., 1996; Narberhaus, 2002). Evidence suggests that αB-crystallin is a negative regulator of apoptosis and its over-expression in certain cancer cells renders resistance to therapeutic agents and thus poor prognosis (Arrigo et al., 2007; Sun & MacRae, 2005a). One recent experiment shows that over-expression of αB-crystallin, but not its phosphorylation mimics, could transform mammary epithelia cells to invasive carcinomas in nude mice, meeting the standard of an oncogenic protein (Moyano et al., 2006).

Hsp27 in human disease

Another widely studied human sHsp is Hsp27, which is involved in a variety of cellular activities, from apoptosis, cytoprotection, to tumorgenesis (Kappe et al., 2003). Hsp27 expression is normally low, but constitutively high in certain cancer cells. Over-expression of Hsp27 contributes to thermo-tolerance of the cell and oxidative stress resistance as well as resistance against apoptotic and necrotic factors (Latchman, 2005). The molecular mechanisms that underlie Hsp27's protective functions may include stabilization of cytoskeletal components (Quinlan, 2002), inhibition of apoptotic signaling pathway (Arrigo et al., 2002), and inhibition of caspase-3 activation (Bruey et al., 2000). Such protective functions allow Hsp27 to potentially play therapeutic roles (Arrigo, 2007), especially in neuronal and cardiac cells. Furthermore, its expression in cancer cells may be utilized as a biomarker for cancer diagnosis and prognosis of chemical treatment (Ciocca & Vargas-Roig, 2002). Experiments show that the quaternary structure and chaperone activities of Hsp27 are regulated through phosphorylation (Koteiche & Mchaourab, 2006; Shashidharamurthy et al., 2005).

1.3 The structure of small heat shock proteins

Most sHsps form large oligomeric structures under physiological condition, with 9 to 50 subunits per assembly (Haslbeck et al., 2005). Because of the unique and prolonged solubility and stability of α-crystallins over decades, numerous studies have focused on the structural properties of α-crystallin. The major structural techniques applied to the study of α-crystallin include X-ray crystallography, cryo-electron microscopy (cryoEM) and single particle reconstruction, electron paramagnetic resonance (EPR) spectroscopy, nuclear magnetic resonance (NMR) spectroscopy, fluorescence spectroscopy and mass spectroscopy (Carver, 1999; Haley et al., 2000; Kim et al., 1998a; Koteiche & Mchaourab, 1999; Sathish et al., 2003; Van Montfort et al., 2001a). Up to date, only a few structures of small heat shock proteins are available, including Hsp16.5(24mer) from *Methanococcus jannaschii,* a hyperthermophilic archaeon (Kim et al., 1998a), Hsp16.9(dodecmer) from wheat (van Montfort et al., 2001b), Tsp36(tetramer) from parasitic worm (Kappe et al., 2004), Arc1(Hsp16.3, dodecmer) from *Mycobacterium tuberculosis,*(Kennaway et al., 2005) and Hsp26(24mer) from *Saccharomyces cerevisiae* (White et al., 2006). The structures of Hsp16.5, Hsp16.9, and Tsp36 were determined by X-ray crystallography. The structures of Arc1 and Hsp26 were generated by electron microscopy and three-dimensional image reconstruction. In general, these oligomers are hollow sphere-like and N-terminal regions reside inside the central cavity and C-termini extend outward toward solvent. The mammalian members of the sHsp family, including human α-crystallin, have not yet been crystallized presumably because they form polydisperse oligomers.

Crystal structures of Hsp16.5 and Hsp16.9 reveal that the α-crystallin domain fold is highly conserved, despite less than 25% sequence identity, and is composed of two layers of three to five anti-parallel β-strands, forming a compact β-sheet sandwich similar to the immunoglobulin fold. Using site-directed-spin-labeling (SDSL) (Koteiche & Mchaourab, 1999) and EPR, Mchaourab et al. have shown that the α-crystallin domain of αA-crystallin also has predominantly a β-sheet fold. Two monomers form a dimer, which is the building subunit of oligomer and a common feature throughout the sHsps family. Subsequently, the dimers form an oligomer through the interaction of a hydrophobic patch on the α-crystallin domain and conserved residues on the C-terminus of another subunit (Van Montfort et al., 2001a). The N-terminal region is highly variable and is generally hydrophobic. In the Hsp16.5 crystal structure, the N-terminal region (32 residues) remains unresolved, suggesting a disordered conformation, whereas 6 of the 12 N-termini in Hsp16.9 oligomer are resolved, and contain α-helix-rich secondary structures (Kim et al., 1998a; Van Montfort et al., 2001a). By combining cryo-electron microscopy (cryo-EM) density map modeling and SDSL-EPR spectroscopy, a portion of the Hsp16.5 N-terminal region was shown to have an α-helical conformation (Koteiche et al., 2005).

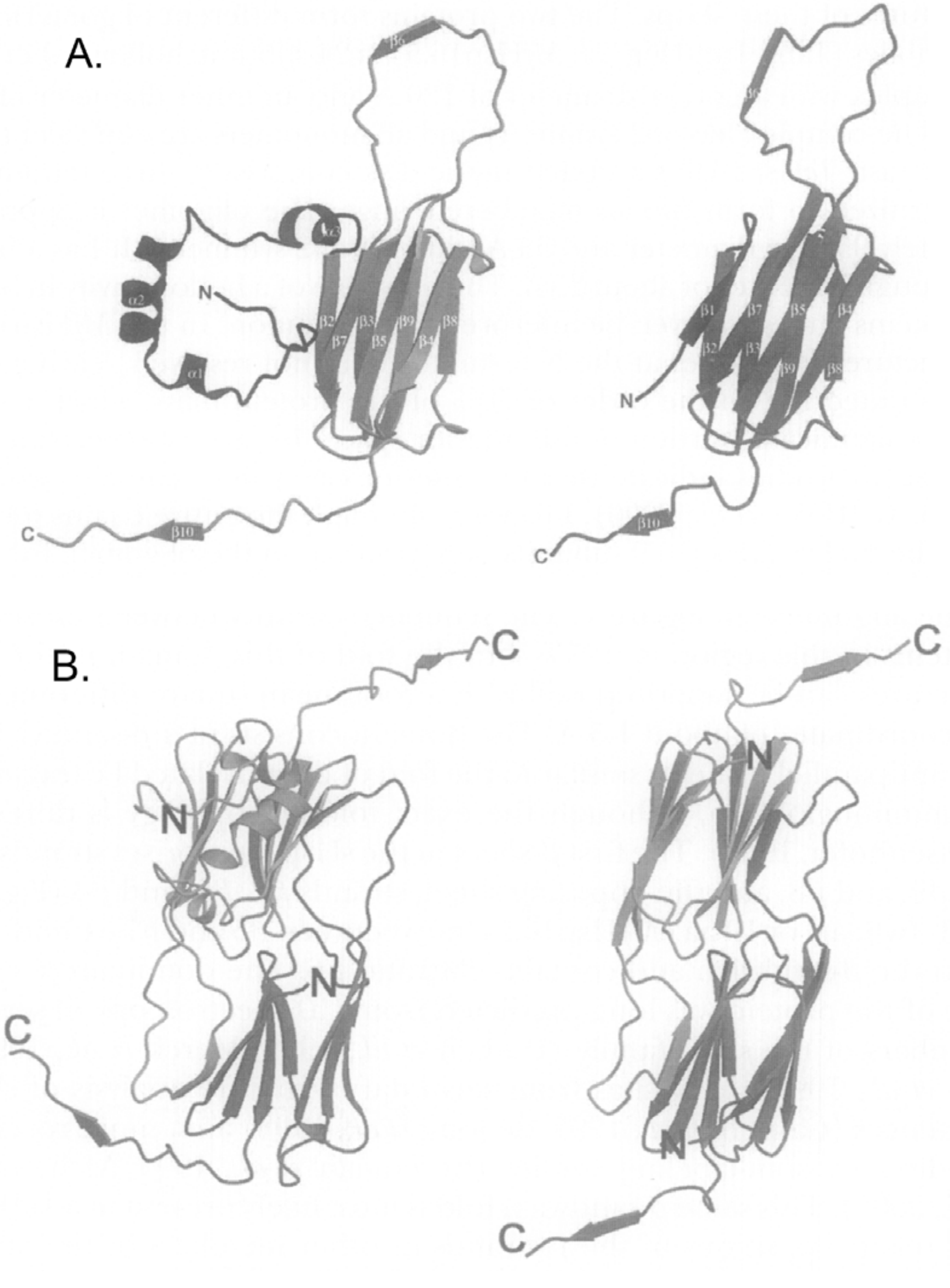

Figure I-1

(A) Comparison of the monomer structure of Hsp16.9 (left) and Hsp16.5 (right). The structure of Hsp16.9 is complete, while the N-terminal 32 residues of Hsp16.5 are disordered and not shown. (B) Comparison of dimer structure of Hsp16.9 (left) and Hsp16.5 (right). Reprinted with permission from (Van Montfort et al., 2001a)

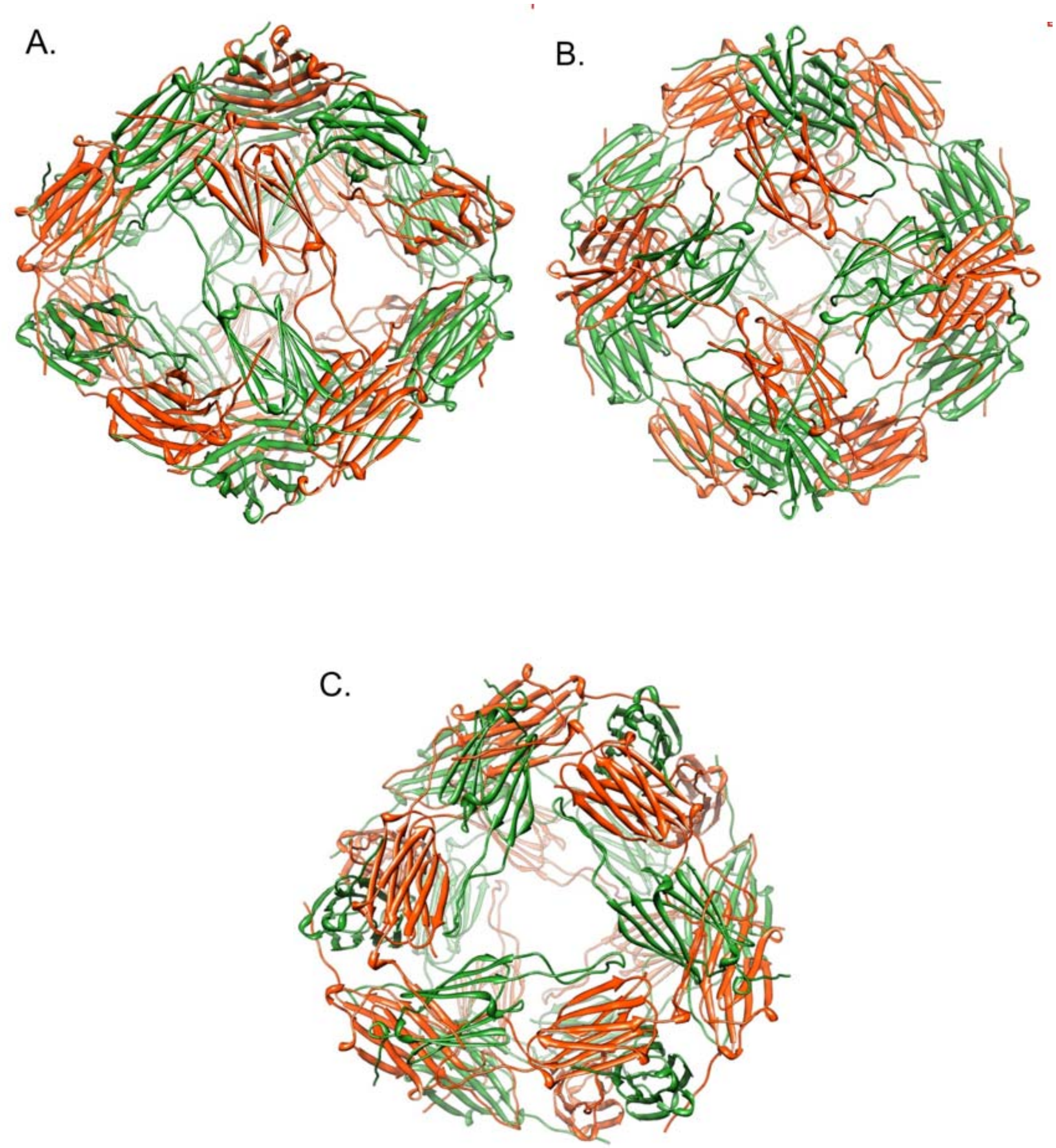

Figure I-2

The X-ray crystal structures of Hsp16.5 oligomer, which is formed by 24 monomers, i.e. 12 dimers, in octahedral symmetry (432). The structure is displayed along (A) 2 fold, (B) 4fold, (C) 3fold symmetrical axis. This figure is made in Chimera and the PDB code is 1SHS (Kim et al., 1998a).

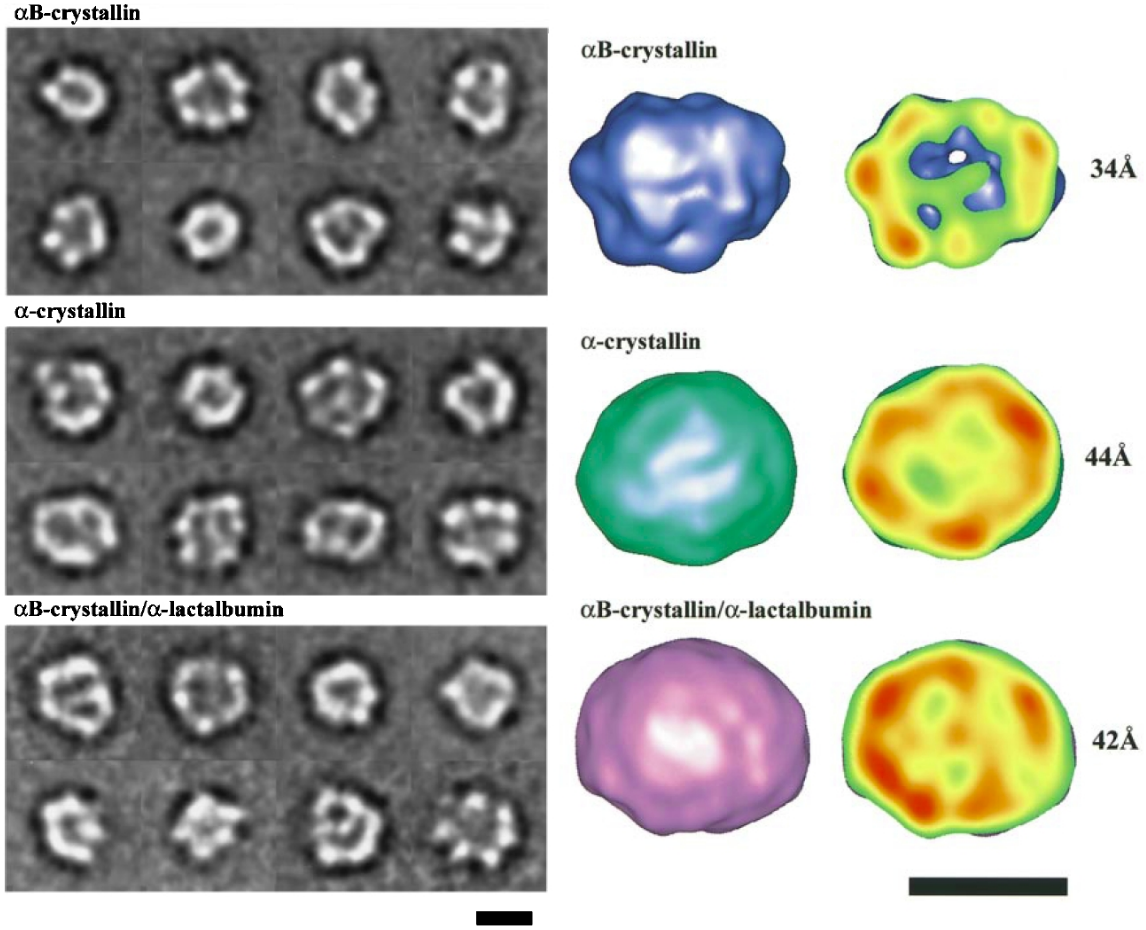

Figure I-3

Class-sum images (left) and 3D reconstructions (right) of aB-crystallin, native a-crystallin, and aB-crystallin with bound a-lactalbumin. All three a-crystallin assemblies display greater variability in size and shape and the resolution of each reconstruction is estimated by Fourier shell correlation (FSC). The two scale bars both represent 100 Å. Reprinted with permission from (Haley et al., 2000)

In contrast to monodisperse Hsp16.5 and Hsp16.9 oligomers, mammalian sHsps, such as αB-crystallin, form variable and dynamic assemblies (Haley et al., 2000), although biophysical studies (de Jong et al., 1998; Koteiche et al., 1998) suggest that their α-crystallin domains adapt similar β-sheet folding. The polydispersity of mammalian sHsps precludes them from being crystallized for X-ray crystallography studies and from yielding high resolution reconstruction by cryo-EM and single particle analysis (Haley et al., 2000; Haley et al., 1998). The lack of high-resolution structural information on polydisperse mammalian sHsps remains as the main obstacle towards understanding the mechanism of their quaternary structure formation and molecular chaperone functions.

Based on analysis of the sHsp sequence divergence, Mchaourab's lab reported that a 14-residue sequence of human Hsp27 (named P1), at the junction between the N-terminal region and the α-crystallin domain, contributes to the oligomeric equilibrium of Hsp27 (Shashidharamurthy et al., 2005). To investigate the structural regulatory role of this specific sequence, the P1 sequence was introduced into the Hsp16.5 N-terminal sequence at two positions: one after residue E12 (named Hsp16.5-P1N) in middle of the N-terminal region and the other after residue T33 (named Hsp16.5-P1) at the junction between the N-terminal and α-crystallin domains. The oligomeric state of Hsp16.5 is perturbed by inserting P1 sequence from human Hsp27. Hsp16.5-P1 forms a monodisperse oligomer with a molecular mass twice that of wild type, while Hsp16.5-P1N forms polydisperse oligomers. Another variant of Hsp16.5 is a truncation mutant (named Hsp16.5-TR) formed by removing the N-terminal 33 residues. We are combining two biophysical approaches, cryoEM with single particle analysis and EPR spectroscopy with site-directed spin labeling (SDSL), to study the structures of various forms of

Hsp16.5. **Our hypothesis is that by studying variants of Hsp16.5 we will gain insight into the mechanism of human sHsps oligomer formation and function.**

EPR analysis has shown that deleting the N-terminal 33aa of Hsp16.5 (Hsp16.5-TR15) produces an assembly similar to wild type (Koteiche & Mchaourab, 2002), which is confirmed by the cryoEM reconstruction in Aim1. The oligomeric structures of Hsp16.5-P1 and Hsp16.5-TR are determined to a resolution of 10Å and 12Å respectively by cryo-EM reconstruction. Cryo-EM class-sum images were also generated for the polydisperse Hsp16.5-P1N variant. The Hsp16.5-P1 cryo-EM density map was interpreted by docking the X-ray crystal structure of the α-crystallin domain from Hsp16.5-WT as guided by the residue specific information from EPR experiments in Dr. Mchaourab's lab. Consequently, a pseudo-atomic model with 48 copies of the α-crystallin domain was built for the Hsp16.5-P1 oligomer. The cryoEM and SDSL-EPR analysis of Hsp16.5-P1 and Hsp16.5-P1N reveals the structural basis of oligomer plasticity within small heat-shock proteins. The binding characteristics of the Hsp16.5 variants for model substrate proteins, T4 lysozyme (T4L) mutants, are studied by a fluorescence assay. Our results indicate that polydispersity is associated with enhancement of binding.

1.4 The mechanism of small heat shock protein function

The human α-crystallin was shown to function as a molecular chaperone that suppresses substrate aggregation induced by high temperatures, in addition to its known function as a lens structural protein (Horwitz, 1992). Compared to other Hsp families, sHsps protect a wide range of proteins from aggregation efficiently. The maximum binding capacity can reach one denatured protein molecule per subunit of the sHsp oligomer (Koteiche & Mchaourab, 2006; Mchaourab et al., 2002). The sHsp and substrate complex is soluble and stable, generally larger than the sHsp oligomer without substrate. The sHsps usually do not require energy input for binding action and do not promote the refolding of substrates. The substrate molecules in sHsp complexes can be effectively refolded in the presence of Hsp70 and ATP (Arrigo, 2007; Nakamoto & Vigh, 2007; Narberhaus, 2002). However, the chaperone function of sHsp is not fully understood mechanistically.

Biophysical and biochemical studies suggest that sHsps are able to recognize an early stage of unfolded proteins and that the bound substrates are folding-competent (Das et al., 1999; Das et al., 1996; Ehrnsperger et al., 1997; Lee et al., 1997; Lindner et al., 2001; Sathish et al., 2003). It is generally accepted that hydrophobic contacts underlie the recognition and binding of unfolded proteins by sHsps. Deletion of the N-terminal region, which is rich in hydrophobic residues, causes the dissociation of α-crystallin to smaller multimers but deletion of the N-terminal region of Hsp16.5 does not block formation of an oligomer with 24 subunits. Nevertheless both deletion mutations of α-crystallin and Hsp16.5 possess diminished chaperone activities, and little effects on secondary structures (Koteiche & Mchaourab, 2002; Kundu et al., 2007; Studer et al., 2002). Substrate interaction sites have been mapped with the α-crystallin domain as well, include β-strands #3, 8, 9 (Ghosh et al., 2005; Ghosh et al., 2006; Sharma et al., 1998a; Sharma et al., 1998b). A well conserved I-X-I/V motif in the C-terminal region of sHsps is responsible for the interaction of neighboring subunits at the hydrophobic groove between β-strand 4 and 8 and this interaction stabilizes the oligomer (Kim et al., 1998a;

Van Montfort et al., 2001a). The C-terminal region is enriched in hydrophilic residues that contribute to the solubility of sHsp oligomers and sHsp-substrate complexes. Disruption of C-terminus of sHsp by deletion or mutation reduces the chaperone activity (Bova et al., 2000; Li et al., 2007; Thampi & Abraham, 2003).

sHsps exhibit similar functions but constitute a continuum of quaternary structure, from poly-disperse to mono-disperse assemblies, and with different symmetry (Haley et al., 2000; Shi et al., 2006). In addition, sHsp oligomers are dynamic in response to aging, temperature, pH, ionic strength, and protein concentration. Subunit exchange constantly occurs between oligomers, which may contribute to substrate binding by increasing accessibility to buried hydrophobic regions (Bova et al., 1997; Bova et al., 2002). Elevated temperatures normally enhance the subunit exchange rate and chaperone activity. As an extreme case, Hsp26 completely dissociates from an oligomer to dimers at elevated temperatures and re-oligomerizes with substrate to larger complexes more than 3 times bigger (Haslbeck et al., 1999). An additional regulatory mechanism for mammalian sHsps is phosphorylation on serine residues, which occurs rapidly when cells are exposed to stress, cytokines, and growth factors (Butt et al., 2001). Phosphorylation alters sHsp assembly equilibrium, sometimes transforming large oligomers to tetramers or dimers, and regulates chaperone activities (Koteiche & Mchaourab, 2003; Shashidharamurthy et al., 2005).

The molecular mechanism of sHsp chaperone function remains elusive due to the diversity of sHsp structure, experimental conditions, and model substrates. The chaperone activity of sHsps typically is estimated by measuring the changes in light scattering of a solution or the recovery of enzymatic activity of substrate proteins, when substrate proteins are incubated with or without the presence of sHsps after heat or denaturants treatments (Reddy et al., 2006; Sun & MacRae, 2005b). The Mchaourab lab has developed a steady state assay for quantitative assessment of sHsp binding to substrates at physiological temperatures using a set of engineered T4 lysozyme mutants as model substrates, whose unfolding free energies range from 5 to 10 kcal/mol (Mchaourab et al., 2002). The quantitative analysis suggests that sHsps have two binding modes: a high-affinity binding mode and a low-affinity binding mode, which are proposed to correlate to different unfolding states of T4 lysozyme substrate (Koteiche & Mchaourab, 2003). In this context, the malfunction of cataractogenic αA-crystallin mutation (R116C) is explained as enhanced binding ability (Koteiche & Mchaourab, 2006), which leads to mis-regulated protein aggregation control and opacification in the lens.

The understanding of molecular mechanisms of cataracts will provide critical information that leads to new therapeutic measures. **We hypothesize that a mechanistic molecular model of sHsps can be inferred by analyzing the oligomeric structures of the complexes of Hsp16.5 variants and T4 lysozyme substrate.** Aim2 is to observe the structural changes of Hsp16.5 variants upon substrate binding by cryo-EM and to develop a mechanistic understanding of sHsp chaperone activity. Our data show Hsp16.5-WT homogenous assemblies are transformed into a continuum of oligomeric states upon T4L substrate binding. The Hsp16.5TR-T4L complex structure suggests that its oligomeric shell, which is formed by 24 copies of the α-crystallin domain, is able to bind substrate. Limited contact between the shell and T4L is unobservable at the current resolution. Binding of T4L to Hsp16.5-P1 and Hsp16.5-WT induces a conformational change in the

N-terminal region. We conclude that both the α-crystallin domain and N-terminal region serve to stabilize the substrate inside the sHsp oligomer and that the adaptable oligomeric state of sHsps contributes to substrate binding. Furthermore, we observe conformational changes in the N-terminal region in the Hsp16.5-R107G mutant by cryo-EM reconstruction, suggesting that it may represent an activated state even without substrate.

CHAPTER II

INTRODUCTION TO THE CRYOELECTRON MICROSCOPY METHOD

2.1 A brief history of cryoelectron microscopy

Development of the electron microscope

In 1927, Hans Busch, a German physicist, theorized that a symmetrical magnetic field could act as a lens for electrons like a convex glass lens for light. In 1930, Ernst Ruska designed an electron magnetic lens for his thesis project and proved that Busch's theory was correct. Ruska and Knoll built the first instrument to demonstrate electron imaging with a magnification factor of 14X in 1931. Ruska later admitted that they had not known the theory of wave-particle duality proposed by Louise De Broglie in early 20's until that summer (Ruska, 1986). The theoretical resolution limit of the light microscope, which is due to the wavelength of visible light, was not exceeded until 1933 with an improved electron microscope. The wavelength of the accelerated electrons in a modern electron microscope ranges from 1/10 to 1/100 of an Angstrom. However the resolution of an electron microscope is largely limited by the spherical and chromatic aberration of the electron magnetic lenses (Batson et al., 2002). All electron magnetic lenses are convex lenses, which have inherent spherical aberration that is difficult to correct without concave-type electron magnetic lens. Chromatic aberration results from the energy spread of an electron beam, which is due to coherence of electron sources and the energy loss after the interaction between electron beam and specimen. Nowadays, an aberration-corrected transmission electron microscope with resolving power of 0.5 Angstrom is commercially available (FEI Company, Titan^{TM} family).

As the primitive electron microscope was developed, the application of electron microscopy to biological science was also initiated, mostly by Ruska's brother Helmut Ruska, a medical scientist (Ruska, 1986). After several decades of improvement in electron microscopes and sample preparation techniques, electron microscopy began to have a profound impact on biological science. The resolving power of the electron microscope allowed the direct observation of a wide variety of biological structures ranges from whole bacteria cells, bacteriophages, virus, cell organelles and cell architectures, and biological macromolecules, such as DNA, ribosomes, and protein assemblies. The resolution of electron microscopy is far-beyond that of light microscopy. The possible observation by EM ranges from the cellular to the molecular level and bridges the scale gaps between X-ray crystallography and light microscopy. A number of EM sample preparation techniques have played important roles in the study of biological macromolecular machines.

Negative Staining

The negative staining method was proposed and widely used beginning in the 1960s (Harris, 1997). In this method, a specimen solution is mixed with heavy metal salt and is air-dried on a carbon-coated EM grid. The heavy metal ions surround the macromolecules and support the structure, resulting in images with high contrast. However, artifacts like partial staining and specimen flattening are almost inevitable, and the biological specimens are not preserved in their native environment. Therefore, the interpretation of the 2D images and 3D reconstructions from the negative staining technique should be accepted with caution. Nevertheless, negative staining remains a rapid and easy way to characterize a specimen and gain an initial model (Ohi et al., 2004). An alternative improved method, cryo-negative staining, has been proposed and used for a variety of biological specimens, and it takes advantages of the high contrast of stain while preserving a native-like hydration environment (De Carlo et al., 2002; El-Bez et al., 2005). More research is needed to demonstrate whether this method is capable of delivering sub-nanometer (< 10Å) resolution structures.

Sample preparation methods without staining

In order to observe specimens in an unstained hydrated state, Taylor and Glaeser (Rajasekaran et al., 2007) froze unstained catalase crystals in liquid nitrogen without a cryoprotectant. The resulting electron micrographs showed information up to 3.4Å in the electron diffraction pattern. However, for non-crystallin specimens, the formation of ice crystal during sample freezing can damage their three-dimensional structure. It was relatively recently (Bruggeller & Mayer, 1980) that the act of vitrifying water (producing ice without crystal formation) was successfully demonstrated. In this experiment micro-liter amounts of water were frozen very quickly (10^5 to 10^6 Ks^{-1}). Subsequently, the Dubochet group developed a simple, rapid and inexpensive method for preparing native specimens “frozen” in vitrified ice (Adrian et al., 1984). First, a thin layer of specimen in solution is formed on a hydrophilic supporting film, e.g. holey carbon film, by applying a micro-liter droplet of the sample solution and removing the excess with filter paper. Then, vitrification of the specimen is achieved by plunging into a cryogen with a high heat capacity, such as liquid ethane or propane. During the transfer into the electron microscope and observation, the specimen has to be maintained below the devitrification temperature (Td~140K). The preservation and protection of high-resolution biological structures in the frozen-hydrated state was demonstrated with a variety of specimens, including adenovirus, T4 bacteriophage and catalase crystals (Adrian et al., 1984; McDowall et al., 1983). Cryoelectron microscopy combined with single-particle reconstruction has become a powerful method to determine structure, since it does not require protein crystals, or large amounts of concentrated sample as needed for X-ray crystallography and NMR respectively. This method can be applied to a wide range of biological specimens, from ~200 kDa proteins to multi-subunit biological complexes and 100+ MDa viruses (Elad et al., 2007; Ohi et al., 2004; Saban et al., 2006). The specimen structure can also be determined in various functional conformations (Endres et al., 2006; Schaffitzel et al., 2006). During last twenty years, the applications of cryoEM have increased exponentially in the literature of structural biology (Chiu et al., 2006) and the resolution of various 3D reconstructions have approached ~4Å (Ludtke & Zhou, 2007; Yonekura et al., 2003).

Problems in cryo-EM methods

Nevertheless, the vitrification method and cryo-EM is not free of problems. Biological specimens in vitreous ice are extremely sensitive to radiation damage caused by inelastically scattering electrons, although the low temperature in cryoEM already provides some protection. This radiation sensitivity limits the applicable electron dose for high-resolution studies below the 10-20 $e^-/Å^2$ range. Therefore, the resulting cryo-electron micrographs contain an extremely low signal to noise ratio (SNR). Another intrinsic difficulty is the inherently low contrast of images because of the small difference in scattering power between the biological specimen and the surrounding water molecules. Recording defocused images gains extra phase-contrast, but also introduces complications to the image interpretation and 3D reconstruction, as discussed in the next section. We need to understand the image formation process in EM and apply computational corrections in order to interpret the structural information from noisy cryoelectron micrographs.

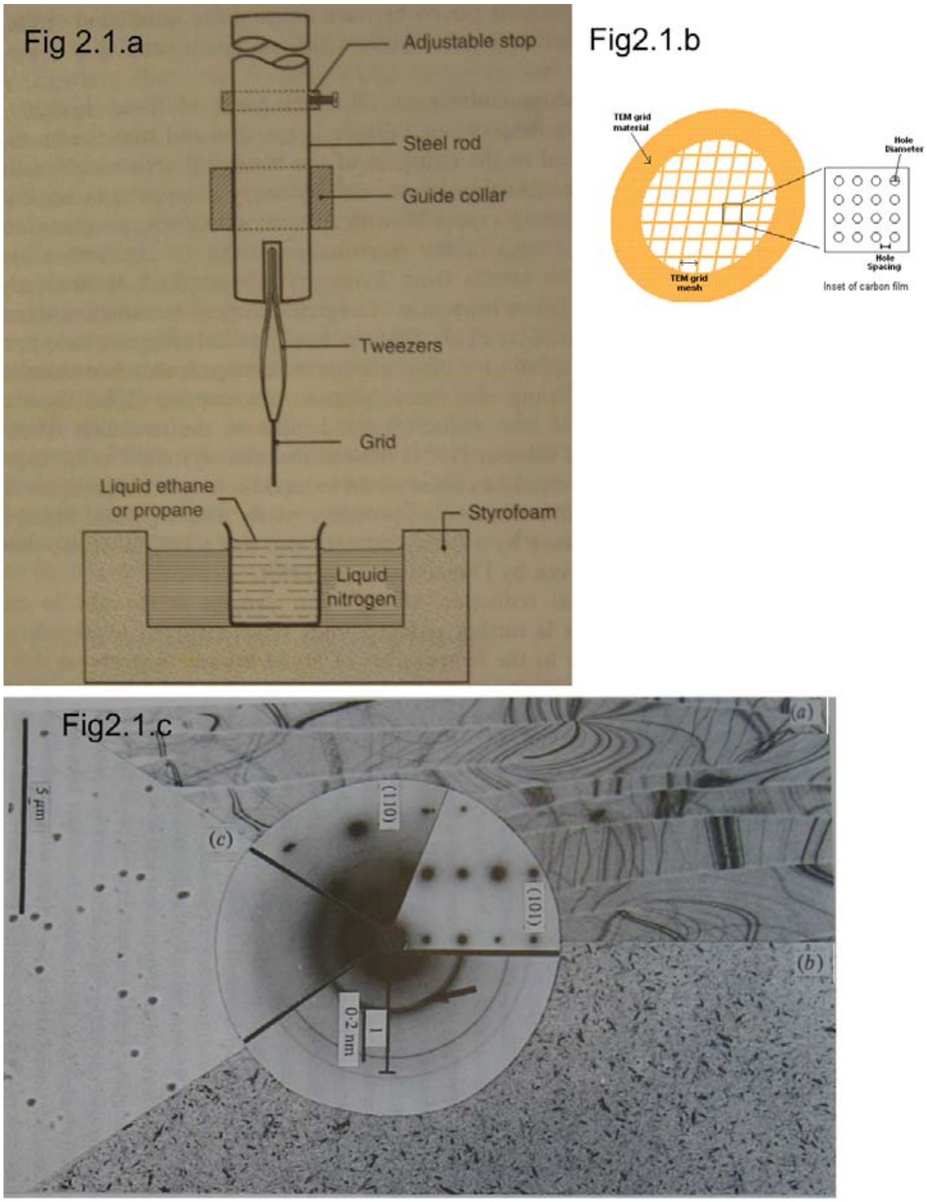

Figure II-1

(a) *This figure shows a scheme of a cryo-plunger Reprinted with permission from (Frank, 2006). The EM-grid* **(b)** *is clamped on the tip of tweezers; at the bottom is a double compartment container for liquid ethane or propane cooled by liquid nitrogen. The success rate in producing cryo-EM grids strongly depends on the local environment, including the humidity, temperature, hydrophobicity of the carbon film, and the skill of the experimenter. The semi-automatic device, Vitrobot (FEI Company) has been specially designed to increase the reproducibility of making high-quality cryo-EM samples under controlled conditions.* **(c)** *This figure shows an EM image and diffraction patterns of three types of ices: (a)hexagonal, (b)cubic and* **(c)** *vitreous ices. Figure modified from (Dubochet et al., 1988).*

2.2 Introduction to image formation in electron microscopy

The electron microscope differs from the light microscope in the principles underlying image formation. Light microscope images mainly result from the variations in absorbance of different parts of an object, and amplitude contrast is the dominant factor in image formation. In the electron microscope, the majority of electrons in the beam pass through the specimen. Some of the electrons are deflected by interaction with the atomic nuclei or electrons surrounding nuclei in the specimen; this phenomenon is known as electron scattering. The mass density of the specimen, which is the product of specimen density and thickness, determines the amount of scattering. For example, the mean free path of a scattered electron is typically in a micrometer range for water molecules and in a millimeter range in air. Therefore, high vacuum in the column of the electron microscope and a very thin specimen (less than 1μm) are prerequisites for successful EM imaging. The final EM image consists of both amplitude contrast and phase contrast.

Amplitude contrast

There are two types of scattering events when an electron beam passes through a specimen: elastic scattering and inelastic scattering. Elastic scattering occurs when an incident electron interacts with a nucleus and the electron does not lose energy, but its path is deflected. The deflection angle of elastic scattering is proportional to the atomic number of the nucleus. Thus, a heavier atomic nucleus deflects an electron to larger angles. Inelastic scattering is due to the interaction between incident electron and the specimen electron clouds. The incident electrons undergo an energy loss, and a small deflection in their direction. Elastically scattered electrons deliver information on the 3D Coulomb potential distribution of the specimen, while inelastically scattered electrons contribute to the background noise of images.

A variation of scattering power across the specimen results in different scattering angle distributions. Some scattered electrons, whose deflection angles exceed a certain threshold angle set by the objective aperture in microscope, are excluded from image formation, thus generating intensity differences on resulting EM micrographs. Amplitude contrast varies as a function of mass density and atomic composition of the specimen. Amplitude contrast is the dominant factor in negative stain images because the heavy metal atoms in the stain possess much stronger scattering power than that of the biological specimen, which mainly consists of carbon, oxygen, nitrogen, and hydrogen atoms. An unstained, hydrated, biological specimen has little scattering difference than the surrounding water molecules. Thus, the contribution of amplitude contrast to a biological cryoelectron micrograph is very low (~ 7% to 10%). Another type of contrast, phase contrast, has to be implemented to attain an image with enough contrast, in order to visualize the biological particles.

Phase contrast and phase contrast transfer function

Phase contrast is best described in terms of wave optics. The specimen has to be thin enough, less than the mean free path of elastic electron, to fulfill the phase-object approximation, in which multiple scattering events are negligible. The outbound elastically scattered electrons can be treated as the incoming wave plane with a phase shift due to the modulation of the Coulomb potential of the specimen. The low scattering power of biological specimens allows the weak-phase approximation to be applied for analyzing image formation. A direct deduction of weak-phase approximation is that the phase shift between the scattered wave and unscattered wave is approximate 90^o (Frank, 2006). The contrast of an image taken at exact focus is very low because there is little contribution from amplitude contrast, and no amplitude difference between the scattered wave and unscattered wave. To make a phase shift visible, an image has to be taken out of focus, in order to introduce extra contrast resulting from the interference between the scattered waves and unscattered waves (Wade, 1992). The intensity of the recorded image holds a linear relationship to the potential projection of the weak phase object, but should not be regarded as a true image of the structural features in the specimen (Hawkes, 2007).

As mentioned above, the lenses in an electron microscope are far from ideal. Both lens aberrations and the effects of defocus contribute to distortions in the final image. In Fourier space, the Fourier transformation of a recorded image equals to the product of the image's wave function O(**k**), object aperture function A(**k**), and phase contrast transfer function (CTF) sin(γ(**k**)).

$$F(\mathbf{k}) = O(\mathbf{k}) \times A(\mathbf{k}) \times \sin(\gamma(\mathbf{k}))$$

$$\gamma(\mathbf{k}) = \pi \Delta z \lambda \mathbf{k}^2 + \frac{1}{2}\pi C_s \lambda^3 \mathbf{k}^4$$

Where **k** *is the spatial frequency vector*, Δz *is defocus of objective lens,* λ *is wavelength of electron beam,* C_s *is the spherical aberration constant of the microscope*

The function $\gamma(\mathbf{k})$ is determined by the spherical aberration C_s value and the defocus value Δz used. The sin function leads to an oscillation of the CTF (Figure II-2.a) and causes information loss at certain spatial frequencies due to the attenuated or zero value of the CTF. In addition, the finite size of the electron source (partial coherence) and energy spread of the illumination (chromatic coherence) attenuate the signal transferred to final image, especially at high spatial frequency range. Cumulatively, these effects can be simulated by an empirical Gaussian function $E(\mathbf{k}) = e^{B\mathbf{k}^2}$, with a empirical B factor (Zhou & Chiu, 2003). The B factor determines the effective dampening of the information at high spatial frequency and limits the attainable signal from a noisy cryoEM image (Figure II-2.b, c). High defocus values result in high contrast images, but with a rapidly decreasing envelope function towards high spatial frequency, i.e. high resolution. The effects of low defocus values are the opposite: higher signal at high spatial frequencies, but very low contrast images. The low contrast of cryoEM images makes particle picking and alignment extremely difficult because of poor contrast of the particles. In practice, the choice of defocus reflects a balance between contrast and desired resolution. Micrographs with a set of defocus values must be collected and combined in order to compensate for the information loss due to the CTF oscillation.

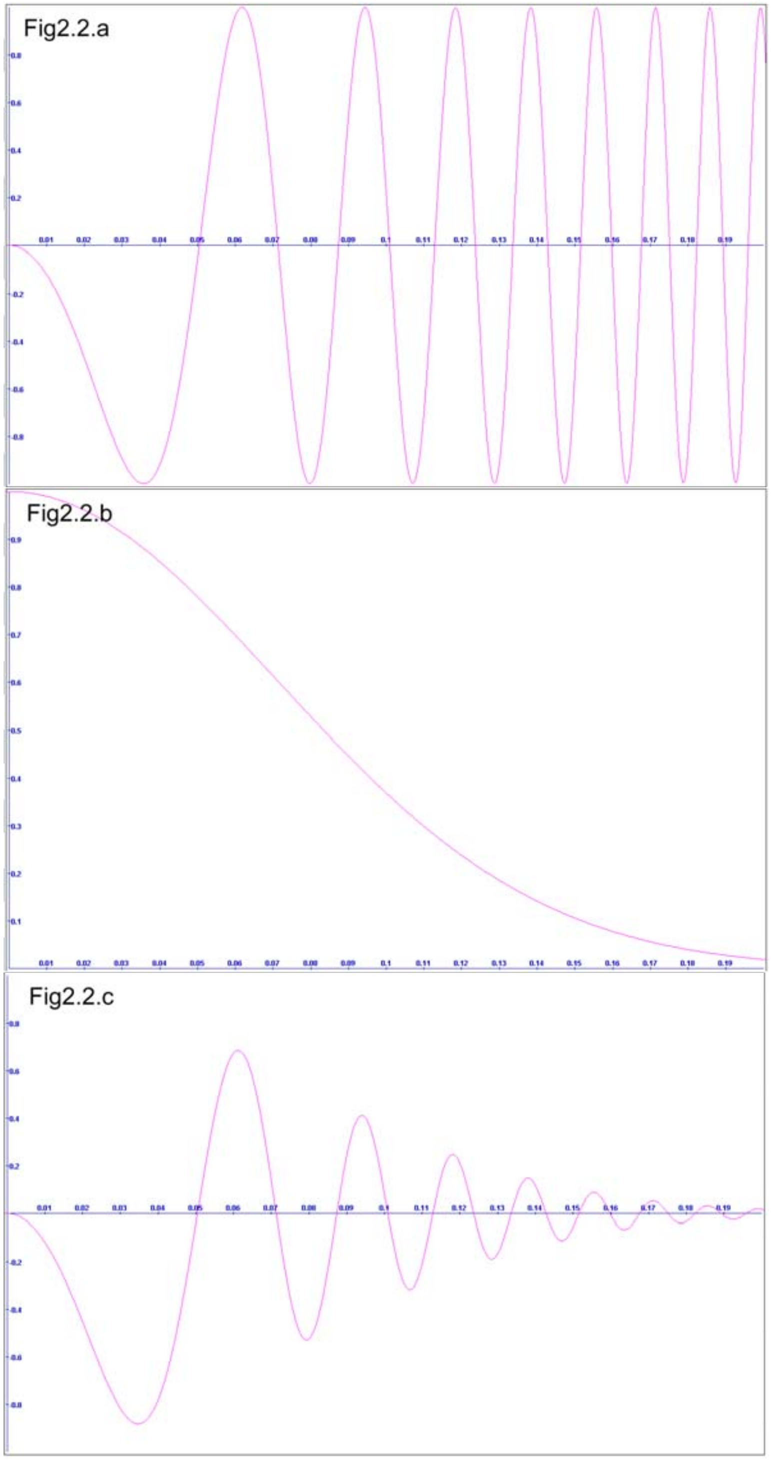

Figure II-2

(a) *A plot of the phase contrast transfer function sin(γ(***k***)) versus the spatial frequency* ($Å^{-1}$)*.* **(b)** *A plot of the empirical Gaussian simulation of cumulative envelope function* **(c)** *A plot of the product of the phase contrast transfer function(a) and envelope function(b). The intensity of CTF at high spatial frequency is dampened by the envelope function. These plots were generated by CTFsim (http://ncmi.bcm.tmc.edu/homes/wen/ctf).*

CTF determination and correction

To obtain the correct structural information of the specimen from the recorded image, we need to determine the CTF and envelop functions for the specific experimental conditions used. The first step toward CTF determination is to calculate the 2D power spectrum of a recorded image (Figure II-3.a). This step is typically calculated by a computer program if the image is recorded digitally by CCD camera, or produced by a diffractometer if the image is recorded on film. The 2D power spectrum is absolute-squared Fourier transformation of a recorded image. The rings in the 2D power spectrum are named Thon ring (Figure II-3.b). The deviation from the round power spectrum implies astigmatism due to imperfect optics, specimen drift, or charging effects. The 2D power spectrum may be radially averaged to create a 1D power spectrum. The spectrum is characterized by periodic maxima and minima along the spatial frequency axis because of the oscillating CTF.

The CTF may be determined manually or automatically, by matching the oscillation features of a calculated CTF with the image power spectrum. Various fully automated programs for CTF estimation have been implemented by many groups (Baxter et al., 2007; Frank et al., 1996; Grigorieff, 2007; Ludtke et al., 1999; van Heel et al., 1996), however, user interaction is routinely required. Phase flipping is the simplest form of CTF correction in which the image Fourier transformation is flipped to correct the phase by multiplying by -1 if the CTF value is below zero. The zeroes in the CTF and the attenuation of information at high spatial frequencies due to the envelop function remain untouched. If multiple images of one object are recorded at different defocus values, a Wiener filtering method may be applied to combine the information from various images, in order to restore the complete structural information across the spatial frequency spectrum (Frank, 2006). This effectively fills in the zeroes of the CTF since images with different defocus values will have CTF zeroes at different spatial frequencies. An inverse *B* factor may be used to correct for the effective envelop function (Zhou & Chiu, 2003).

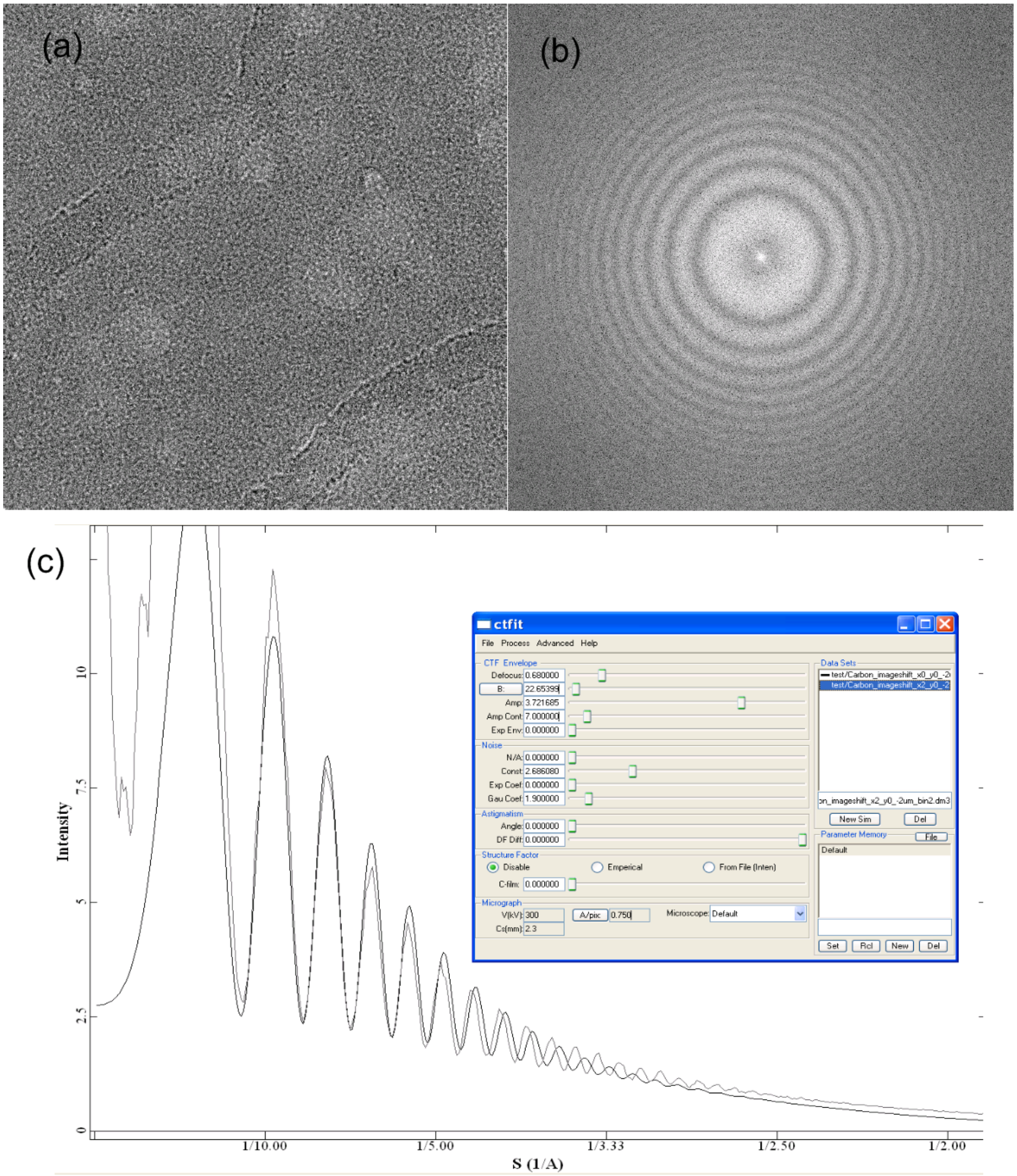

Defocus: 0.680000
B: 22.65399
Amp: 3.721685
Amp Cont: 7.000000
Exp Env: 0.000000
N/A: 0.000000
Const: 2.686080
Exp Coef: 0.000000
Gau Coef: 1.900000
Angle: 0.000000
DF Diff: 0.000000
● Disable ○ Emperical ○ From File (Inten)
C-film: 0.000000
V(kV): 300
A/pix: 0.750
Microscope: Default
Cs(mm): 2.3
test/Carbon_imageshift_x0_y0_-2
test/Carbon_imageshift_x2_y0_-2
on_imageshift_x2_y0_-2um_bin2.dm3
Default

Figure II-3

(a) *A typical EM image of carbon film.* **(b)** *The Fourier transform of the image in (a), characterized by periodic Thon rings.* **(c)** *A screen snapshot of the CTFit program in the EMAN package. The 1D power spectrum (gray line) is the circular average of (b). The CTF and envelop function parameters are manually input by the user in the interactive input window to generate the estimated CTF curve (black line). After the CTF and envelop functions are satisfactorily fit, phase flip correction may be chosen from the menu.*

2.3 Introduction to three-dimensional image reconstruction theory

The theory of three-dimensional image reconstruction through Fourier transformation and synthesis was proposed in 1968, and was demonstrated by calculating a helical recontruction of the bacteriophage T4 tail (De Rosier & Klug, 1968). Crowther et al. extended the methodology for single particles and successfully applied it to two icosahedral viruses (human wart virus and tomato bushy stunt virus) (Crowther et al., 1970). The principle underlying the reconstruction theory is the Projection theorem, which states that a Fourier transformation of a 2D projection of a 3D object is equivalent to a 2D plane perpendicular to the projection orientation, which passes through the center of the Fourier transformation of the 3D object. This theorem also implies that by performing the reverse process of filling 3D Fourier space with sufficient 2D central planes, the 3D structure of the object can be reconstructed by inverse Fourier transformation. A unique 2D plane in Fourier space corresponds to a unique 2D projection in real space. Therefore, in theory we can reconstruct a 3D object by collecting multiple projections of unique orientations. The only information we need to determine is the orientations of the 2D projections relative to the 3D object, which is equivalent to knowing the orientations of the 2D planes in Fourier space.

There are two methods to obtain orientation information for recorded EM images: the first involves tilting the microscope stage to capture a series of images of one object (electron tomography), and the second is to capture one projection view of a large set of objects that are assumed to have the same 3D structure (single particle approach). The goal of both methods is to obtain enough information to allow 3D reconstruction of the specimen. However, both methods have their drawbacks. The tomography approach takes advantage of the known projection orientations of all of the recorded images in a tilt series. But, a biological specimen in vitreous ice suffers radiation damage from the accumulated electron dose, which limits the attainable resolution to ~50Å. Although tomography is not suitable for high-resolution studies of biological macromolecular assemblies, it is particularly useful for structural studies of whole cells, cell organelles, and polymorphic viruses (Baumeister, 2005; Baumeister et al., 1999; Jensen & Briegel, 2007). The second method, the single particle approach, is based on the premise that individual particles in EM images represent projections of the same 3D structure in different orientations. According to the projection theorem, the 2D Fourier transformations of individual particle images pass through the center of the 3D Fourier transform, so every pair of 2D planes must share one identical line, named a "common line" (Crowther et al., 1970). The shared common lines can be identified by exhaustive computer search for every pair of 2D particle images. In practice, the common line search can be performed either in Fourier space or in real space (Frank, 2006).

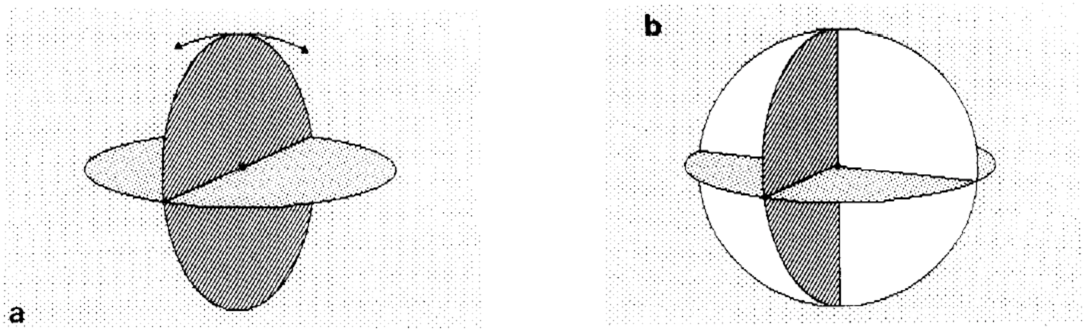

Figure II-4

(a) *A diagram illustrates a common line shared by a pair of 2D planes. Only one common line does not fix the relative orientation between two 2D planes because of the extra degree of freedom (indicated by the arrows).* **(b)** *Introducing a third plane, i.e. three common lines, will fix the relative spatial orientation of all 2D planes. Reprinted with permission from (Van Heel, 1987)*

The low SNR of cryoEM images hampers accurate determination of common lines. To overcome this problem, particle images representing the same projection view are classified into classes, and all members in one class are averaged to create a class-sum image with enhanced SNR (van Heel et al., 2000). We must keep in mind that the classification and averaging steps might blur the subtle structural difference between the members in one class, and therefore class averaging will compromise the attainable resolution of the final 3D reconstruction. In practice, class averaging is recommended at the early stage of building an initial model, but not for the later refinement steps that aim to generate a high resolution reconstruction. After a bootstrapping Euler-angle search, an initial reconstruction can be calculated but it is far from optimal. The next steps of single-particle reconstruction are iterative refinement (van Heel et al., 2000). A set of reference projections evenly covering Euler space can be calculated from the initial reconstruction. The class-sums or particles images are aligned with the reference projections to determine more accurate angles, which leads to a better reconstruction (Frank, 2006). The whole process needs to be iterated many times until the final reconstruction converges and there is no further improvement in resolution. The Fourier shell correlation (FSC) method is used to estimate the resolution of a reconstruction in the single particle approach (van Heel & Schatz, 2005). The whole particle set is divided into two datasets, and from which two 3D reconstructions are generated. A 1D correlation coefficient curve as a function of spatial frequency is calculated by comparing the two reconstructions in Fourier space. A threshold of 0.5 is generally accepted to determine the resolution value of the final reconstruction. However, the resolution from the FSC method is only suggestive, not an absolute resolution.

Typical resolutions from single particle analysis range from 20 to 6 Angstrom. The interpretation of resulting density maps requires expert knowledge of the biological system and careful inspection. In order to identify and separate the known components/domains from the density maps, external information, such as atomic structures of components, homologous structures in databases, and biochemical and biophysical constraints, are extremely useful (Koteiche et al., 2005). The docking and fitting of an atomic structure into a density map usually are accomplished by computer programs. But the fitting results demand scrutinization, which leads to meaningful biological explanations and hypotheses.

2.4 Materials and methods for experiments

Site-directed mutagenesis

Site-directed mutagenesis of T4L and Hsp16.5-TR (amino acids 34-147) was described previously (Koteiche & Mchaourab, 2002; Mchaourab et al., 1996). To generate Hsp16.5-P1 and Hsp16.5-P1N, the Hsp27 P1 peptide sequence was inserted in the Hsp16.5 gene between residues 33 and 34 and residues 12 and 13 respectively using overlap extension PCR. The cysteine mutants of Hsp16.5-P1 and arginine mutant of Hsp16.5 were generated using the QuikChange method (Stratagene). All plasmids were sequenced to confirm the substitution and the absence of unwanted changes. Single-site mutants are named by specifying the original residue and the number of the residue followed by the new residue.

Expression, purification and labeling

Expression, purification and labeling of T4L mutants were carried out as described (Mchaourab et al., 1996). Briefly, plasmids containing the appropriate vectors were transformed into *Escherichia coli* BL21(DE3) competent cells. Cultures, inoculated from overnight seeds, were grown to midlog phase at 37 °C until A600 ~ 0.8. The cultures were then induced with the addition of 0.4 mM isopropyl-β-D-thiogalactopyranoside and grown for 3 h at a temperature of 32 ° C. After cell lysis and precipitation of DNA by polyethyleneimine, Hsp16.5 and its mutants were purified by sequential, anion exchange, hydrophobic interaction and size exclusion (SEC) chromatography (Koteiche & Mchaourab, 2002). For SEC, a Superdex 200 column was used for Hsp16.5, Hsp16.5-R107G, and Hsp16.5-TR and a Superose 6 column for Hsp16.5-P1 and Hsp16.5-P1N.

The buffer for SEC contained 9 mM MOPS, 6 mM Tris, 50 mM NaCl, 0.1 mM EDTA and 0.02% NaN3 at pH7.2 and was used for subsequent binding studies.

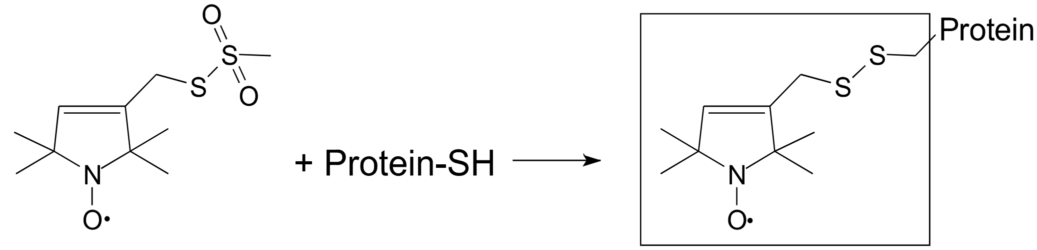

Spin Label I

Side Chain R1

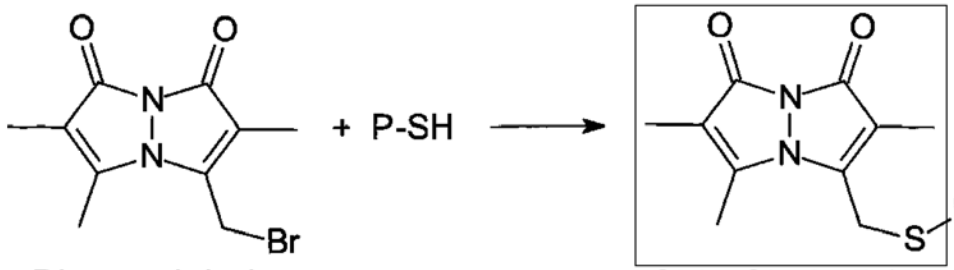

Bimane label

Side Chain R1

Labeling of the cysteine mutants with either bimane or MTSSL was carried out as previously described (Koteiche & Mchaourab, 2002; Sathish et al., 2003). Single-site mutants are named by specifying the original residue and residue number followed by R1.

Binding of T4L mutants to Hsp16.5 variants

Samples containing 5, 7, 10 or 14 µM T4L and varying concentrations of Hsp16.5 and it variants were incubated at 37ºC for 2 hours. The fluorescence intensity measurements were carried out on a PTI L-format spectrofluorometer equipped with an RTC2000 temperature controller and a sample holder containing a Peltier heater/cooler. The bimane molecule was excited at 380 nm and the fluorescence emission spectra were then recorded in the 420-500 nm range. The binding isotherms were fit with the appropriate equations (Sathish et al., 2003) using the program Origin (OriginLab Inc.). The Levenberg-Marquart method was used for nonlinear least squares fits.

Size exclusion chromatography (SEC)

Analytical SEC was performed on a Superose 6 column. The samples, at a concentration of 1 mg/ml, were prepared in the SEC buffer described above and injected from 100 µl volumes at a flow rate of 0.5 ml/min. For molar mass determination, a multi-angle laser light-scattering detector (Wyatt Technologies) was connected in line with the absorption detector. The signal at the 90º angle was analyzed to obtain molar mass values, both protein absorption at 280nm and bimane emission at 470nm, which is excited at 380nm, are measured.

Electron Paramagnetic Resonance (EPR)

EPR spectra were collected on a Bruker EMX spectrometer. The microwave power was 5 mW, modulation amplitude was 1.6 G and the scan width was 200 G. Distances were determined by non-linear least squares fitting of the EPR spectra based on the convolution approach (Rabenstein & Shin, 1995) assuming one or two Gaussian distance distributions.

CryoEM imaging

CryoEM grids were prepared by applying 2.5 µl of (0.5 to 1 mg/ml) protein, to R2/4 Quantifoil grids (Quantifoil Micro Tools GmbH) and 2/2 C-Flat grids (ProtoChips Inc.). The excess liquid from the droplet was blotted away with filter paper, and the sample grid was immediately plunged into liquid ethane cooled by liquid nitrogen using either a homemade vitrification device or a Vitrobot (FEI, Eindhoven, The Netherlands).

CryoEM data collection was performed for all samples on an FEI Tecnai 12 (120kV, LaB6) electron microscope (120kV, 67,000X nominal magnification, underfocus range 0.7 to 2.90 μm) equipped with a Gatan cryo-holder and UltraScan 2kx2k CCD camera (Gatan Inc., Pleasanton, CA). The Angstrom-to-pixel ratio on the molecular scale for the 120kV micrographs is 1.5 Å; and 3.1 Å after binning for image processing.

A high resolution cryoEM dataset was collected for Hsp16.5-P1 on an FEI Polara (300kV, FEG) electron microscope (liquid nitrogen temperature, 300kV, 310,000X nominal magnification, underfocus range 0.6 to 1.9 μm) with an UltraScan 4kx4k CCD camera. The Angstrom-to-pixel ratio on the molecular scale for the 300kV micrographs is 0.4 Å; and 1.5 Å after binning for image processing. The microscope magnifications were calibrated to within +/-0.5% with a negatively stained TMV grid (Saban et al., 2006). Since late of 2006, a Tecnai and Gatan scripting interface package was developed to facilitate semi-automated targeting, data-acquisition, and image quality assessment (Shi, Williams, Stewart, In preparation).All collected datasets of specimens studied are listed below.

Specimen	Micrographs	Particle numbers	Microscope
Hsp16.5-P1	809	3,570	TF30
Hsp16.5-P1	698	13,798	T12
Hsp16.5-P1+T4L	401	19,804	T12
Hsp16.5-P1N	233	4,980	T12
Hsp16.5-WT	327	12,909	T12
Hsp16.5-WT+T4L	425	11,451	T12
Hsp16.5-TR	251	18,799	T12
Hsp16.5-TR+T4L	235	20,499	T12
Hsp16.5-R107G	161	13,390	T12
DNAPK-cs (collaborate with Dr. Williams)	~18,000	356,000	T30
CaMKII	~1,800		T12
CTV/PMV/SMV	~300		T12

Image processing

The contrast transfer function (CTF) correction was performed with the CTFIT routine in the EMAN v1.7 package (Ludtke et al., 1999). For the 300kV micrographs, the CTF parameters were determined with CTFFIND3 (Mindell & Grigorieff, 2003) and CTF correction (phase flipping only) was performed by the EMAN routine APPLYCTF. The particle images were selected by BOXER, a semi-automatic routine in EMAN, or BATCHBOXER, an automatic routine in EMAN. The particle images were low-pass filtered to 19 Å (120kV), or 6 Å resolution (300kV). The IMAGIC-5 package (van Heel et al., 1996) was used to calculate initial class-sum images.

For the initial Hsp16.5-P1 model, C4, D4, and octahedral symmetries were tested with IMAGIC-5 and the results indicated octahedral symmetry. The best Hsp16.5-P1 reconstruction from the 120kV dataset was used as the starting model for the 300kV dataset reconstruction and refinement with EMAN. The resolution of the final Hsp16.5-P1 reconstruction is 10.3 Å as assessed by the 0.5 FSC threshold. Octahedral symmetry was imposed on the Hsp16.5-WT, Hsp16.5-TR, Hsp16.5-TR+T4L, and Hsp16.5-WT+T4L datasets based on resemblance of the class-sum images to Hsp16.5-WT. All 120kV datasets are reconstructed and refined with FREALIGN (Grigorieff, 2007), using the Hsp16.5-WT or Hsp16.5-P1 density map as starting models. A set of C-shell scripts are used to split the dataset to parallelize processing and combine all resulting parameter files to calculate the density maps. The five orientational parameters (three angular [Psi, Theta, Phi] and two translational [SHX, SHY]) and defocus and astigmatism parameters [DF1, DF2, ANGAST] for each particle are refined iteratively. Image processing was performed on the Vampire linux cluster at Vanderbilt. The final resolutions are assessed by the conservative 0.5 Fourier shell correlation (FSC) threshold. Molecular graphics images were produced using the UCSF Chimera package (Pettersen et al., 2004).

Docking of the α-crystallin domain dimer

A dimer of α-crystallin domains (aa 33-135) was extracted from the Hsp16.5 crystal structure (PDB ID 1SHS) (Kim et al., 1998a) and fit within the Hsp16.5-P1 reconstruction with the CoLoRes routine in the Situs v2.2 package (Chacon & Wriggers, 2002). Octahedral symmetry was applied to the coordinates for the best dimer position resulting in a pseudoatomic model for the oligomer (24 dimers, or 48 monomers). Three dimers around a 3-fold window in the pseudoatomic model and crystal structure were compared and an r.m.s.d. of 1.9 Å was found with Chimera. The pseudoatomic model was converted to a density map with the PDB2MRC routine in EMAN and subtracted from the cryoEM density to generate a difference map. The backbone torsion angles of the B-chain C-terminal extension were adjusted using Swiss-PDB viewer (Guex & Peitsch, 1997).

CHAPTER III

CRYOEM AND EPR ANALYSIS OF ENGINEERED SYMMETRIC AND POLYDISPERSE HSP16.5 ASSEMBLIES REVEALS DETERMINANTS OF POLYDISPERSITY AND SUBSTRATE BINDING

3.1 Abstract

We have identified sequence and structural determinants of oligomer size, symmetry and polydispersity in the small heat-shock protein superfamily. Using an insertion mutagenesis strategy that mimics evolutionary sequence divergence, we induced the ordered oligomer of Methanococcus jannaschii Hsp16.5 to transition to either expanded symmetric or polydisperse assemblies. Using a hybrid approach that combines spin labeling electron paramagnetic resonance (EPR) and cryoelectron microscopy (cryoEM) imaging at 10 Å resolution, we demonstrate that the underlying plasticity is mediated by a packing interface with minimal contacts and a flexible C-terminal tether between dimers. Twenty-four dimeric building blocks related by octahedral symmetry assemble into the expanded symmetric oligomer. In contrast, the polydisperse variant has an ordered dimeric building block that heterogeneously packs to yield oligomers of various sizes. Increased exposure of the N-terminal region in the Hsp16.5 variants correlates with enhanced binding to destabilized mutants of T4 lysozyme, while deletion of this region reduces binding. Transition to larger intermediates with enhanced substrate-binding capacity has been observed in other small heat-shock proteins including lens -crystallin mutants linked to congenital cataract. Together, these results provide a

mechanistic perspective on substrate recognition and binding by the small heat-shock protein superfamily.

3.2 Introduction

In the crowded molecular environment of the cell, five classes of heat shock proteins (HSP) act as molecular chaperones by suppressing protein aggregation through the selective binding of proteins in non-native states (Parsell & Lindquist, 1993; Xu & Sigler, 1998). Subsequent processing of the bound polypeptides involves either release and refolding or delivery to degradation machineries. Small heat shock proteins1 (sHSP) are members of a superfamily of oligomeric proteins characterized by a conserved module in the C-terminal region of their sequences referred to as the α-crystallin domain (de Jong et al., 1998; Van Montfort et al., 2001a). In vitro, sHSP are protein stability sensors that can differentially bind mutants with similar structures in the folded state, but different free energies of unfolding (Mchaourab et al., 2002; Shashidharamurthy et al., 2005). Substrates are bound with efficiencies that can reach 1 substrate molecule per subunit of sHSP and without direct input of ATP energy (Ehrnsperger et al., 1997; Lee et al., 1995; Sathish et al., 2003). Bound substrates are protected against heat inactivation and can be released from sHSP complexes by other members of the chaperone network (Ehrnsperger et al., 1997; Lee et al., 1997). sHSP play critical roles in maintaining vertebrate lens transparency (Horwitz, 2000) and in a number of physiologic processes (Eaton et al., 2001; van de Klundert & de Jong, 1999; van de Klundert et al., 1998). Their expression in C. elegans promotes longevity and delays the onset of polyglutamine protein aggregation (Hsu et al., 2003).

The structural basis of substrate recognition and binding by sHSP continues to be enigmatic. Most sHSP assemble into polydisperse and dynamic oligomers and their heterogeneity is enhanced by substrate binding. Available high-resolution structures are for three ordered, symmetrical sHSP assemblies, Hsp16.5 from Methanococcus jannaschii (MJ) (Kim et al., 1998a), Hsp16.9 from wheat (Van Montfort et al., 2001a), and the more distantly related Tsp36 from a parasitic flatworm (Stamler et al., 2005), but there is a paucity of structural information for polydisperse sHSP. Many sHSP oligomers exchange subunits on a relatively fast time scale (Bova et al., 1997; Bova et al., 2000). The functional role of equilibrium dissociation has been controversial (Haslbeck et al., 2005) with one class of models implicating the dissociated form as a major binding-competent species (Shashidharamurthy et al., 2005; Van Montfort et al., 2001a).

Taken together, crystallographic (Kim et al., 1998a; Van Montfort et al., 2001a), cryoEM (Haley et al., 2000; Haley et al., 1998) and spin labeling EPR (Koteiche & Mchaourab, 1999) analyses of selected sHSP reveal a remarkably versatile protein scaffold amenable to a wide range of oligomeric structures and dynamic behaviors. The oligomer of Hsp16.5 is monodisperse and composed of 24 subunits assembled with octahedral symmetry. On the other end of the spectrum, the mammalian α-crystallins and human Hsp27 form heterogeneous oligomers of different sizes and shapes (Haley et al., 2000). The basic building block of Hsp16.5 is a dimer of the conserved α-crystallin domain. In wheat Hsp16.9, distinct packing by the dimeric building block, facilitated by two conformations of the C-terminal extension, reshapes the quaternary structure resulting in a double disk assembly (Van Montfort et al., 2001a).

The mechanism by which a conserved module such as the α-crystallin domain mediates highly specific contacts to form symmetrical assemblies in some contexts and yet can participate in polydisperse assemblies in others is one of the mysteries in the sHSP field. Comparative sequence analysis provides hints regarding the determinants of the quaternary structural variation found in the sHSP family (de Jong et al., 1998). sHSP have undergone extensive sequence divergence with remnants of sequence similarity in the α-crystallin domain while the N-terminal region is highly variable and is generally hydrophobic. The short C-terminal extensions following the α-crystallin domain are of variable length with a conserved sequence motif that serves to tether the dimeric building blocks in Hsp16.5 and Hsp16.9.

Guided by analysis of sHSP sequence divergence, we have transformed the ordered and monodisperse Hsp16.5 assembly into both a larger symmetrical assembly as well as polydisperse oligomers consisting of variable numbers of subunits. The structural basis of oligomeric plasticity is gleaned from a hybrid approach combining cryoEM and site-directed spin labeling (SDSL) EPR (Koteiche et al., 2005). The functional consequence of polydispersity is explored using a steady-state binding assay to non-native states of T4 lysozyme (T4L) (Mchaourab et al., 2002). Together, these results identify the sequence motifs responsible for the transition between ordered and variable quaternary structures, define the structural basis of oligomeric plasticity, and elucidate the nature of the intermediates involved in substrate binding and recognition.

3.3 Results

Flexible peptide insertions in Hsp16.5 lead to novel structural assemblies

Sequence alignment of members of the sHSP family (Van Montfort et al., 2001a) identifies a unique 14-residue proline and alanine rich sequence at the junction between the N-terminal and α-crystallin domains of Hsp27, labeled P1 in Figure III-1a. We have previously demonstrated that the P1 peptide is involved in equilibrium dissociation of the Hsp27 oligomer (6). The peptide is expected to have a highly flexible backbone; therefore we predicted that its insertion might affect the dynamic properties of the ordered Hsp16.5 oligomer. Indeed, insertion of this sequence at two positions in the Hsp16.5 sequence alters the size and polydispersity of the oligomer as revealed by molecular mass determination across the size exclusion chromatography (SEC) peaks (Figure III-1b). Introduction of the P1 peptide after residue E12, in a helix in the N-terminal region of Hsp16.5 (Koteiche et al., 2005), induces the formation of a highly polydisperse oligomer (Hsp16.5-P1N) with an average molecular mass of ~650 kDa and a mass distribution reminiscent of that of mammalian sHSP. In contrast, insertion of P1 at the junction between the N-terminal and α-crystallin domains leads to the formation of a monodisperse oligomer (Hsp16.5-P1) with a molecular mass approximately double that of wild type (WT) (~850 kDa). Considering the additional mass of the inserted peptide, this indicates that the oligomer consists of 48 subunits, or twice the number of subunits in the WT oligomer. Simply deleting the N-terminal region of Hsp16.5 (variant Hsp16.5-TR lacking aa 1-33) produces an assembly similar to WT, differing only in the mass of the deleted sequence.

CryoEM reconstructions show that Hsp16.5-TR has an outer shell similar to WT but without any internal density while Hsp16.5-P1 has a larger outer shell with weak internal density (Figure III-1c). Comparison of the Hsp16.5-TR reconstruction with that of WT along with previous SDSL-EPR (Koteiche et al., 2005) supports the assignment of the internal density to the N-terminal region, which was not visible in the crystal structure. The Hsp16.5-TR reconstruction also confirms previous spin labeling EPR data indicating that the α-crystallin domain and C-terminal extension encode all of the subunit interactions necessary for oligomeric assembly (Koteiche & Mchaourab, 2002). The Hsp16.5-P1 structure indicates that the α-crystallin domain can form a symmetrical assembly significantly larger in diameter than WT and that the inserted P1 peptide is disordered, leading to poorly reconstructed internal density. This is despite SDSL-EPR data for the N-terminal region of Hsp16.5-P1 indicating a pattern of proximity between spin labels similar to that of the WT.

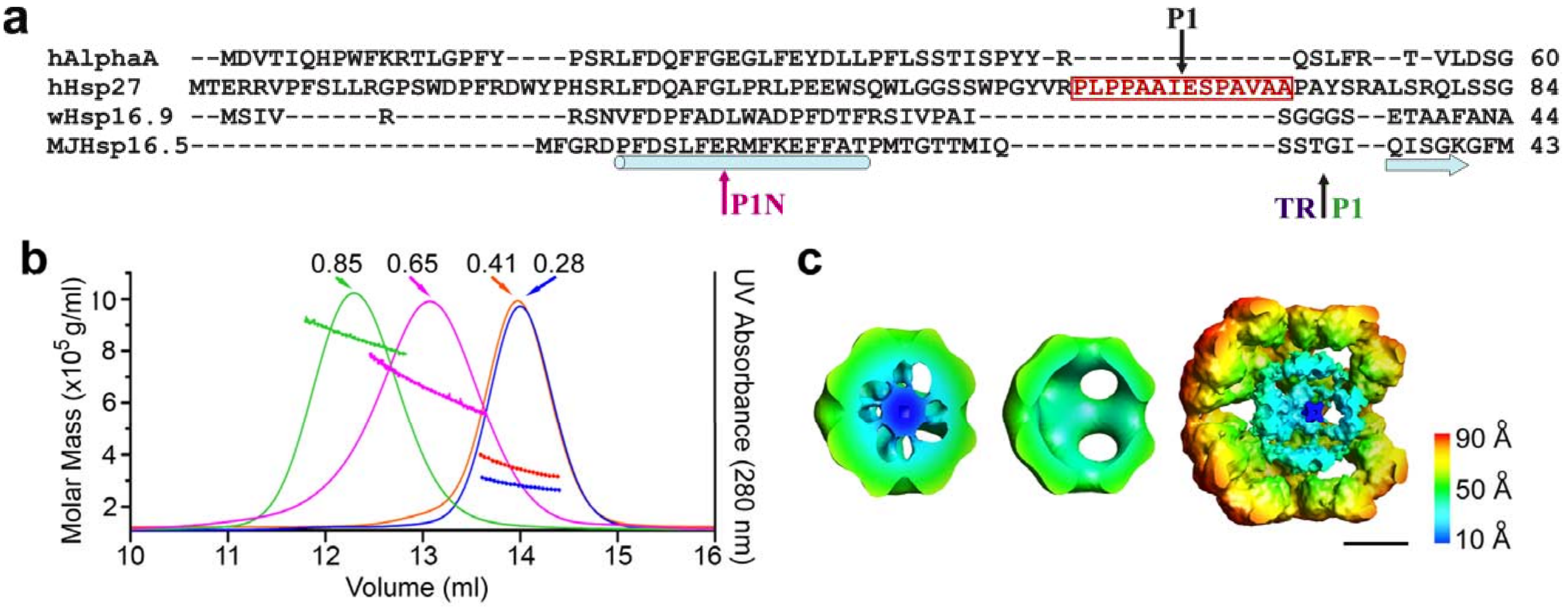

Figure III-1

(a) *Alignment of the N-terminal sequence of selected sHSP. The 14-residue P1 sequence unique to human Hsp27 is boxed in red. The positions for the insertion of the P1 peptide within the Hsp16.5 sequence to generate Hsp16.5-P1 and Hsp16.5-P1N are indicated by arrows and labels color coded to correspond to the size exclusion profile. The position of the N-terminal truncation is indicated by TR. The light blue rod indicates the α-helix modeled for the N-terminal region of Hsp16.5 (25). The light blue arrow indicates the first β-strand of the α-crystallin domain in Hsp16.5.* ***(b)*** *Molar mass distribution and UV absorption profiles of WT Hsp16.5 (orange), Hsp16.5-TR (blue), Hsp16.5-P1 (green) and Hsp16.5-P1N (magenta). The lines across the UV absorbance peaks are calculated molar mass values obtained as a function of elution volume. The numbers above indicate the molar mass at the peak.* ***(c)*** *Three-dimensional cryoEM reconstructions of WT Hsp16.5 (Haley et al., 2000), Hsp16.5-TR, and Hsp16.5-P1 (left to right) shown cropped in half and radially color-coded. The isosurface values were set to enclose 100% of the expected volumes for full (uncropped) reconstructions. The scale bar represents 50Å. Reprinted with permission from(Shi et al., 2006)*

CryoEM reveals a highly fenestrated and symmetrical structure for Hsp16.5-P1

CryoEM class-sum images reveal nearly perfect 2-fold, 3-fold and 4-fold symmetry indicative of an octahedral assembly for Hsp16.5-P1 (Figure III-2a). This is the same symmetry observed for WT and yet the subunit number is doubled in Hsp16.5-P1. A reconstruction of Hsp16.5-P1 was generated from a data set collected on a Polara (300kV, FEG) microscope (Figure III-2b). The resolution is 10.3 Å as assessed by the conservative 0.5 Fourier shell correlation (FSC) threshold. The Hsp16.5-P1 structure is more faceted than WT and there is a significant expansion with an increase in diameter from 120Å for the roughly spherical WT, to a maximum of 182 Å for Hsp16.5-P1. Furthermore, Hsp16.5-P1 has relatively large openings in the outer protein shell at both the 3-fold and 4-fold symmetry axes compared with the WT structure that has large windows only at the 3-fold axes.

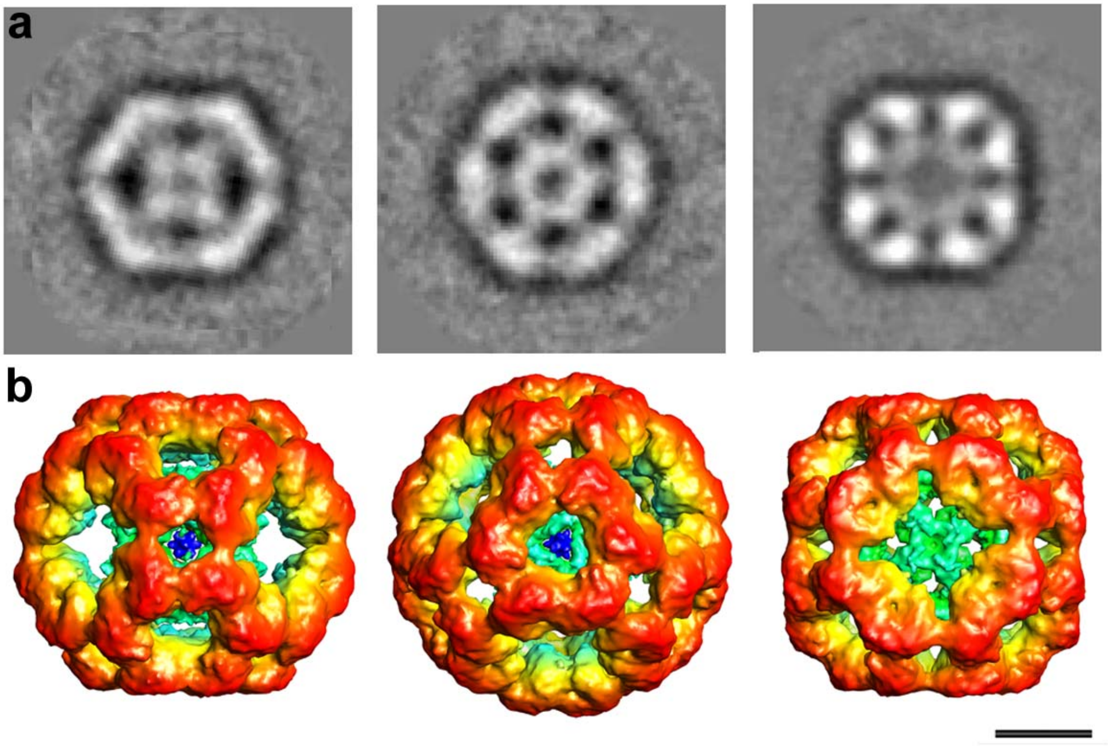

Figure III-2

(a) *Three selected class-sum images based on a 120kV cryoEM dataset showing 2-fold, 3-fold, and 4-fold symmetry from left to right.* ***(b)*** *CryoEM reconstruction of Hsp16.5-P1 at 10 Å resolution based on a 300kV FEG cryoEM dataset of 3080 particle images. Three surface views are shown aligned along the symmetry axes to resemble the class-sum images shown directly above. The radial color coding is the same as in Fig. 3.1c. The scale bar represents 50 Å. Reprinted with permission from (Shi et al., 2006)*

Preservation of the dimeric building block in Hsp16.5-P1

The reorganization of the quaternary structure in Hsp16.5-P1 does not involve disruption of the dimeric building block. We observed strong spin-spin couplings at residues near the two-fold symmetry axis of WT. EPR spectra at the same sites in the context of either Hsp16.5-P1 or WT shown in Figure III-3 are almost superimposable suggesting that the overall architecture of the dimer is preserved. For instance at site 42 located at the monomer-monomer interface, spectral components arising from spin labels separated by less than 8Å are evident in both WT and Hsp16.5-P1 (indicated by brackets). The change in the sharp spectral components represents about 5% increase in the population of singly-labeled dimers for Hsp16.5-P1 compared to the WT. Notable also is the close proximity between residues 46 and 97 that reflects the strand swapping between monomers.

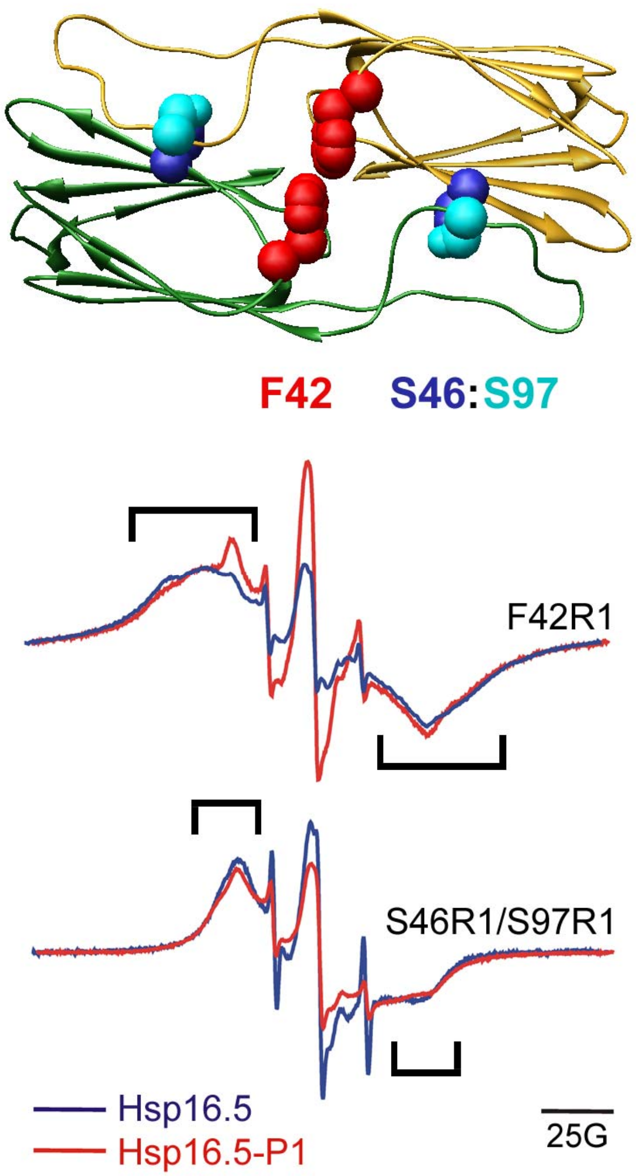

Figure III-3

The Hsp16.5 dimer interface is the same in WT Hsp16.5 and Hsp16.5-P1. Shown is the dimer of α-crystallin domains (aa 33-135) from the crystal structure of Hsp16.5 (PDB ID code 1SHS). The locations of F42, S46 and S97 are highlighted for reference. EPR spectra of a single-mutant (F42) and a double-mutant (S46/S97) of WT Hsp16.5 (Koteiche & Mchaourab, 2002) and Hsp16.5-P1. The brackets indicate nearly superimposable spectral components arising from spin labels within 8Å. Reprinted with permission from (Shi et al., 2006)

A pseudoatomic model of Hsp16.5-P1 reveals two non-equivalent subunit positions

On the basis of the EPR data, a dimer of α-crystallin domains (aa 33-135) was extracted from the crystal structure of Hsp16.5 and fit within the Hsp16.5-P1 cryoEM density by the quantitative docking tool CoLoRes in the Situs software package (Chacon & Wriggers, 2002). Both possible hands of the cryoEM density were tested and a significantly better correlation (12% higher) was found for the hand shown in Figure III-2 and III-4. The best fit dimer position was selected and octahedral symmetry was imposed resulting in the generation of a pseudoatomic model for all of the α-crystallin domains in Hsp16.5-P1 (Figure III-4a). The atomic fitting indicates that the outer protein shell of the Hsp16.5-P1 oligomer is formed by 48 α-crystallin domains. The α-crystallin monomers are found in two independent positions, referred to as chains A and B. The pseudoatomic model has three dimers around the opening at the 3-fold symmetry axis (Figure III-4b) and four dimers around the larger opening at the 4-fold axis (Figure III-4c). The high degree of accuracy of the pseudoatomic model is highlighted by the delineation observed between α-crystallin monomers (Figures III-4b and III-4c) and by the superposition of the three dimers around the 3-fold symmetry axis on three dimers from the WT Hsp16.5 crystal structure with an r.m.s.d. of 1.9 Å.

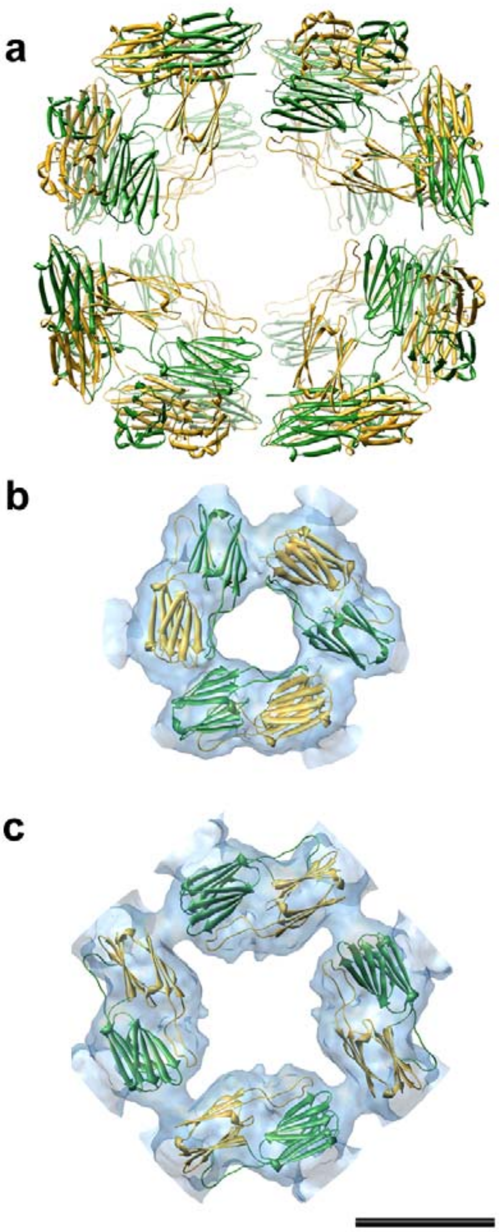

Figure III-4

Pseudoatomic model of the α-crystallin domains in Hsp16.5-P1 and the fit within the cryoEM density. ***(a)*** *The pseudoatomic model viewed along a 4-fold symmetry axis with 48 α-crystallin domain monomers. The independent monomer positions are colored either gold (chain A) or green (chain B).* ***(b)*** *Transparent surface representation of a portion of the Hsp16.5-P1 cryoEM reconstruction viewed along a 3-fold symmetry axis and fit with three α-crystallin domain dimers.* ***(c)*** *A similar view of Hsp16.5-P1 along a 4-fold symmetry axis and fit with four α-crystallin domain dimers. The scale bar represents 50 Å. Reprinted with permission from (Shi et al., 2006)*

Validation of the Hsp16.5-P1 pseudoatomic model by SDSL-EPR

To further validate the pseudoatomic model of Hsp16.5-P1, we determined proximities between spin labels near the symmetry axes. At sites along the two-fold symmetry axis of Hsp16.5-P1 such as G34, the spin labels are predicted to undergo strong dipole-dipole interactions and the EPR spectra are similar to those of spin labels introduced at the same sites in WT (Figure III-5a). In contrast, the increase in the spectral intensity observed at site 102 reflects an increase in distance between symmetry related copies as expected based on the location of these residues at the symmetry interfaces of Hsp16.5-P1. One independent α-crystallin monomer (chain B) in the pseudoatomic model has residue 102 facing the 3-fold opening as in the WT structure (Figure III-5b). The other independent monomer (chain A) has this residue facing the larger 4-fold opening that is only present in the Hsp16.5-P1 structure. Quantitative analysis of the EPR spectrum for residue 102 of Hsp16.5-P1 (Rabenstein & Shin, 1995) reveals two spectral components each representative of a ~50% spin population. One population represents dipolar-coupled spin labels as in WT, and the other population represents non-interacting spin labels consistent with a larger distance between sites around the 4-fold symmetry axes of Hsp16.5-P1. Similarly, the change in the EPR spectrum of spin label pair 51/80, which reports on the interaction between dimers, is consistent with a change in the relative orientations of residues 51 and 80 for approximately half of the sites in the Hsp16.5-P1 model (Figure III-5b).

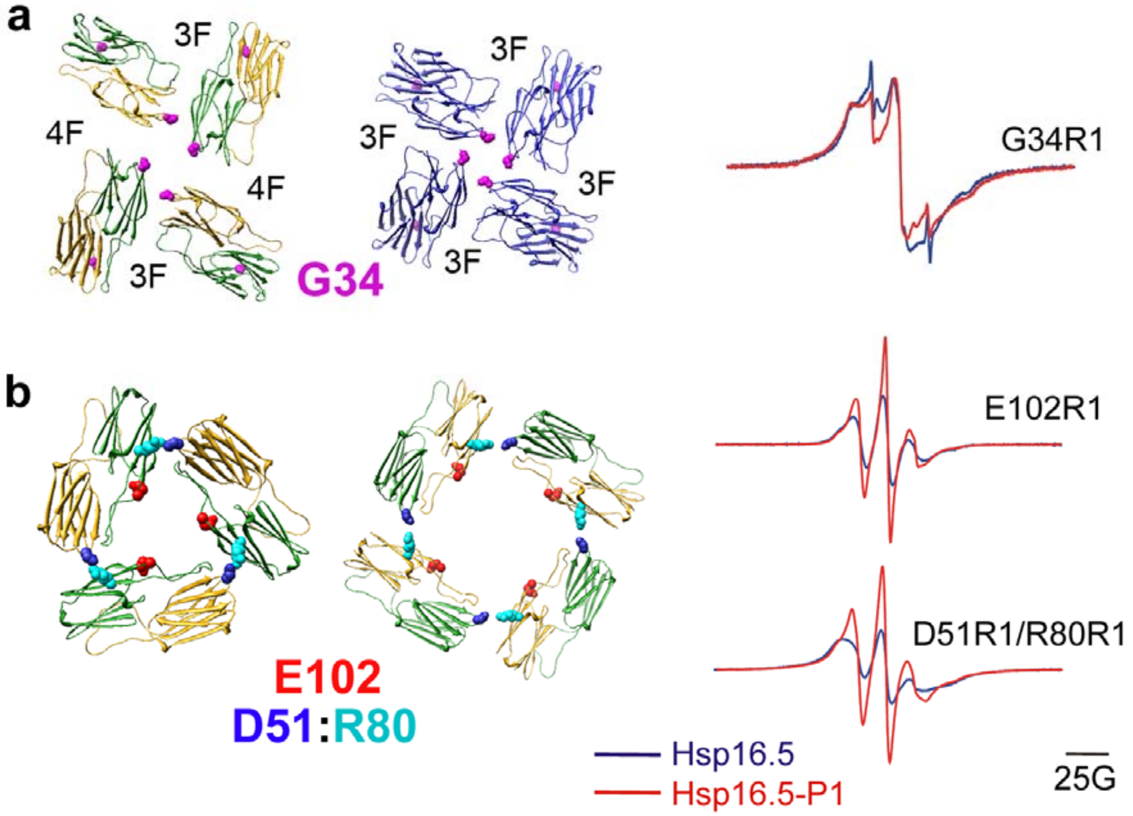

Figure III-5

(a) *α-crystallin domain dimers around a 2-fold symmetry axis of Hsp16.5-P1 (gold and green) compared to the α-crystallin domain dimers around a 4-fold symmetry axis of WT Hsp16.5 (blue). The EPR spectra at site 34 in the WT Hsp16.5 (Koteiche & Mchaourab, 2002) and Hsp16.5-P1 background are consistent with the close proximity of symmetry related copies of site 34 in both structures.* ***(b)*** *Location of residues 51/80 and 102 around 3-fold and 4-fold symmetry axes of the Hsp16.5-P1 model along with the EPR spectra of spin labels introduced at these sites in the WT and Hsp16.5-P1 backgrounds. The independent monomer positions in Hsp16.5-P1 are colored as in Figure III-4. Reprinted with permission from (Shi et al., 2006).*

The C-terminal extension is a flexible tether that enables repacking

To identify the structural features that mediate oligomer repacking, a difference map was calculated between the Hsp16.5-P1 cryoEM reconstruction and the pseudoatomic model which includes just the α-crystallin domains. Difference density was observed on the outer surface of both independent α-crystallin domains (chains A and B) in a groove between the two β-sheets of the α-crystallin domain where the C-terminal extension docks in the WT structure. Given that the three dimers around the 3-fold opening can be nearly superimposed on the WT Hsp16.5 crystal structure, it seems likely that the conformation of the C-terminal extensions that stabilize these three dimers is maintained in Hsp16.5-P1 as it is in WT. This accounts for the conformation of half of the 48 C-terminal extensions in Hsp16.5-P1, those of the A-chain monomers.

In view of the change in the interface angle at the corner of the 4-fold symmetry window, the C-terminal extensions of the B-chain monomers must have a modified conformation in order to stabilize the ring of four α-crystallin dimers. Difference density is observed extending from near residue 135 of the B-chain monomer over the A-chain α-crystallin domain forming an interlocked ring of four dimers (Figure III-6a). Simply attaching aa 136-147 in the WT conformation onto the B-chain monomer leads to a clash with the side of the A-chain α-crystallin domain. Therefore, we positioned the C-terminal extension over the A-chain α-crystallin domain so as to preserve the numerous hydrophobic interactions between residues 141-147 and the underlying α-crystallin domain. Small adjustments (12° to 37°) in the backbone torsion angles, staying within the allowed helical region of the Ramachandran plot, for residues 137 and 138 in the short α-helix enabled the extension to be connected to the rest of the B-chain monomer (Figure III-6b).

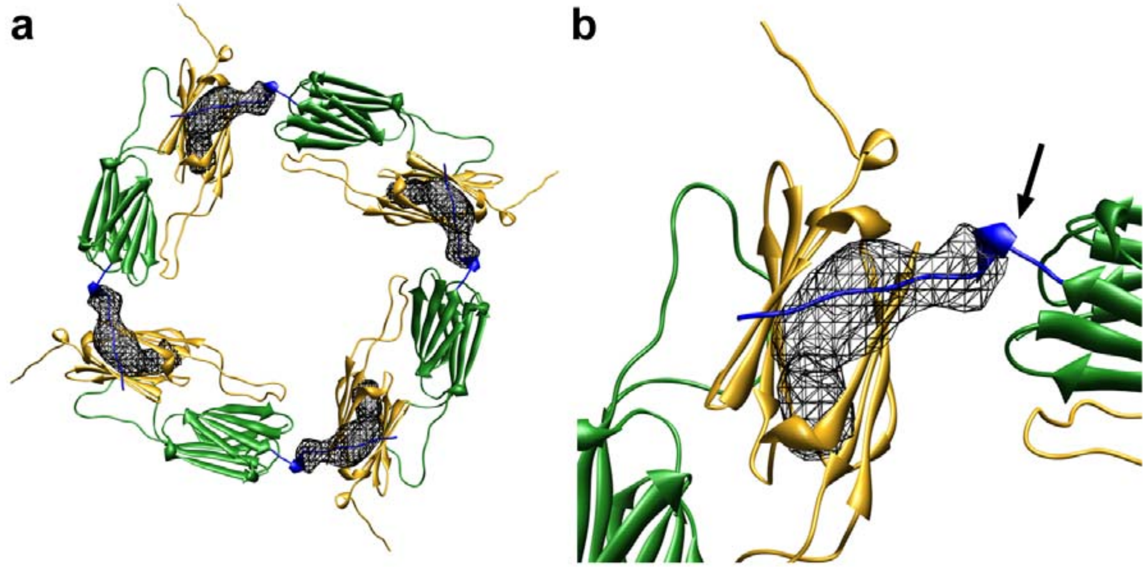

Figure III-6

The C-terminal tail can adapt to a new packing arrangement around the Hsp16.5-P1 4-fold symmetry axis. ***(a)*** *Four α-crystallin domain dimers with the difference density assigned to the C-terminal tail (mesh) above the A-chain α-crystallin domains.* ***(b)*** *Close up view showing that the re-positioned C-terminal tail (aa136-147, blue) fits within the difference density. The backbone torsion angles of residues 137 and 138 (arrow) were modified to connect the C-terminal tail to residue 135 of the neighboring B-chain α-crystallin domain. The independent monomer positions in Hsp16.5-P1 are colored as in Figure III-4. Reprinted with permission from (Shi et al., 2006)*

Plasticity at the dimer-dimer interface can lead to polydispersity

Structurally, the insertion position of P1 in Hsp16.5-P1 maps to the interface between α-crystallin domain dimers that is held together by only two ionic interactions (D51/R80 and E78/R93) (Kim et al., 1998a). In the WT structure neighboring α-crystallin domain dimers meet and form a 60° angle, thus creating the triangular openings at the 3-fold symmetry axes. The same angle is also found in the Hsp16.5-P1 pseudoatomic model around the 3-fold openings (Figure III-7a); however a larger angle of 90° is also found around the 4-fold opening (Figure III-7b). The combination of these two packing angles between α-crystallin domain dimers leads to the larger diameter octahedral assembly observed for Hsp16.5-P1. The sparseness of contacts between α-crystallin domain dimers, together with the adaptability of the C-terminal extension, are central to the ability of the Hsp16.5 sequence to form larger assemblies.

In contrast, when the Hsp27 P1 sequence is inserted between residues 12 and 13, to form the Hsp16.5-P1N variant, polydisperse assemblies are created. Cryoelectron micrographs of Hsp16.5-P1N show variably sized and shaped assemblies. In a dataset of ~5,000 particle images classified into 500 class-sum images, less than 5% of the class-sum images showed 2-, 3-, or 4-fold symmetry and these displayed only loose symmetry (Figure III-8a). In comparison most of the Hsp16.5-P1 class-sum images displayed essentially perfect 2-, 3-, and 4-fold symmetry (Figure III-2a). The more irregular class-sum images of Hsp16.5-P1N often show apparent gaps in the outer protein shell (Figure. III-8b). Given the heterogeneity in the Hsp16.5-P1N dataset it was not possible to calculate a three-dimensional reconstruction.

We explored the subunit arrangement in Hsp16.5-P1N by determining the pattern of proximity between spin labels near the axes of symmetries. At site 42 at the monomer-monomer interface, the EPR spectrum is unchanged from that of Hsp16.5-P1 (Figure III-8c) indicating that the dimeric building block is intact. The lack of spectral change at site 102 is consistent with the preservation of 3-fold and 4-fold windows in Hsp16.5-P1N. In contrast, the EPR spectrum at site 34 reveals increased distance heterogeneity at the dimer-dimer interface. We speculate that the highly variable quaternary structure of Hsp16.5-P1N can be explained by a continuum of angles between α-crystallin domain dimers. While the flexible C-terminal extension can adapt to many of these dimer packing angles, there are likely to be regions within the assembly where dimers can not be tethered. This would lead to gaps in the outer shell as suggested by the cryoEM images and to highly irregular assemblies of varying size and subunit copy number.

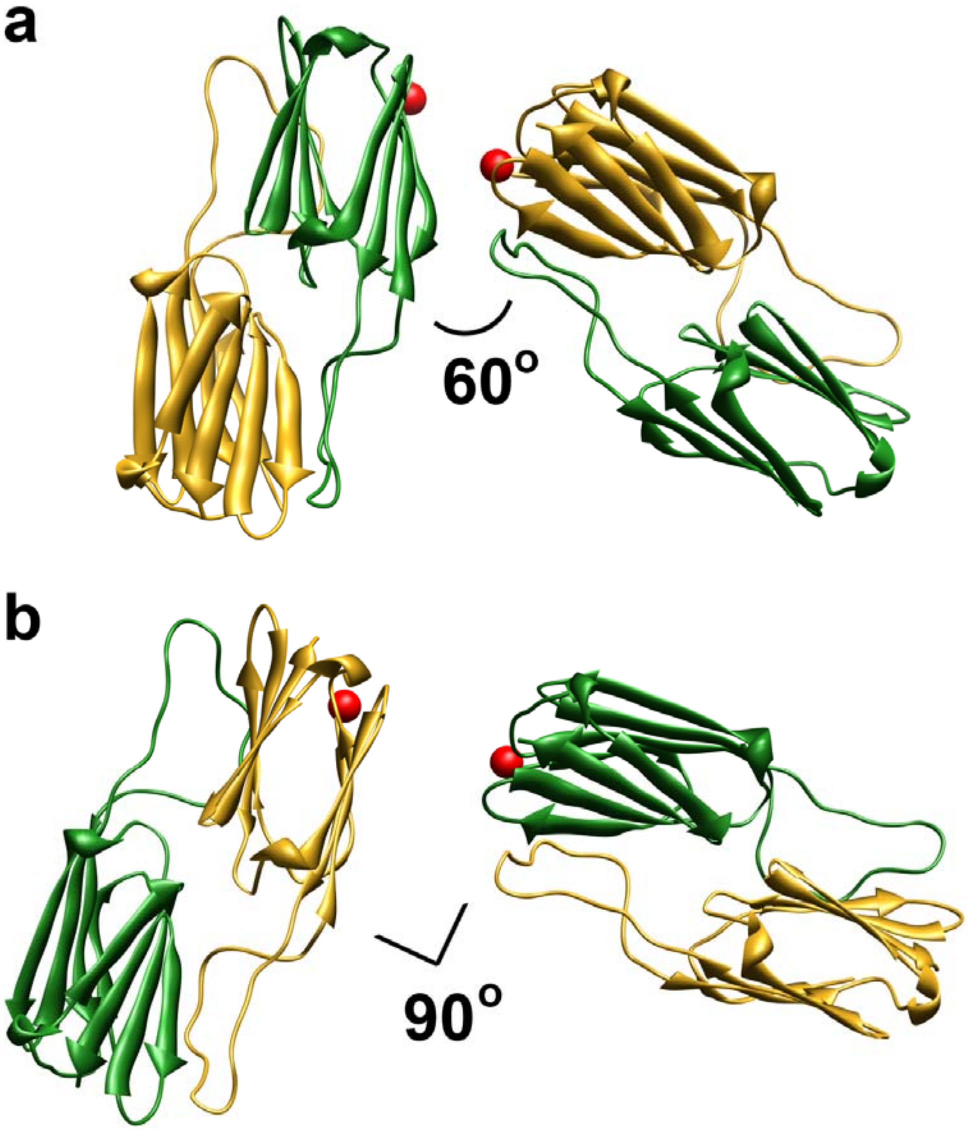

Figure III-7

The α-crystallin domain dimers pack with two distinct angles in Hsp16.5-P1. ***(a)*** *Two α-crystallin domain dimers packing with a 60° angle to form a 3-fold opening.* ***(b)*** *Two α-crystallin domain dimers packing with a 90° angle to form a 4-fold opening. Copies of residue 34 near the dimer-dimer interface are shown as red spheres. The independent monomer positions in Hsp16.5-P1 are colored as in Figure III-4. Reprinted with permission from (Shi et al., 2006)*

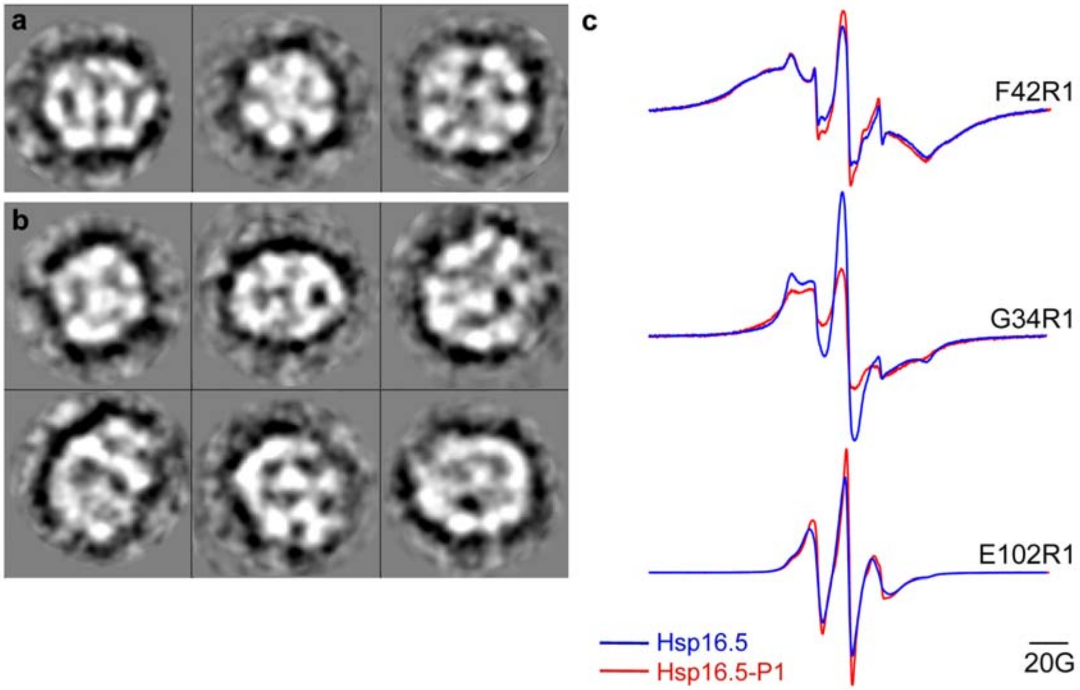

Figure III-8

***(a)** Three class-sum images of Hsp16.5-P1N selected from a total set of 500 class-sum images showing approximate 2-fold, 3-fold, and 4-fold symmetry, left to right. **(b)** Six class-sum images selected to represent the diversity and lack of symmetry in the majority of the class-sum images. **(c)** The superimposable EPR spectra at site 42 in Hsp16.5-P1 and Hsp16.5-P1N indicate that the dimer interface is not perturbed in Hsp16.5-P1N. The similar spectral line shapes at site 102 reflect the preservation of 3-fold and 4-fold windows in Hsp16.5-P1N. In contrast, the lineshape at site 34 indicates increased distance heterogeneity in Hsp16.5-P1N. Reprinted with permission from (Shi et al., 2006)*

Oligomer expansion enhances substrate binding

Transition to either large or polydisperse oligomers is accompanied by a significant increase in the apparent affinity to destabilized mutants of T4L (Mchaourab et al., 2002). Substrate affinity was determined using an assay where Hsp16.5 is presented with T4L mutants of progressively lower free energies of unfolding (ΔG_{unf}). At 37º C, ΔG_{unf} of T4L-L99A is 4.7 kcal/mol while that of T4L-D70N is 6.0 kcal/mol (Shashidharamurthy et al., 2005). Thus, under the assay conditions, T4L is predominantly in the folded state and does not aggregate. Steady state association between Hsp16.5 and dynamically populated non-native T4L is detected directly via changes in the fluorescence property of a bimane probe attached on the surface site, 151, of T4L (Sathish et al., 2003). The binding isotherms of Hsp16.5 and the Hsp16.5-P1 variant to T4L-L99A (Figure III-9a and b) are biphasic indicative of two-mode binding as previously reported for α-crystallin. Binding was confirmed by SEC of Hsp16.5/T4L mixture followed by fluorescence detection (data not shown) (Sathish et al., 2004). The quenching observed at low molar ratio of Hsp16.5 to T4L has been shown to reflect the extensive unfolding of T4L when bound with low affinity (Sathish et al., 2003). Truncation of the N-terminal region leads to a right-shifted monophasic binding isotherm indicating a reduced level of binding. We used a phenomenological two-mode binding model previously derived from analysis of α-crystallin and Hsp27 interaction with T4L (Sathish et al., 2003) to rank the affinity of the Hsp16.5 variants for T4L. Dissociation constants obtained from non-linear least squares fits demonstrate that the Hsp16.5-P1 variant has significantly higher affinity than the WT while the N-terminal truncation Hsp16.5-TR is best modeled with a single low affinity mode. High-affinity bound T4L has a higher quantum yield in the Hsp16.5-P1 variant and a larger blue shift of its maximum intensity wavelength relative to the WT suggesting a more hydrophobic environment of bound T4L.

Addition of Hsp16.5-P1N to 7 or 10 μM T4L-L99A leads to visible aggregation and light scattering. The aggregates consist of both Hsp16.5 and T4L which is indicative of saturation binding where the sHSP oligomer becomes insoluble. Therefore, the level of binding was reduced by obtaining the binding isotherm at 5 μM T4L-L99A (Figure III-9b) and by using T4L-D70N which is more stable than T4L-L99A by ≅ 2 kcal/mol (Figure III-9c). Hsp16.5-P1N shows a significantly higher level of binding than the WT. In the presence of T4L-D70N, little or no binding is observed for the WT while both insertion mutants display biphasic binding at substrate concentrations as low as 7 μM. These qualitative results indicate that both Hsp16.5-P1 and Hsp16.5-P1N represent activated forms of Hsp16.5 displaying significant enhancement of binding to non-native states of T4L. As discussed below, the mechanism of activation may involve the increased exposure of the N-terminal region.

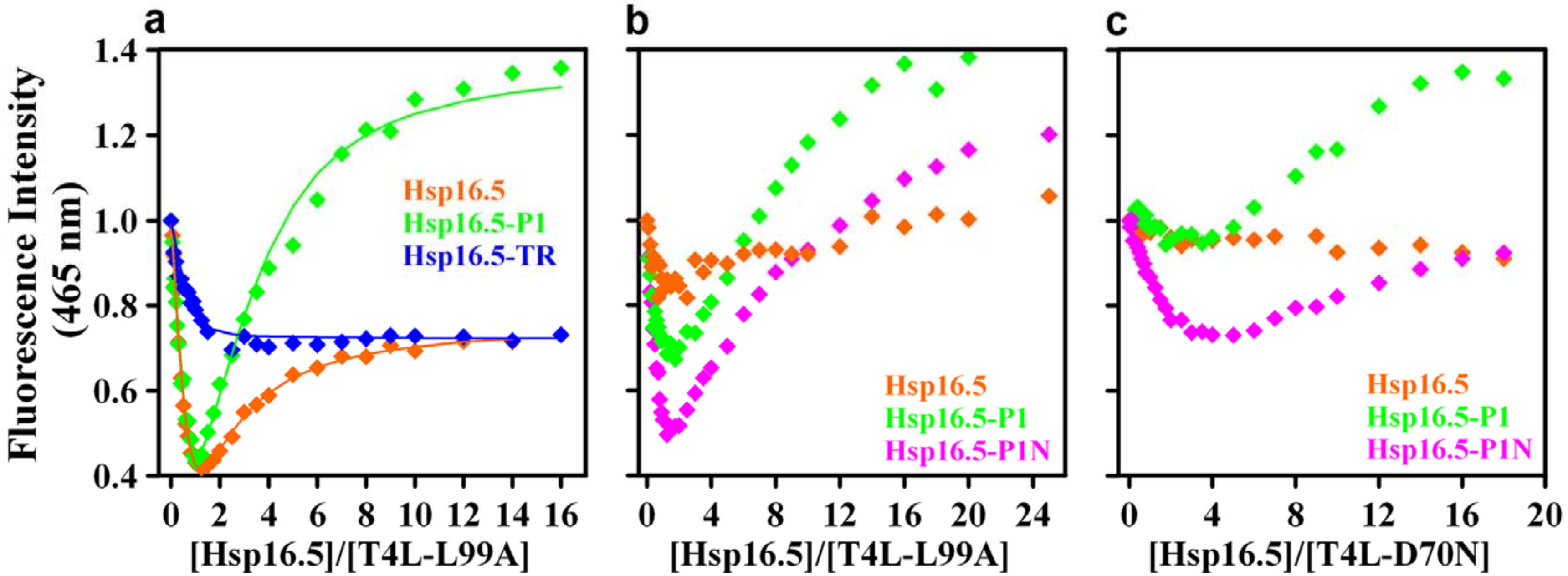

Figure III-9

Hsp16.5 and its variants display differences in binding to destabilized mutants of T4L. ***(a)*** *Truncation of the N-terminal region leads to a loss of two-mode binding while Hsp16.5-P1 shows an increased level of binding relative to WT. The Hsp16.5 and Hsp16.5-P1 curves were generated with 10µM T4L-L99A and the Hsp16.5-TR curve with 7µM T4L-L99A. The binding-induced changes in the maximum emission wavelengths are as follows: ΔλHsp16.5=10 nm, ΔλHsp16.5-P1=14 nm, ΔλHsp16.5-TR =10 nm.* ***(b)*** *and* ***(c)*** *Enhancement of Hsp16.5-P1 and Hsp16.5-P1N binding to two T4L destabilized mutants with two different free energy of unfolding. The curves were generated with 5µM T4L-L99A in (b) and 14µM T4L-D70N in (c). All curves were generated at pH7.2 and 37ºC. Reprinted with permission from (Shi et al., 2006)*

3.4 Discussion

By combining rational insertion mutagenesis with a hybrid cryoEM and EPR structural approach and a unique binding assay, we derive a model for the interplay between the three sequence modules (N-terminal domain, α-crystallin domain, and C-terminal extension) that underlies the transition to polydispersity, and defines the role of polydispersity in substrate binding. The finding that disruption of the Hsp16.5 N-terminal region profoundly affects the packing interactions of the α-crystallin domain establishes the paradigm that sequence divergence in the N-terminal domain of sHSP is a primary mechanism for tuning the oligomer symmetry and degree of order. An extreme manifestation of this mechanism is the evolved role of the N-terminal domain of αA-crystallin and Hsp27 in controlling the global assembly of the native oligomer and its dynamic properties (Berengian et al., 1999; Bova et al., 2000; Merck et al., 1992). Multiple assemblies were also recently reported from cryoEM analysis of Hsp26 (White et al., 2006). Although deletion of the N-terminal region does not alter the symmetry and size of the Hsp16.5 oligomer (Koteiche & Mchaourab, 2002), sequence changes in the N-terminal region lead to the formation of larger symmetrical or polydisperse assemblies. The findings that the expanded Hsp16.5-P1 and Hsp16.5-P1N have activated binding suggest that the intrinsic plasticity is central to the chaperone mechanism.

The structural basis of Hsp16.5 oligomer plasticity is a dimer-dimer interface of minimal contacts whose angular adjustment is coupled to the flexible C-terminal extension. The critical role of the latter in conferring packing flexibility across the superfamily is highlighted by comparison of the crystal structures of Hsp16.9 and Hsp16.5 where two distinct conformations of the C-terminal extension allow alternative assemblies to be formed despite a largely conserved α-crystallin domain (Van Montfort et al., 2001a). The conformational adaptability is based on a hinge mechanism and is guided by contacts with a hydrophobic groove on one side of the α-crystallin domain β-sandwich (Van Montfort et al., 2001a). In Hsp16.5-P1, we find that the interface angle is 60° around the 3-fold window and 90° around the 4-fold window, and that the C-terminal extension can adapt to form a linker at both interface angles. Van Monfort et al. pointed out the similarity of this feature to the VP1 protein of simian virus which has a flexible extension that allows variability in the geometry of the assembly while maintaining equivalent subunit-subunit interfaces (Van Montfort et al., 2001a). That this structural motif is conserved across the superfamily is suggested by the presence of the conserved sequence IXV in the C-terminal extension (de Jong et al., 1998) and the lack of significant structural changes on the side of the β-sandwich where it binds.

The structure and binding characteristics of the Hsp16.5 insertion mutants can be framed into a mechanistic model for WT Hsp16.5 chaperone activity with broader relevance to the entire superfamily. Specific sequences in the N-terminal regions of sHSP have been shown to interact with substrates (Giese et al., 2005; Van Montfort et al., 2001a), a conclusion reinforced by the reduction in binding affinity upon deletion of this region in Hsp16.5. Previous SDSL-EPR and cryoEM data on WT Hsp16.5 have shown that helices from different subunits in the N-terminal region form a bundle at the oligomeric 4-fold symmetry axis (Koteiche & Mchaourab, 2002). Complex formation with substrate involving the N-terminal region may disrupt the packing of the helices. We hypothesize that this perturbation is transmitted to the C-terminal α-crystallin domain and influences the packing of dimers in the outer shell leading to an expansion of the oligomer. We observe an expansion relative to WT for both the symmetric variant Hsp16.5-P1 and the polydisperse variant Hsp16.5-P1N. It is possible that the inserted P1 peptide, which is covalently linked to the N-terminal region in both variants, may be mimicking the effect of bound substrate on the quaternary structure of the oligomer. Whether the structural transitions observed for Hsp16.5-P1 and Hsp16.5-P1N are the consequence of the dynamic properties of this peptide, its detailed sequence character, or the structural disruption of the N-terminal region cannot be conclusively established.

This mechanistic model for chaperone activity is consistent with negative stain EM studies which report an expansion of the Hsp16.5 oligomer following binding to single chain monellin (Kim et al., 2003b). Furthermore, exposure of the oligomer to the binding temperature of 65°C in the absence of the substrate results in a similar increase in diameter without change in the secondary structure (Kim et al., 2003a). Transition to either large symmetrical or polydisperse assemblies is accompanied by increased accessibility of the N-terminal region as demonstrated by the large 4-fold windows observed in the Hsp16.5-P1 structure. The incomplete and irregular shells of Hsp16.5-P1N may provide even greater access to the interior of the assembly. We propose that

WT binding-competent intermediates may resemble the expanded Hsp16.5-P1 and Hsp16.5-P1N variants and thus provide substrate increased access to the internal N-terminal regions.

From a more global perspective, our results resolve the conundrum between the α-crystallin domain encoding specific subunit contacts and the overall polydispersity of the oligomers. The polydisperse quaternary structures observed for mammalian sHSP such as α-crystallin can be explained in the same manner as Hsp16.5-P1N. Hsp16.5-P1 may also provide a structural and mechanistic model for the expansion of oligomers observed in mutants of α-crystallin associated with congenital cataract. It is noted that these mutants also display higher affinity to their substrates (Koteiche & Mchaourab, 2006).

It is likely that the N-terminal sequences of αA- and αB-crystallin induce polydisperse oligomers, and simultaneously confer and modulate the ability to undergo dynamic subunit exchange. Subunit dissociation provides transient exposure of the N-terminus beyond the steady state level of accessibility associated with polydispersity. The steady state fraction of dissociated multimers may be an added mechanism by which mammalian sHSP control their activation state.

CHAPTER IV

INSIGHTS INTO THE MECHANISM OF SHSP CHAPERONE FUNCTION ARE REVEALED BY CRYO-ELECTRON MICROSCOPY AND SINGLE PARTICLE ANALYSIS

4.1 Introduction

Horwitz first reported that α-crystallin can function as a molecular chaperone that suppresses substrate aggregation induced by high temperatures, in addition to its known function as a lens structural protein (Horwitz, 1992). Compared to other Hsp families, sHSPs efficiently protect a wide range of proteins from aggregation. The binding capacity of the sHSPs has a maximum of 1 to 1 molecular stoichiometry (Koteiche & Mchaourab, 2006; Mchaourab et al., 2002). This means for example that a sHSP oligomer with 30 monomers can bind up to 30 substrate molecules. The sHSP and substrate complex, which is larger than the sHSP oligomer alone, is highly soluble and stable. The binding action of sHSPs does not require energy input from ATP and further sHSPs do not promote the refolding of substrates. The substrate molecules in sHSP complexes can be effectively refolded in the presence of Hsp70 and ATP (Arrigo, 2007; Nakamoto & Vigh, 2007; Narberhaus, 2002).

Biophysical and biochemical studies suggest that sHSPs are able to recognize an early stage of unfolded proteins and that the bound substrates are folding-competent (Das et al., 1999; Das et al., 1996; Ehrnsperger et al., 1997; Lee et al., 1997; Lindner et al., 2001; Sathish et al., 2003). It is generally accepted that hydrophobic contacts underlie the recognition and binding of unfolded proteins by sHSPs. Deletion of the N-terminal region, which is enriched with hydrophobic residues, causes the dissociation of α-crystallin to smaller multimers, but deletion of the N-terminal region of Hsp16.5 does not disturb formation of an oligomer with 24 subunits. Neither deletion has an effect on the secondary structure of the α-crystallin domain, nevertheless, both deletion mutants possess diminished chaperone activities (Koteiche & Mchaourab, 2002; Kundu et al., 2007; Studer et al., 2002). The substrate interaction sites located within α-crystallin domain have been mapped to β-strands #3, 8, 9 using hydrophobic probe ANS (8-anilino-1-naphthalene sulfonate) or synthesized peptides corresponding to αB-crystallin sequences for protein pin array assay(Ghosh et al., 2005; Ghosh et al., 2006; Sharma et al., 1998a; Sharma et al., 1998b) The C-terminal region is enriched with hydrophilic residues that contribute to the solubility of the sHSP oligomer and sHSP-substrate complex. In crystal structures of Hsp16.5 and Hsp16.9, a well conserved I-X-I/V motif in the C-terminus is responsible for stabilizing the dimer interaction in the oligomer, through the interaction of a hydrophobic groove between β-strand 4 and 8 of neighboring subunits (Kim et al., 1998a; Van Montfort et al., 2001a). Disruption of C-terminus of sHSP by deletion or mutation results in poor solubility and reduced the chaperone activity (Bova et al., 2000; Li et al., 2007; Thampi & Abraham, 2003).

The sHSPs exhibit similar chaperone functions but display a continuum of quaternary structures, from poly-disperse to mono-disperse assemblies, and with different symmetries (Haley et al., 2000; Shi et al., 2006). In addition, oligomeric assemblies of sHSPs are dynamic in response to aging, temperature, pH, ionic strength, and protein concentration. Subunit exchange constantly occurs between oligomers, which may contribute to increased accessibility of sHSP substrates to buried hydrophobic regions (Bova et al., 1997; Bova et al., 2002). Elevated temperatures normally enhance the subunit exchange rate and chaperone activity. An extreme case of this dynamism is Hsp26, which completely dissociates into dimers at elevated temperatures. Binding to substrate drives HSP26 dimers into complexes with a 50% increase in the diameter (Haslbeck et al., 1999). Another regulatory mechanism for mammalian sHSPs is phosphorylation on serine residues, which occurs rapidly when cells are exposed to stress, cytokines, and growth factors (Butt et al., 2001; Koteiche & Mchaourab, 2003). Phosphorylation alters sHSP assembly equilibrium, sometimes transforming large oligomers to tetramers or dimers, and regulates chaperone activities (Koteiche & Mchaourab, 2003; Shashidharamurthy et al., 2005).

The molecular mechanism of sHSP chaperone function remains elusive due to the diversity of sHSP structures, experimental conditions, and model substrates. The chaperone activity of sHSPs typically is estimated by measuring the changes in light scattering of a protein solution or the recovery of enzymatic activity of substrate proteins, when substrate proteins are incubated with or without the presence of sHSPs after heat or denaturant treatments (Reddy et al., 2006; Sun & MacRae, 2005b). The Mchaourab lab has developed a steady state assay for quantitative assessment of sHSP binding to substrates at physiological temperatures using a set of engineered T4 lysozyme mutants as model substrates, whose unfolding free energies range from 5 to 10 kcal/mol (Mchaourab et al., 2002). The quantitative analysis suggests that sHSPs have two binding modes: a high-affinity binding mode and a low-affinity binding mode, which are proposed to correlate to different unfolding states of T4 lysozyme substrate (Koteiche & Mchaourab, 2003). In this context, the mechanism of cataractogenic αA-crystallin mutation (R116C) is explained as enhanced binding ability (Koteiche & Mchaourab, 2006), which leads to mis-regulated protein aggregation control and opacification in the lens.

We reported a set of Hsp16.5 variants with diverse quaternary structures, which correlate with enhanced or diminished substrate binding affinity. To further understand the mechanism of small heat-shock protein chaperone activity, we investigated the interactions between sHSP and substrate, with particular attention to the relationship between sHSPs quaternary structure and their binding ability. We use cryo-EM and single particle reconstruction to study the oligomeric structure of Hsp16.5 variants alone and the complexes formed by Hsp16.5 variants and model substrate. Our results show homogenous Hsp16.5-WT assemblies are transformed into a continuum of oligomeric states upon T4L substrate binding. The structure of the Hsp16.5TR/T4L complex confirms that its oligomeric shell, which is formed by 24 copies of the α-crystallin domain, is able to bind substrate with low-affinity. We find differences between the unbound structure and the bound structure that lead us to conclude that binding of T4L to Hsp16.5-P1 and Hsp16.5-WT induces a conformational change in the N-terminal region. Our data suggest that both the α-crystallin domain and N-terminal region serve to stabilize the substrate inside the sHSP oligomer and that the dynamic oligomeric state of sHSPs contributes to substrate binding. Furthermore, we observe similar conformational changes in the N-terminal region in the Hsp16.5-R107G mutant reconstruction, suggesting that it may represent an activated state even without substrate. Taken together, these results show the dynamic oligomeric state regulates the chaperone capability of sHSP and this is driven by conformational changes in regions that may be important for substrate interaction.

4.2 Results

Hsp16.5-Truncation (TR) and Hsp16.5-TR/T4L complex

The quaternary structural fingerprints of Hsp16.5 truncation (TR) were mapped though measuring the proximities between nitroxide pairs labeled on selected sites. The results suggested that the overall structure and symmetry remains unchanged after the N-terminal sequence is removed (Koteiche & Mchaourab, 2002). The cryoEM reconstruction showed that Hsp16.5-TR oligomer forms homogeneous assembly and holds the same quaternary structure as Hsp16.5-WT. This is also indicated by size-exclusion chromatography and light scattering (Shi et al., 2006). The only difference compared to Hsp16.5-WT reconstruction is the missing internal density of the truncated N-terminal region. The binding isoforms of Hsp16.5-TR to T4 lysozyme substrate indicates monophasic binding and is best modeled with a single low affinity mode, compared to the two binding mode of Hsp16.5-WT (Shi et al., 2006).

After incubation with bimane labeled T4 lysozyme at a molar ratio of 4:1 (sHSP monomer to T4L), the Hsp16.5-TR+T4L mixture was separated by size-exclusion chromatography. The similarity between the elution profiles of Hsp16.5-TR and Hsp16.5-TR+T4L complex indicates that substrate binding does not change the hydrodynamic properties of Hsp16.5-TR. The cryo-EM imaging and single particle reconstruction indicates that the Hsp16.5-TR+T4L complex holds a similar size and symmetry as Hsp16.5-TR. The octahedral symmetry was applied for single particle 3D reconstructions of both Hsp16.5-TR and Hsp16.5-TR/T4L, using the density map of Hsp16.5-WT as the starting model. The resolutions of Hsp16.5-TR and Hsp16.5-TR/T4L reconstructions are around 10Å and 12Å respectively, and were estimated by the 0.5 FSC threshold. The diameter of the Hsp16.5-TR assembly with or without substrate does not change, indicating that the overall quaternary structure is preserved upon substrate binding.

The 3D reconstructions of the Hsp16.5-TR and Hsp16.5TR-T4L complexes are shown cropped in half to reveal the interior in Figure IV-1. The Hsp16.5-TR structure has a hollow interior due to the missing N-termini. In contrast, the central cavity in the

Hsp16.5-TR/T4L complex is filled with additional density, presumably T4L substrate molecules. In the absence of the N-terminal region, T4L must be tethered through contacts with the α-crystallin domain shell of the Hsp16.5-TR oligomer. The absence of density connecting the central cavity density to the outer shell in Hsp16.5-TR/T4L reconstructions can be explained by either these contacts not being extensive or by their being highly disordered. It seems likely, given the lack of density in direct contact with the alpha-crystallin domain, that limited binding to the α-crystallin domain may serve to guide the unfolded T4 lysozyme to the inner region of the oligomer.

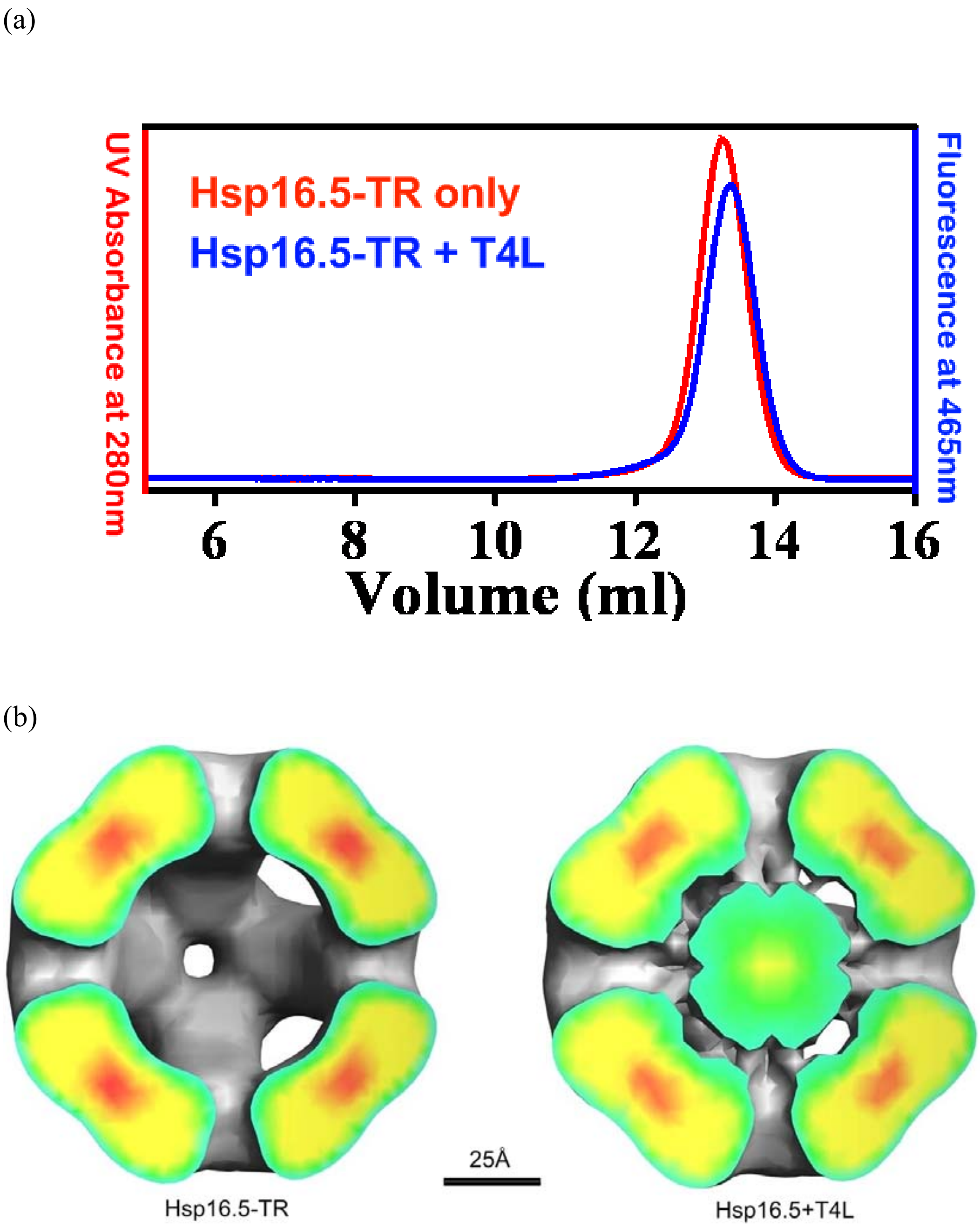

Figure IV-1

(a) *Comparison of size exclusion chromatography results for Hsp16.5-TR and Hsp16.5TR-T4L complexes. The similarity of their elution profiles indicates that substrate binding does not change the hydrodynamic properties of Hsp16.5-TR.* ***(b)*** *Comparison of the 3D reconstructions of the Hsp16.5-TR and Hsp16.5TR-T4L complexes shown cropped in half to reveal the interior. The Hsp16.5-TR structure shows a hollow interior due to the missing N-termini. The density inside the Hsp16.5TR-T4L complex is assigned to the bound T4L substrate.*

Hsp16.5-P1 and Hsp16.5-P1/T4L complex

Hsp16.5-P1 was generated by inserting 14 amino acids derived from the human Hsp27 sequence into the homologous site in Hsp16.5 at the junction between the N-terminal region and α-crystallin domain. Size-exclusion chromatography and light scattering results show that Hsp16.5-P1 forms a monodisperse oligomer with a molecular mass (~850 kDa) approximately double that of Hsp16.5-WT (~400kDa) (Shi et al., 2006). Cryo-EM reconstruction revealed an octahedral structure with a diameter of 182Å, 50% larger than that of Hsp16.5-WT (120 Å). A pseudo-atomic model was built by docking the atomic coordinates of the Hsp16.5-WT α-crystallin domain into the Hsp16.5-P1 density map. The resulting pseudo-atomic model consists of 48 monomers, twice that of Hsp16.5-WT. This model is confirmed by the recent crystal structure of Hsp16.5-P1 solved by Mchaourab lab (personal communication, Dr. Mchaourab). The oligomeric structure of Hsp16.5-P1 is characterized by unique four-fold openings, which are much larger than the three-fold openings in Hsp16.5-WT. The Hsp16.5-P1 possesses significantly higher binding affinity for substrate than Hsp16.5-WT, indicated by biphasic substrate binding isoforms (Shi et al., 2006).

After incubated with bimane labeled T4 lysozyme at a molar ratio of 2:1 (monomer to T4L), the Hsp16.5-P1+T4L mixture was purified by size-exclusion chromatography. As was the case for Hsp16.5-TR, elution profiles of Hsp16.5-P1 and Hsp16.5-P1/T4L do not change noticeably, suggesting similar hydrodynamic properties between Hsp16.5-P1 and Hsp16.5-P1/T4L. The cryo-EM particle images of Hsp16.5-P1 and Hsp16.5-P1/T4L are close in size and symmetry. Although a 10Å reconstruction of Hsp16.5-P1 has been obtained from a 300KV microscope (Shi et al., 2006), the Hsp16.5-P1 data collected on a 120KV microscope was used as a control for Hsp16.5-P1/T4L. Octahedral symmetry was applied during single particle reconstruction and refinement. The resolution of the Hsp16.5-P1 and Hsp16.5-P1/T4L reconstructions are 10Å and 12Å estimated by the 0.5 FSC threshold, respectively.

The conserved oligomeric size of the Hsp16.5-P1 assembly with or without substrate shows an unaltered α-crystallin shell, which does not appear to have any gross changes upon substrate binding. The cryoEM reconstructions of Hsp16.5-P1 and Hsp16.5P1/T4L are shown cropped in half in Figure IV-2. The inner density in Hsp16.5-P1 is assigned to 48 copies of the N-termini and the inserted 14-residue sequence. By combining modeling of cryo-EM density maps and SDSL-EPR spectroscopy, a portion of the Hsp16.5 N-terminal region was shown to have an α-helical conformation and four N-terminal α-helices form a bundle along the 4-fold symmetry axis (Koteiche et al., 2005). Site-directed spin labeling EPR data indicates that the structure and interaction in the N-terminal region are preserved in both Hsp16.5-WT and Hsp16.5-P1 (Shi et al., 2006). The strong electron density in Hsp16.5-P1 may be due to the association of partially ordered N-termini bundles. We observed considerable redistribution of the internal density inside the Hsp16.5P1/T4L reconstruction, suggesting that the N-termini undergo large conformational changes upon substrate binding and that the N-terminal associations are disrupted by interactions with T4L substrates. The weaker electron density in Hsp16.5P1/T4L implies that both the N-termini and the substrates are likely disordered. The extensive connection between the internal density and α-crystallin domain shell suggests that the substrates may also interact with the lining of α-crystallin domain shell at the same time.

(a)

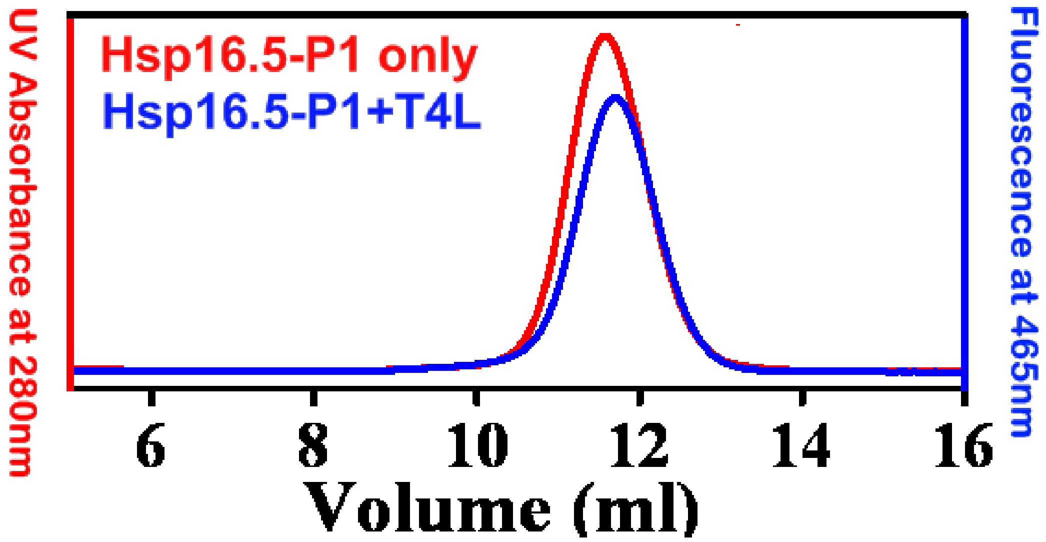

(b)

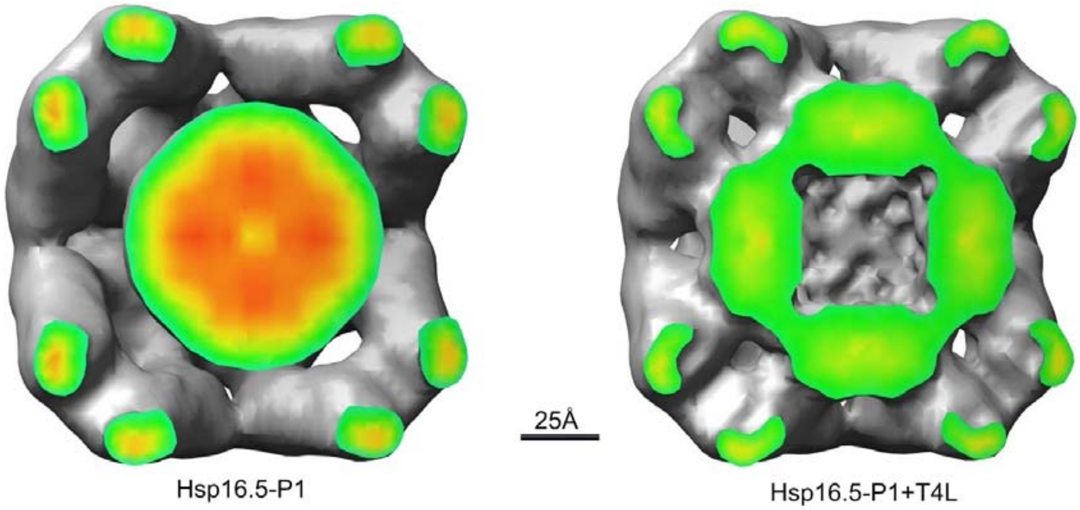

Figure IV-2

(a) *Size exclusion chromatography of Hsp16.5-P1 and Hsp16.5P1-T4L complexes. The similarity of their elution profiles indicates that the Hsp16.5P1-T4L complex has the same hydrodynamic properties as Hsp16.5-P1.* ***(b)*** *Comparison of 3D reconstructions of the Hsp16.5-P1 and Hsp16.5P1-T4L complexes shown cropped in half. The inner density in Hsp16.5-P1 is assigned to 48 copies of the N-terminus. The Hsp16.5P1-T4L structure indicates that the bound T4L disrupts the packing of the N-termini.*

Hsp16.5-WT and Hsp16.5-WT/T4L complex

A 2.9Å crystal structure of homogenous Hsp16.5-WT oligomer was published in 1998 (Kim et al., 1998a). The octahedral oligomer with a diameter of 120Å consists of 24 monomers and contains eight triangular and six square windows. The N-terminal 32 residues are disordered in the crystal structure, but the cryoEM reconstruction shows additional density in the central cavity (Haley et al., 2000). The homogenous oligomer is transformed into heterogeneous assemblies by inserting a 14-residue sequence from human Hsp27 into the N-terminal region, presumably due to the disruption of the α-helical bundle of N-termini (Shi et al., 2006).

Size exclusion chromatography of Hsp16.5-WT/T4L shows three elution peaks, which is illustrated by the elution plot of WT/T4L (molar ratio 8:1) in (Figure IV-3). By varying the molar ratio between Hsp16.5-WT and T4L, and by varying the incubation temperature, we can change the relative intensities of the three peaks. The first peak runs with the void volume of the column, suggesting a large molecular weight. The second peak has a similar retention time range to that of Hsp16.5-P1N, indicating heterogeneous particle sizes. The third peak is similar to that of Hsp16.5-WT alone, indicating monodisperse assemblies. CryoEM images of peak1 of WT/T4L (molar ratio 6:1, data not shown) indicate that this fraction consists of clustered Hsp16.5 particles presumably associated by bound T4L (see Figure IV-3). Interestingly, individual Hsp16.5 assemblies can be discerned in these large aggregates. The particles in peak-2 WT/T4L (molar ratio

6:1, data not shown) appear to be heterogeneous complexes with a wide range of sizes, similar to Hsp16.5-P1N (Shi et al., 2006). The observation of heterogeneous particles is consistent with previous results of Hsp16.5-WT activated by elevated temperature (Kim et al., 2003a; Kim et al., 2003b). Particle images of peak-3 are close to that of Hsp16.5-WT alone, likely corresponding to a state similar to Hsp16.5-TR/T4L and Hsp16.5-P1/T4L complexes.

The cryoEM reconstructions were conducted for homogenous peak-3 of Hsp16.5-WT/T4L (molar ratio 4:1, data not shown), as well as for Hsp16.5-WT as a control, using the previous 13Å Hsp16.5-WT density map as an initial model (Haley et al., 2000). A series of different percentage (35%, 55%, 75%, and 95%) of particles are included in reconstruction and refinement processes. This selection process is one way to deal with heterogeneous datasets. The Hsp16.5-WT and Hsp16.5-WT/T4L cryoEM reconstructions are shown cropped in half in Figure IV-4. All of the reconstructions of Hsp16.5-WT show centralized density, consistent with previous results, whereas the reconstructions of Hsp16.5-WT/T4L contain internal density with a different distribution than that of Hsp16.5-WT. The reconstruction that included 35% of the particles clearly shows expanded density in the interior, suggesting that the N-terminal region undergo a conformational change upon substrate binding, similar to that of Hsp16.5-P1/T4L. The incremental change in the central density of the Hsp16.5-WT/T4L reconstructions when more particles are included may be caused by heterogeneous species of particles being present in peak-3, in which both Hsp16.5-WT alone and complexes with bound substrates co-exist.

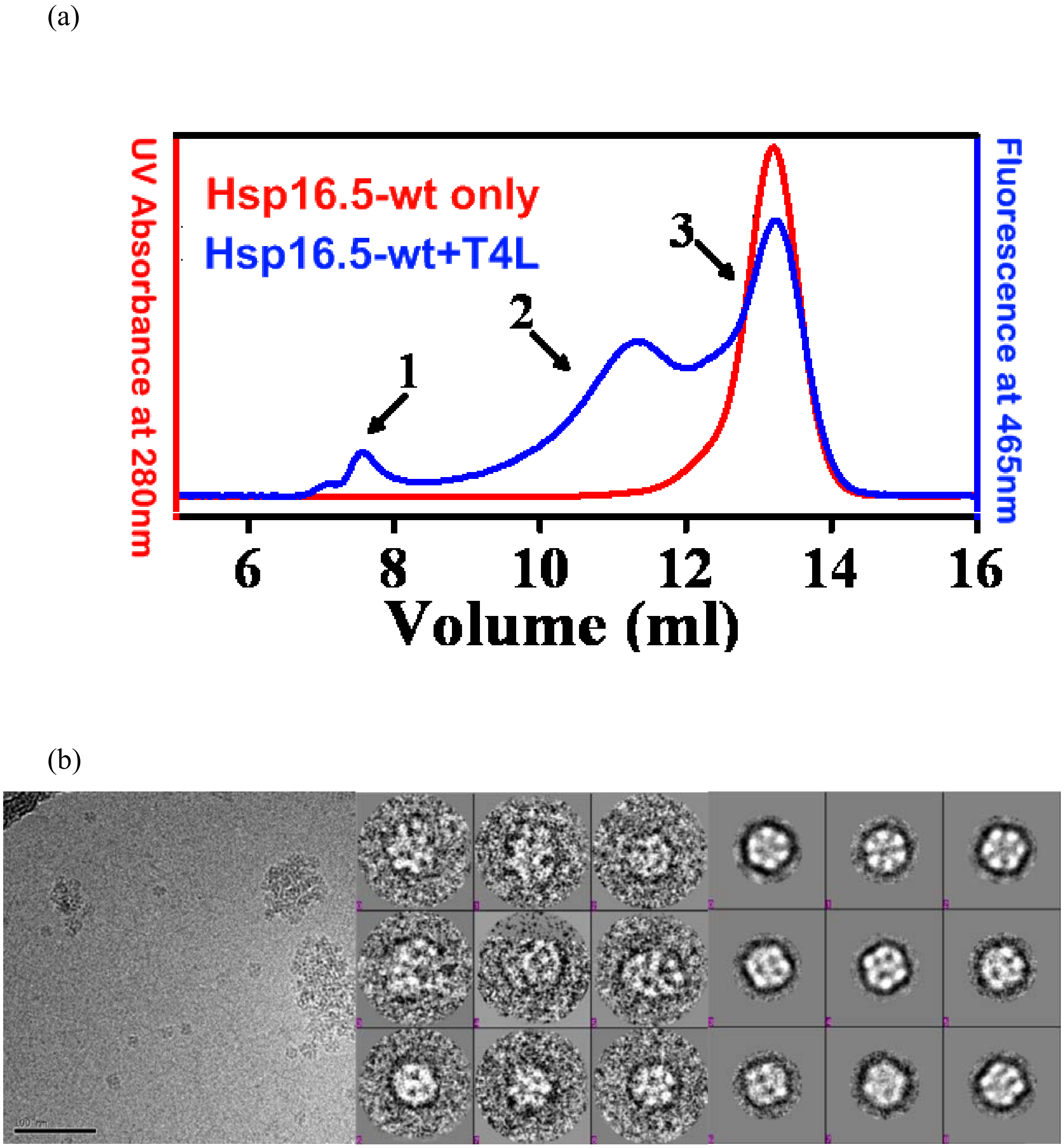

Peak-1 Cryoelectron micrograph **Peak-2 Class-sum images** **Peak-3 Class-sum images**

Figure IV-3

***(a)** Size exclusion chromatography of Hsp16.5 and Hsp16.5-T4L complexes. Peak3 in the Hsp16.5 elution profile is consistent with a monodisperse state and a homogeneous quaternary structure. Other peaks in the Hsp16.5-T4L elution profile indicate oligomers with a range of sizes. **(b)** A cryoelectron micrograph of peak-1 indicates that this fraction consists of large aggregates. Representative class-sum images of peak-2 suggest heterogeneous quaternary structures. Representative class-sum images of peak-3 show that oligomers in this fraction have the same size and symmetry as Hsp16.5-WT alone.*

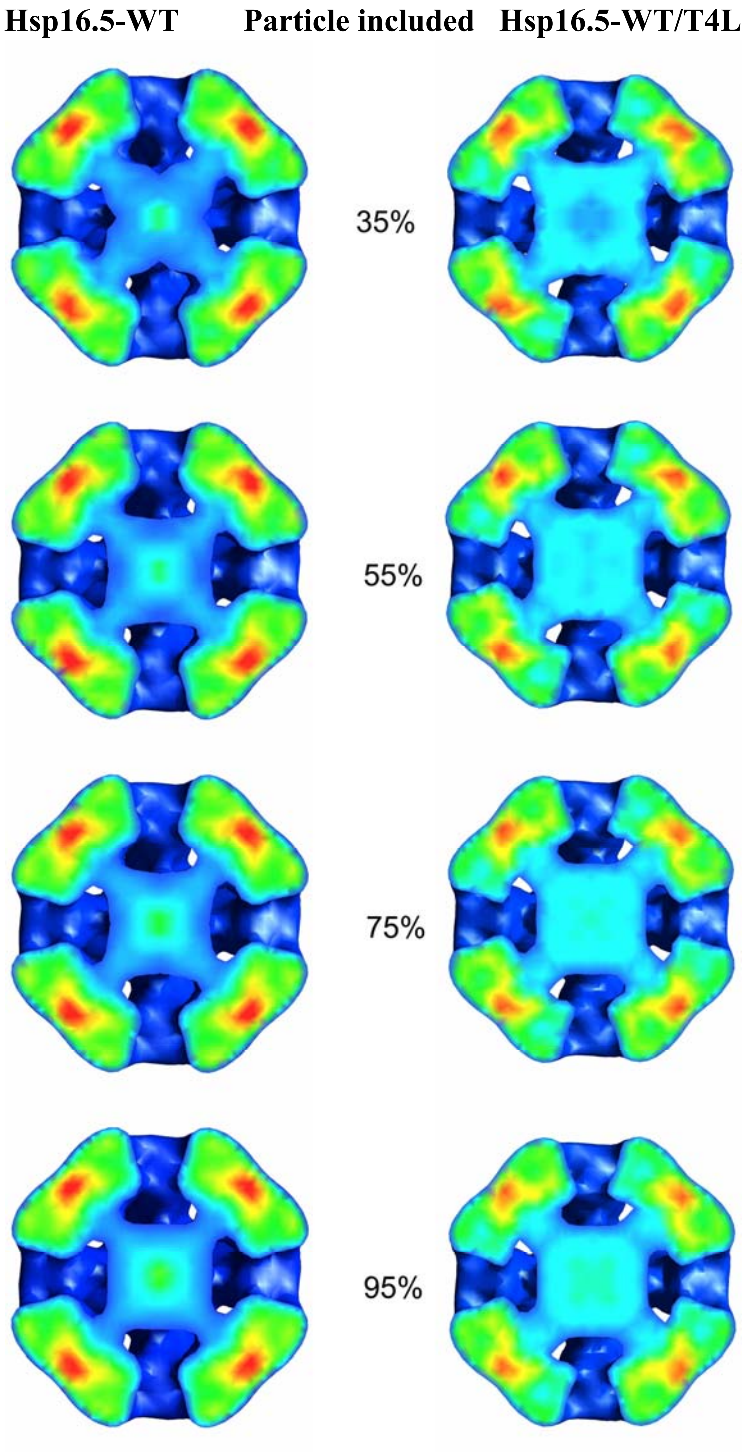

Figure IV-4

CryoEM reconstructions of Hsp16.5-WT and Hsp16.5-WT/T4L are shown cropped in half. Four different percentages of particles are included for 3D reconstruction and refinement. The Hsp16.5-WT/T4L reconstruction with 35% particles possesses the most apparent internal density deviation with and without T4L substrate.

Hsp16.5-R107G

A missense mutation R120G in αB-crystallin has been identified in a French family with inherited desmin-related myopathy (DRM)s (Vicart et al., 1998). Immunolabelling in a patient muscle biopsy and transfected muscle cells shows that there are accumulated abnormal deposits that contain both desmin and R120G-αB-crystallin. Furthermore, a missense mutation R116C at an homologous position in αA-crystallin is genetically associated with autosomal dominant congenital cataract (Litt et al., 1998). Both R116C of αA-crystallin and R120G of αB-crystallin show significantly reduced ability in suppressing protein aggregation. Perturbations of secondary and tertiary structure of the two mutants are suggested by UV circular dichroism (UV-CD) spectra (Cobb & Petrash, 2000; Treweek et al., 2005). Size exclusion chromatography reveals increased polydispersity and oligomeric mass of the two mutants (Bova et al., 1999; Mchaourab et al., 2007). The conservation of this Arg residue throughout the sHSP family suggests a structural and functional importance. In the crystal structure of Hsp16.5-WT, the homologous Arg107 is located in β7 of the α-crystallin domain. This negatively charged residue makes a hydrogen bond (~2.9Å) with Gly41 in the loop between β1 and β2, and forms a weak salt bridge (~4.5Å) with Glu98 in β6, which is contributed from a neighbor monomer. Thus, these interactions stabilize both β-sheet folding and dimerization.

Interestingly, the Hsp16.5-R107G mutation does not alter the overall oligomeric structure appreciably. From the cryo-EM particle images and class-sums, there are no differences evident between Hsp16.5-R107G and Hsp16.5-WT. Single particle reconstruction of Hsp16.5-R107G was performed with octahedral symmetry using the 13Å resolution Hsp16.5-WT density map as an initial model (Haley et al., 2000) and revealed similar external oligomeric structure. However a markedly different internal density distribution is observed by examining sections of the reconstruction (see Figure IV-5). The internal density of Hsp16.5-R107G is considerably expanded and is close to the α-crystallin domain shell, which is in stark contrast to that observed for the HSP16.5-WT internal cavity. A series of reconstructions with different percentages of particles show the same internal density configuration, suggesting that all particles in the dataset are homogeneous in this structural change. We speculate that removing the negatively charged Arg destabilizes β1 and β6, and consequently induces conformational changes in the N-terminal region.

Figure IV-5

In the crystal structure of Hsp16.5-WT, the homologous Arg107(Green) is located in β7 of the α-crystallin domain. This negatively charged residue makes a hydrogen bond (~2.9Å) with Gly41(Yellow) in the loop between β1 and β2, and forms a weak salt bridge (~4.5Å) with Glu98(Orange) in β6, which is contributed from a neighbor monomer. Thus, these interactions stabilize both β-sheet folding and dimerization.

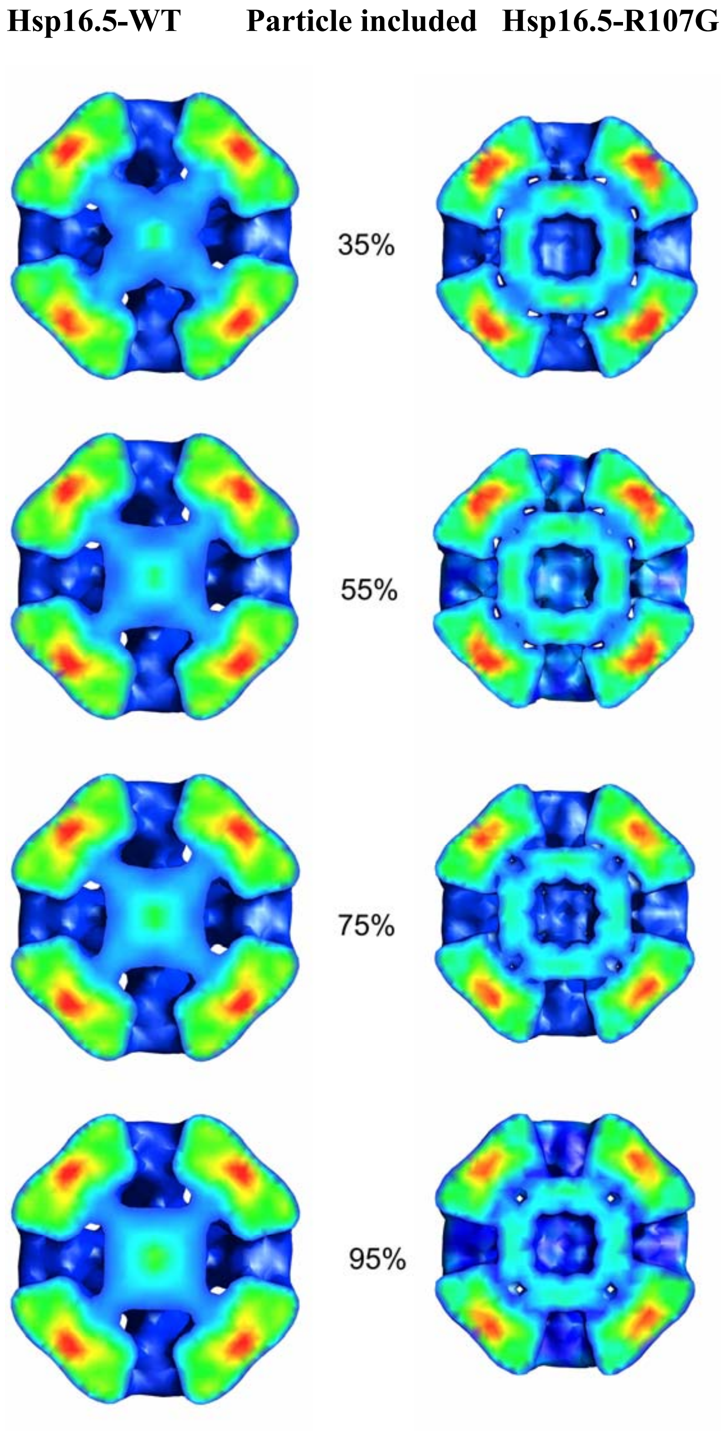

Figure IV-6

CryoEM reconstructions of Hsp16.5-WT and Hsp16.5-R107G are shown cropped in half. Four different percentages of particles are included for 3D reconstruction and refinement. All Hsp16.5-R107G reconstructions show extensive density deviation compared to the centralized density in Hsp16.5-WT

4.3 Discussion

The sHSPs have been reported to have a wide range of cellular functions, including bestowing thermo-tolerance to cells (Andley, 2007; Arrigo et al., 2007). In general, it is accepted that sHSPs compete with aggregation processes by interacting with aggregation-prone intermediates of cellular proteins. Consequently these intermediates are maintained in soluble complexes with sHSPs, from where they may be refolded or degraded by other molecular chaperones or proteases (Ehrnsperger et al., 1997). In the absence of detailed structural information, it remains unclear what structural attributes make sHSPs suited for their chaperone activity. In an effort to understand the nature of the interaction of sHSPs with substrate proteins, we have chosen engineered T4 lysozyme as a model substrate, incubating it with a series of Hsp16.5 variants previously reported by us (Shi et al., 2006). This system has a number of advantages: the destabilized T4L mutants simulate the delicate equilibrium between folded and unfolded states of cellular proteins. Substrate binding occurs under mild controlled conditions, which are closer to the normal physiological environment rather than the harsh conditions used in the aggregation suppression assay. Therefore, the resulting sHSP-substrate complexes mirror the natural products of chaperone activities in cell. The binding affinity and capacity of the sHSP-substrate complex at steady state can be analyzed quantitatively (Mchaourab et al., 2002; Sathish et al., 2003). Stable complexes consisting of Hsp16.5 variants and T4L are purified by SEC and investigated by cryoEM. From single particle 3D reconstructions of these complexes, we observe local and global conformational changes in the Hsp16.5 variants upon substrate binding. From these structural studies, we gain some mechanistic insight into Hsp16.5 chaperone activity, which may also be applicable to mammalian sHSPs.

Enclosed substrate and dynamic oligomeric structure

In a study of substrate binding of GroEL by cryoEM, a 33kDa malate dehydrogenase substrate exhibited an evident protrusion from the binding region in the reconstruction (Elad et al., 2007). There are no marked extra density protrusions corresponding to substrates observed on the surface or around the window areas of the three complex reconstructions of Hsp16.5 and its variants. The increased density in the Hsp16.5-TR/T4L complex only exists inside of outer protein shell. We noticed a significant conformational change in the N-terminal region of the Hsp16.5-WT/T4L and Hsp16.5-P1/T4L complexes by cryoEM reconstruction. Because there is no increase in the hydrodynamic size of these three complexes, we believe that the substrates must be enclosed within the oligomers and are stabilized through interactions between both the N-termini and the α-crystallin domain shell of the oligomer. Another possibility is that the substrates are completely unfolded and coat the surface of the sHSP oligomer, but this does not explain the extra density and conformational changes observed inside of the complexes by cryoEM reconstruction.

According to the 2.9Å crystal structure of Hsp16.5-WT, it is estimated that 49% of the solvent-accessible surface in the interior of the assembly is formed by nonpolar residues, in contrast to 22% on the outside surface. A general feature in sHSP family is that the N-terminal region is enriched with hydrophobic residues and the importance of the N-terminal region in chaperone function has been demonstrated for many sHSP family members (Ghosh et al., 2006; Giese et al., 2005; Kundu et al., 2007; Stromer et al., 2004). There are eight triangular and six square windows on the surface of the Hsp16.5 assembly, with side lengths of 30Å and 17Å respectively (Kim et al., 1998a). The triangular windows are wide enough to allow small substrates (~20kDa) to diffuse in and out of the oligomer. In the case of Hsp16.5-P1, the square window is even larger, with a width of ~60 Å, and correspondingly higher chaperone activities are observed. We attribute the higher chaperone activity to the increased accessibility of internal binding sites within the N-terminal region and the α-crystallin domain shell. The relationship between accessibility of hydrophobic sites and chaperone activity is also shown in human α-crystallin, in a temperature dependent manner (Raman & Rao, 1997; Singh et al., 1995; Singh et al., 1994).

The increased oligomeric size of Hsp16.5-P1 also provides a larger space to enclose more or larger substrates. For Hsp16.5-WT and Hsp16.5-P1, the volume of oligomers increases about 3 times, from 905,000Å^3 to 3,156,000Å^3, and the volume of the internal cavity increases from 147,000Å^3 (diameter 65Å) to 1,022,700Å^3 (diameter 125 Å), about 7 times. In theory, there is enough room for 6 molecules of T4L (18kDa) in the internal cavity of Hsp16.5-WT, and 42 molecules inside of the Hsp16.5-P1 assembly without considering the N-termini. Taking into account the volume of the N-termini, the space is sufficient for 2-3 molecules in the Hsp16.5-WT cavity and 30 molecules in Hsp16.5-P1. Therefore, a 50% increase in oligomer diameter and twice number of subunits (24 to 48 monomers) result in a 10 fold increase in the number of substrates that can fit within the central cavity. Similarly, it has been noted that the diameter of Hsp26 also increases ~50% upon substrate binding, from 150Å to 230Å (Haslbeck et al., 1999). The stoichiometry of Hsp16.5-WT/substrate binding can reach up to a 1:1 molar ratio (Kim et al., 1998b; Mchaourab et al., 2002; Shi et al., 2006), in contrast to the calculated number (3 T4L molecules to 24 monomer) for the Hsp16.5-WT oligomer with smallest diameter. Therefore expansion is necessary to accommodate high numbers of substrate molecules per oligomer, and the Hsp16.5-WT oligomer has to dynamically re-organize to larger oligomeric state. This is in line with our observation that a fraction of Hsp16.5-WT/T4L complex show increased size and more structural heterogeneity (Haley et al., 2000). Thus, we believe that the dynamic organization of sHSP oligomers is of high importance to its chaperone capacity.

Activation of sHSPs

One possible route to achieve oligomer re-organization is subunit exchange, presumably in the form of dimer. Subunit exchange is observed in almost all of the investigated sHSPs, including Hsp16.5-WT, α-crystallin and Hsp27 (Bova et al., 2002;

Bova et al., 2000; Pasta et al., 2003). The dissociated subunits may expose buried hydrophobic sites, which would be able to sense and bind non-native substrates in the cell. Based on the observation that a 24-mer of Hsp26, which is inactive at low temperature, dissociates completely into dimeric species at elevated temperature and gains chaperone activity, one model has been developed stating that the sHSP oligomer is a storage state and it dissociates into its activated dimeric form in response to external stressors (Haslbeck et al., 1999). However, further experiments show that cross-linked Hsp26 and αB-crystallin, which are not able to dissociate, become activated with observable conformational changes upon elevated temperature and exhibit chaperone activity that is indistinguishable from native protein (Augusteyn, 2004; Franzmann et al., 2005). The concomitant conformational changes, oligomer reorganization and increased chaperone activity upon heat-shock were observed for Hsp16.5-WT as well as α-crystallin (Farnsworth et al., 1997; Kim et al., 2003a; Raman & Rao, 1997). A recent study shows that temperature activated IbpB, a sHSP from *E coli.*, retains the activated conformation and displays elevated chaperone activity even after removing the heat-shock stress (Jiao et al., 2007). These results suggest that the temperature-induced conformational changes are the driving force of sHSPs activation, which may also occur concomitantly with substrate binding. Furthermore, sHSP and substrate form large complexes, which are soluble and stable. The profound conformational changes observed in the Hsp16.5 variant/T4L complex reconstructions likely result from activation and simultaneous substrate binding.

In addition to the conformational changes observed in the Hsp16.5 variant/T4L reconstructions, we also saw a similar density deviation in the internal density of the Hsp16.5-R107G reconstruction. The CD spectrum indicates that the β-sheet content in R120G αB-crystallin and R116C αA-crystallin decreases compared to wild type, which is similar to a conformational transition of wild type αB-crystallin induced by elevated temperature (Bova et al., 1999; Shroff et al., 2000; Treweek et al., 2005). Although the Arg mutations of α-crystallin cause reduced or completely lost chaperone activity in aggregations suppression assay, further analysis indicates that R120G αB-crystallin gains hyperactivity, which results in aggregation with model substrates (Koteiche & Mchaourab, 2006; Treweek et al., 2005). Cobb and Petrash reported that R116C αA-crystallin shows enhanced binding to membranes, which may be related to the pathogenesis of this mutation and its tendency to cause cataracts (Cobb & Petrash, 2000). Similarly, the R107G mutation in Hsp16.5 might destabilize the β-sheet interaction in a monomer and between monomers in a dimer, and consequently induce the conformational changes that we observed. We speculate that the observed conformational changes in Hsp16.5-R107G mirror an activated state that would normally result from heat-shock treatment. The structural perturbation brings the N-terminal region closer to the windows of the protein shell, which may increase the accessibility of hydrophobic sites within the N-termini or lower the energy barrier for substrate interaction. Consistent with this hypothesis, the significant gain of substrate binding ability of Hsp16.5-P1N may be attributed to the disruption of N-termini packing arrangement by the inserted sequence.

Our results provide insight into the possible mechanisms by which Hsp16.5 and Hsp16.5 variants accomplish their task of stabilizing a model substrate, an engineered T4L mutant. We proposed that the substrate molecules are secluded inside the oligomer, which prevents them kept from undergoing abnormal interaction and aggregation. Forming a larger sHSP oligomer by incorporating more subunits is an efficient strategy to increase the substrate binding capacity, as well as provide higher accessibility to the interaction sites in the N-terminal region. The oligomer re-organization is presumably accomplished through subunit exchange, although this is not a prerequisite for activation and chaperone activity. The similar internal density distribution observed in Hsp16.5-R107G, Hsp16.5-WT/T4L and Hsp16.5-P1/T4L may reflect the activated state of these oligomers. Based on the evidence in the literature, we speculate that mammalian sHSPs may share a similar mechanism for their chaperone function.

CHAPTER V

SCRIPT ASSISTED MICROSCOPY (SAM) IMPROVES DATA ACQUISITION RATES ON FEI TECNAI ELECTRON MICROSCOPES EQUIPPED WITH GATAN CCD CAMERAS

5.1 Abstract

We have developed a set of scripts that semi-automates data collection on FEI Tecnai electron microscopes equipped with Gatan CCD cameras. These scripts were developed utilizing the scripting interface provided by both the microscope and camera manufacturers. Our script-assisted microscopy (SAM) package allows the user to select multiple locations at low-magnification in low dose search mode for automatic acquisition in batch, within exposure mode. The SAM package minimizes dial and mouse movements by the user, which improves efficiency and microscope ergonomics for more productive prolonged microscopy sessions. With SAM employed, an average of 1,000 micrographs per day can be collected on any grid type at very high magnification, where camera over-sampling improves the signal to noise ratios at high spatial frequency. This rate of data collection is a five-fold improvement over our traditional manual collection rates and is comparable to rates achieved by other labs using fully automated microscopy.

5.2 Introduction

Cryo-electron microscopy (cryo-EM) is a complementary technique to X-ray and NMR structure determination of biological macromolecules, because it is ideal for examining multi-protein or supramolecular complexes not easily solved by crystallography and NMR. Although cryo-EM is ideal for filling this resolution gap between cellular and atomic structures, cryo-EM of biological material requires extremely low electron dose to be used in imaging to avoid damaging the biological specimen. This, unfortunately, results in images containing especially low signal noise ratios, where it is estimated (Henderson, 1995) that hundreds of thousands of particle images are required to generate a near-atomic resolution structure. Manually collecting such large numbers of images demands significant investment of time by experimenters and is a tedious rate-limiting step toward high-resolution structure determination. Further, a high throughput, automated methods of data collection are highly desirable, since ice growth on the cryo-EM grid within the column, limits grid imaging to days only (Liu et al., 2006).

Automated electron microscopy originated with the computer control of transmission electron microsopes (TEM) and the emergence of slow-scan CCD cameras. The first automated microscopy software was developed for tomography applications, where a tilted series of images are collected for three dimensional volume reconstruction (Koster et al., 1992; Mastronarde, 2005; Zheng et al., 2007; Ziese et al., 2002). For single particle structure determination, several automated data collection packages are currently available. Leginon, developed by the National Resource for Automated Molecular Micrscopy (NRAMM), was first developed to work on the Phillips TEMs, now FEI, and is capable of simulating an experienced microscopist to complete all tasks of searching, targeting, exposing, and storing images in a database. This is done with limited human intervention (Suloway et al., 2005). AutoEM and AutoEMation (Lei & Frank, 2005; Liu et al., 2006; Zhang et al., 2001), also incorporate several levels of automation, allowing automatic or manual grid square and hole selection. These packages were designed for commercially available holey carbon grids, which possess uniform holes size and arrangement. Typically, these applications acquire data at exposure magnifications below 100,000X, a magnification range suitable for photographic film as recording media (Booth et al., 2004; Lei & Frank, 2005; Liu et al., 2006; Stagg et al., 2006). In our lab, micrographs are digitally recorded on a CCD camera at relative high magnifications (> 200,000X) in order to over-sample the specimen on the CCD chip. The limited field of view at this magnification requires precise targeting, to less than 0.05μm, in order to center sample on the CCD chip. This precision of targeting is not easily achieved with current automated software packages. In some instances, we preferentially use homemade holey carbon grids, because they better preserve our specimen and produce superior ice. These irregular arrays of holes are not amendable to automatically identifying and targeting with current automated microscopy packages. Due to these limitations, we have been unable to take advantage of the current automated software packages. Therefore, we have developed a set of scripts that could automate highly redundant processes and assist the microscopist rather that replace. This script assisted microscopy (SAM) package is implemented with the scripting interface provided by the manufacturers of both the FEI and Gatan instruments.

Specifically, one script helps the user to target positions by allowing a graphical interface with the search window in search mode, while then calculating and storing beam and image shifts from these user positioned graphical elements. A second script then applies the image and beam shifts to the microscope for acquiring multiple micrographs in batch at high magnification in low dose exposure mode. A final script then allows for rapid evaluation and archiving of the collected micrographs in parallel with acquisition. As a package, these scripts have increased our data collection at magnifications >200,000kx on any grid type at least five fold in comparison to our manual data collection and significantly improves microscope ergonomics. More importantly, they show how simple scripting, which is available to all microscopist, using the manufacture-derived scripting language can achieve significant improvement in throughput and ergonomics while using the microscope.

5.3 Methods

Specimen preparation:

CryoEM grids were prepared by applying ~3.0 μl. of (0.25–1 mg/ml) protein, to double side glow-discharged R2/4 Quantifoil grids (Quantifoil Micro Tools GmbH), C-flat grids (Protochips, Raleigh, NC), or homemade holey carbon grids. The grids were frozen in ethane slush using either a homemade vitrification device or a Vitrobot (FEI, Eindhoven, Netherlands). A thin support layer of amorphous carbon was deposited on C-flat grid before glow discharge and vitrification. The amorphous carbon film on a cryo grid and a Pt-Ir grid were used for resolution test with assigned image-shift values.

Script programming:

The SAM package utilizes both the scripting language of Gatan Digital Micrograph® software suite and the Tecnai scripting interface of the FEI Tecnai series of microscopes. Our specific installation is on a Windows 2000 professional operation system (service pack 4) with Tecnai User Interface (TUI) v2.1.8 and Digital Micrograph (DM v3.8.1). Tecnai microscopes allow users to communicate and control the microscope through a Windows standard *COM* interface, which supports the major object-oriented programming (OOP) languages. Microsoft Visual Basic 6.0 is used to draw the interface of the image acquisition application in the SAM package, in which Tecnai object and Tecnai CCD library are used to communicate with microscope and CCD cameras. Digital Micrograph (Gatan Inc., Pleasanton, CA) software suite provides a powerful scripting language, which allows user to customize Digital Micrograph and manipulate micrographs for specific applications. Two DM scripts were implemented and installed as custom components. The first one calculates and saves the beam/shift offsets based on user's annotations of CCD camera position and targeted positions on the display of search view. The second script groups a number of DM menu calls, which are responsible to micrograph binning, FFT calculation and saving, into one button.

Electron Microscopy:

We have tested the SAM package on both of our FEI Tecnai electron microscopes. The T12 is a 120kV, LaB6 microscope, which we operate at 120 kV and collect data at a nominal magnification of 67,000X. Our FEI Polara (TF-30) is a 300 kV FEG instrument, which we operate at 300 kV with a nominal magnification of 200,000X or 310,000X. The T12 is equipped with a Gatan UltraScan1000™ (2k x 2k CCD) and the TF-30 is outfitted with a Gatan Ultrascan4000™, a 4k x 4k CCD camera. The calibrated pixel sizes are 0.589Å and 0.375Å at 200,000X or 310,000X respectively.

Estimating signal to noise ratio

The electron doses of amorphous carbon images are approximate 50 electron/Å^2. CTF parameters are estimated with ctfit program in EMAN package. Signal noise ratio plot can be calculated and displayed in ctfit interface after the 1D-power spectrums of cryo-electron micrographs are accurately fit.

5.4 Results

Strategy

The general steps for recording a low-dose micrograph on a Tecnai series microscope, includes focusing on carbon near the areas of interest, centering interesting areas into the center of view, switching between low-dose and expose modes for taking an exposure, and finally evaluating the recorded micrograph for saving or discarding. Focusing is performed once per grid-square if the grid is sufficiently flat, however typically focusing is performed following each stage translocation. The switch between search and exposure modes requires 15s in the latest Tecnai user interface (v2.1.8) and typically good practice necessitates more than 40s wait for stage drift to settle following any compustage movement. Further, manually centering an area of interest into position for acquisition demands precision, good bookkeeping to avoid imaging over lapping region, and exposes the specimen to unwanted electron dose. These problems can be compounded when collecting data on irregularly spaced hole on homemade holey carbon grids.

The strategy implemented in SAM is to limit switching between modes and avoid centering the interested areas manually in search view. This is achieved by annotating areas of interest on the DM search view window for subsequent targeting of these selected areas for batch exposure. Targeting is accomplished by deflecting the electron beam with calculated beam/image shift offsets (Figure V-1). This strategy significantly reduces the amount of dose and time associated with mode-switches and manual stage movements. Additionally, batch mode acquisition of ~5μm square regions of a grid square simplifies bookkeeping and allows a more efficient use of ice. Additionally, we attempted to reduce the repetitive motions associated with manual data collection to improve the ergonomics of the microscope and reduce the tedium of the microscopy session. For instance, we find to evaluate and save a 4Kx4K micrograph in DM software, we perform > 20 mouse clicks to select pull-down menu items and extensive mouse movements on the display screen, which costs over a minute following micrograph acquisition. Our solution is to group all repetitive operations into a script so that users may complete the micrograph evaluation and storage with only two mouse clicks and little mouse movement. We find scripting these tasks considerably alleviates experimenter fatigue, which we call data elbow. The improved evaluation speed also enables the parallel execution of image acquisition and assessment. Thus, these scripts can improve performance and, hopefully, overall quality of micrographs.

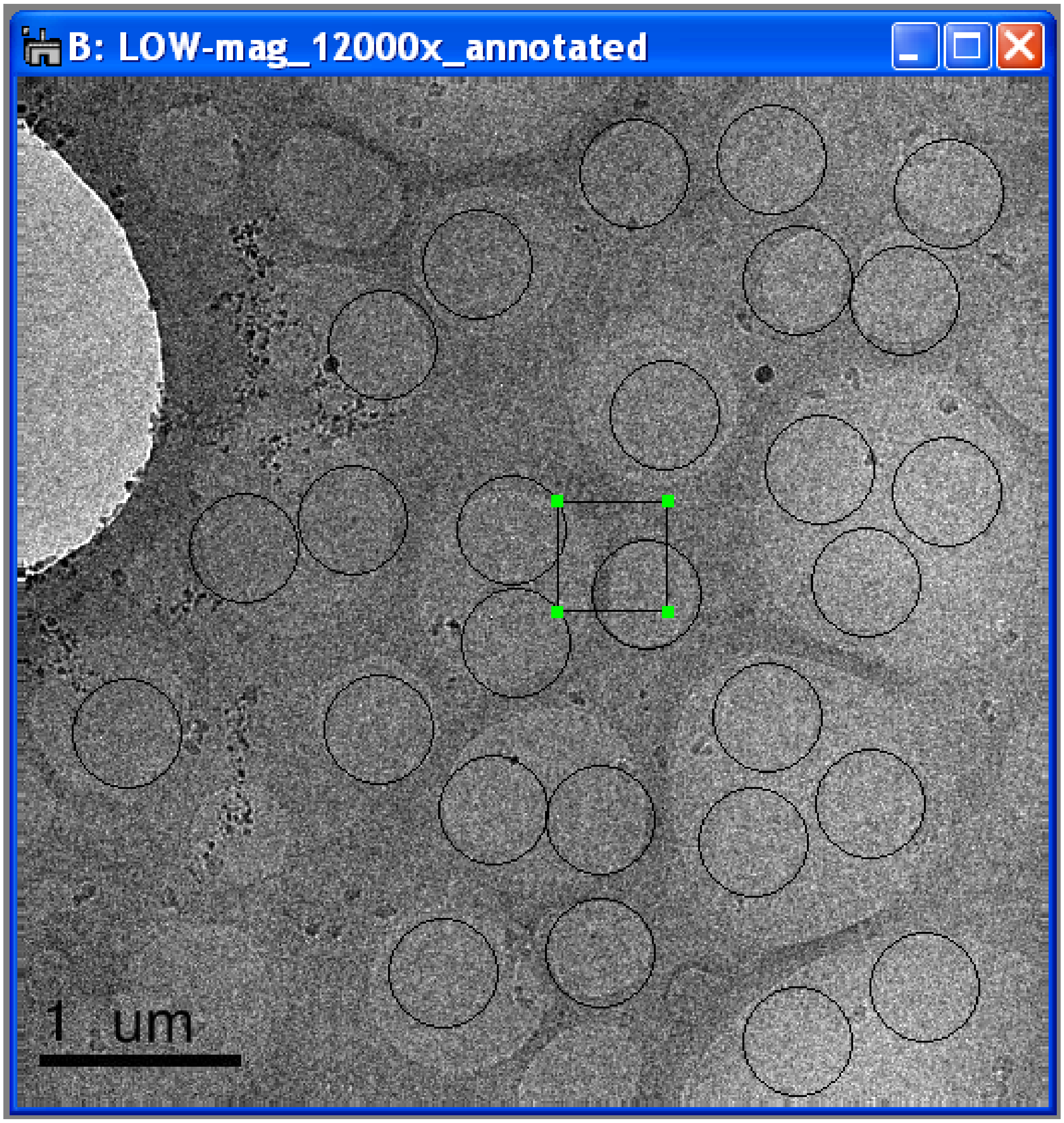

Figure V-1

In the low-magnification search-mode view window, circles are placed to annotate positions of interest for exposure mode acquisition. The square annotation indicates to the script the register of the CCD camera and the beam at (0,0) shift. The size of the annotations is the same as the beam spread in exposure mode for this instance.

Targeting

The most critical step in our image collection is precise targeting of the interested area for exposure at high magnification. On our TF-30, the search mode at 12,000X images an area of ~5um^2, where the 4K*4K CCD camera captures an area of only ~0.31um^2 at 200,000X and ~0.2um^2 at 310,000X. This necessitates a high level of precision for targeting particles and holes, and thus precludes the use of the goniometer, which is only accurate to a micron (Pulokas et al., 1999; Zhang et al., 2001). This is why most current automated EM software chooses to implement image shift to reposition the area of interest at the sub-micrometer scale (Mastronarde, 2005; Suloway et al., 2005).

A screen capture of our low dose search mode is shown in Figure V-1 with user annotations used to mark regions targeted for image acquisition. As a first step, it is essential to establish the position of the camera (box annotation in Figure V-1) for calculating the image shift for each of the selected regions (circles annotation in Figure V-1). A vector from the CCD camera position to the targeted position is used to represent the expected shift in Gatan CCD camera coordinates (see Figure V-2). However, the CCD camera coordinates are not equivalent to image shift coordinates. To transform the shift vector in CCD camera coordinates into image shift coordinates, two factors need to be considered. The first factor is the position of CCD camera in the search mode micrograph. It is possible to center the CCD camera to the center of the micrograph in low-dose search mode by independent image shift. Unfortunately, any small error of centering is magnified in exposure mode by an order of magnitude. So an initial alignment of the actual position of CCD camera is essential to reduce possible centering errors. Thus, the shift vector in camera coordinates is calculated between the single square annotation, which marks the position of the camera, and various circle annotations, which are regions of ice to be imaged. The second factor is the coordinate transformation. The relationship between camera coordinates and image shift coordinates is illustrated in Figure V-2.A. A general mathematic formula for transforming a vector $\vec{S}$ from camera coordinate xy to image shift coordinate x′y′ is shown in Figure V-2.B. Three constant parameters (Å/pixel, X_Scale_factor, Y_Scale_factor) are introduced in the formula because the retrieved position values (x, y) in camera coordinates are in pixel units and image shift coordinates are not in the same scale as the CCD camera coordinates. A DM script in the SAM package is responsible for transforming the vectors between two coordinates and stores the image shift value into a text file (see Figure V-3).

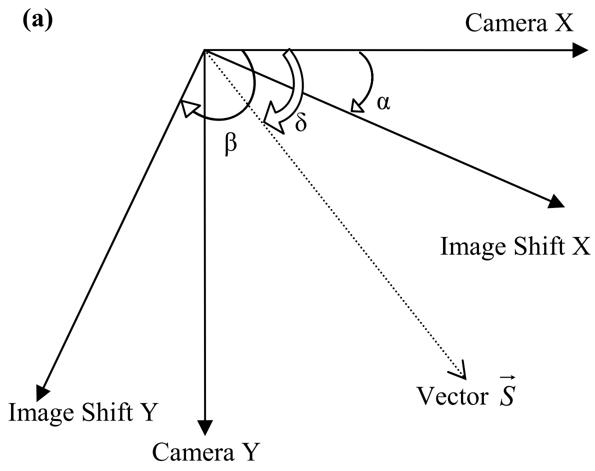

(b)

$$x' = \sqrt[2]{x^2 + y^2} \times \frac{\sin(\alpha - \delta)}{\sin(\alpha - \beta)} \times \frac{\overset{o}{\mathrm{A}} / pixel}{X\_Scale\_factor}$$

$$y' = \sqrt[2]{x^2 + y^2} \times \frac{\sin(\delta - \beta)}{\sin(\alpha - \beta)} \times \frac{\overset{o}{\mathrm{A}} / pixel}{Y\_Scale\_factor}$$

Figure V-2

(a) We assume the angle between camera-X and image-shift X is α, the angle between camera-X and image-shift Y is β. The vector $\vec{S}$ *represents the direction and distance from origin position to targeted position in search view and the angle between camera-X and vector* $\vec{S}$ *is δ. (b). The general formula transform vector* $\vec{S}$ *from CCD camera coordinates and image shift coordinates. The x, y are CCD camera coordinates value of vector* $\vec{S}$*, the x’, y’ are the value of vector* $\vec{S}$ *in image-shift coordinates.*

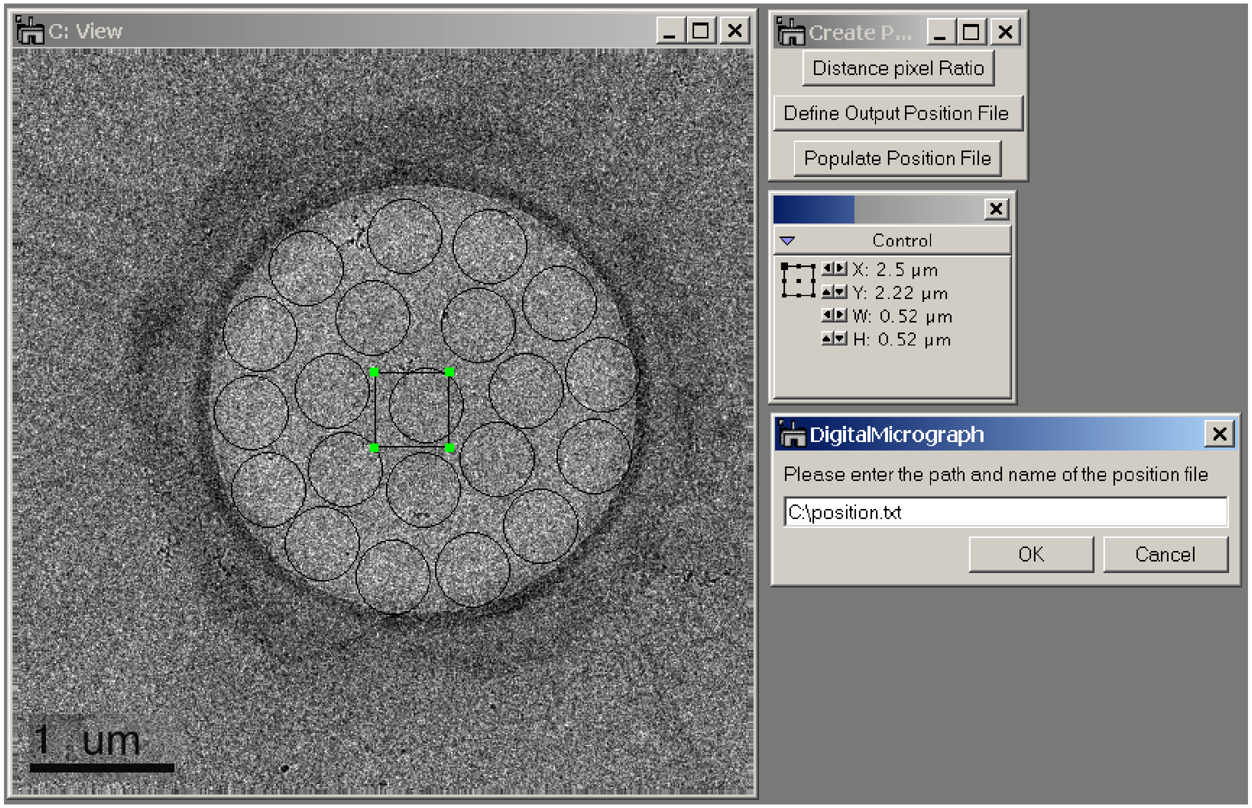

X: 2.5 µm
Y: 2.22 µm
W: 0.52 µm
H: 0.52 µm

Please enter the path and name of the position file

C:\position.txt

Figure V-3

The search mode image in the left window is a representative view of a 2µm ice hole on a 2/4 Quantifoil grid. The script createpostionfile, shown at top-right, transforms the camera coordinates into image shift coordinates. Just below the createpositionfile window is the control module in DM display, which indicates the position of the selected annotation in the view window at left. At right bottom, the user defines the path and name of the position file.

Image Acquisition

Images are acquired with a script that runs as a separate program, separate from the TUI and DM interfaces (see Figure V-4). It reads the saved beam/image shift parameter file and lists the image shift values for each of the targeted regions in the display box on the left. The user can start automatic data acquisition simply by clicking one button. We found it necessary to incorporate a delay time of several seconds in order to avoid the image drifting after adjusting deflection coil currents and to provide the user with time to assess the images prior to saving. The current image shift values are displayed in the two text boxes at the bottom of the window. This provides the user manual control of the image shift values for testing or calibration purposes.

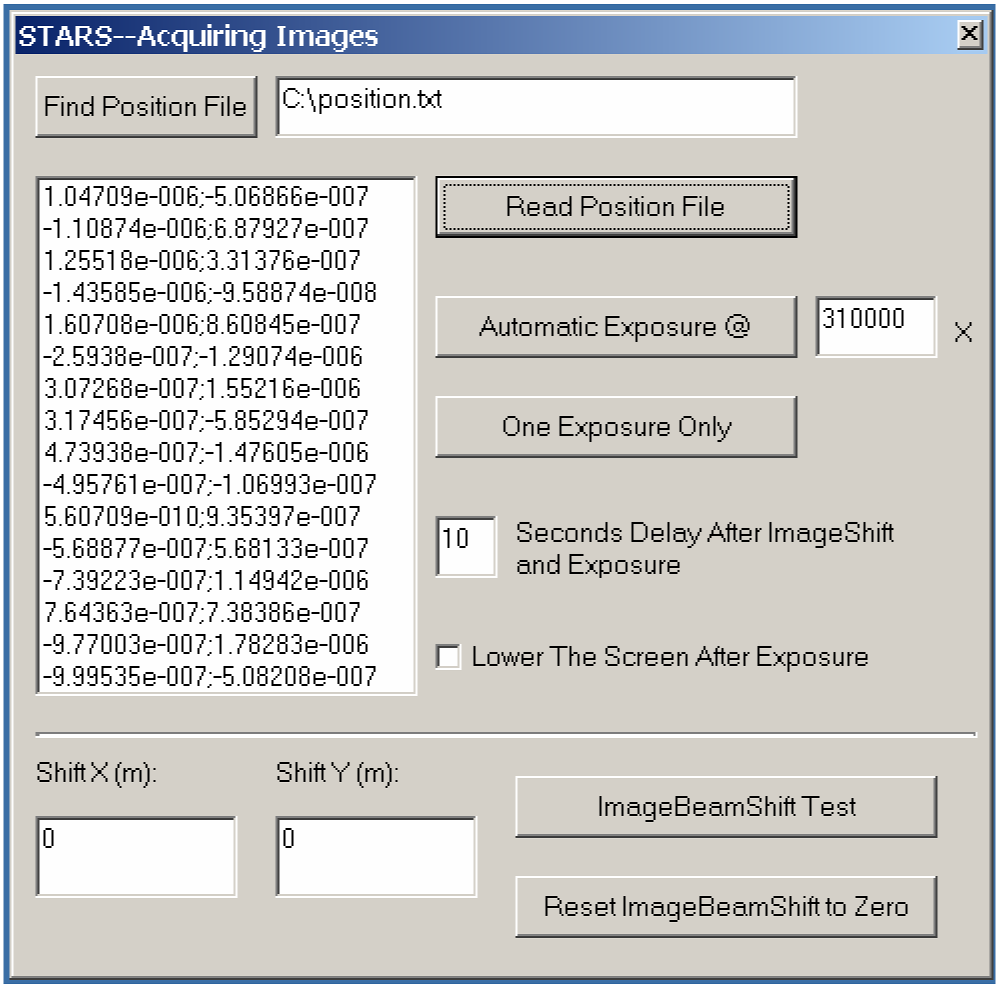

C:\position.txt

```
1.04709e-006;-5.06866e-007
-1.10874e-006;6.87927e-007
1.25518e-006;3.31376e-007
-1.43585e-006;-9.58874e-008
1.60708e-006;8.60845e-007
-2.5938e-007;-1.29074e-006
3.07268e-007;1.55216e-006
3.17456e-007;-5.85294e-007
4.73938e-007;-1.47605e-006
-4.95761e-007;-1.06993e-007
5.60709e-010;9.35397e-007
-5.68877e-007;5.68133e-007
-7.39223e-007;1.14942e-006
7.64363e-007;7.38386e-007
-9.77003e-007;1.78283e-006
-9.99535e-007;-5.08208e-007
```

310000 X

10 Seconds Delay After ImageShift and Exposure

☐ Lower The Screen After Exposure

Shift X (m): 0

Shift Y (m): 0

Figure V-4

The contents of the image shifts or "position" file are read into the acquisition application and displayed as a list on the left. The user may set the delay time and exposure magnification in the corresponding text boxes. Current image shift values are displayed in meters in the two textboxes labeled Shift X and Shift Y (bottom left of FigureV.4). The image shift values can also be entered in these two text boxes for calibration purposes.

Calibration

According to the formula in Figure V-2b, several parameters need to be determined before the script can accurately target selected positions in search mode on an FEI microscope. Angles α and β are the angles between image shift coordinates and CCD camera coordinates X and Y, respectively (Figure V-2a). Scale factors normalize the relationship between image shift coordinates and camera coordinates. These scale factors are determined by calibration of the image shift distance on an area of the carbon support film away from the imaging area within the SAM package. By setting specific image shift values and directions in the image acquiring script (Figure V-4.), the measured distance in the DM search view window can be calibrated to the image shift values. For instance, a prolonged exposure is used to mark the unshifted beam position on the grid in exposure mode by burning the ice away from the carbon surface. This burnt area, which is visible at low magnification in low dose mode, is annotated with a circle. The annotation and control tools in DM are used to measure the distance and direction between these marks in the image in the search mode view window; this also is a perfect time to set the beam spread at the desired C2 lens value. Linear regression of a series of image shift test points can readily achieve an accurate calibration of the angles α and β as well as their relationship to the X, Y scale factor. Since the Å/pixel ratio depends on the magnification used in search mode, it is necessary to calculate this once at the beginning of initiating the script (see Figure V-3). The X-value for the position of the unshifted beam is determined by reading the value of X for the annotated box marking the unshifted beam in the control window of DM. This value is entered into the popup window for the “Distance pixel ratio” of the DM script Createpositionfile (Figure V-3, top right hand box). The accurate calibration of these parameters under the user specific microscope conditions ensures the accurate targeting for high magnification exposure.

Evaluation and Saving

Due to the low contrast of biological specimens in electron micrographs, binning of the micrographs is required in order to achieve the contrast necessary to reveal particles for evaluation. In addition, a fast Fourier transformation (FFT) of the micrograph displays any astigmatism, drift, and/or charging that exists in the digital micrograph (this is evident by the misshapen or directionally missing Thon rings). The third script in the SAM package generates and displays a binned micrograph and an FFT image together with one click of a button. Following evaluation by the user, another button will close all opened micrograph windows either saving the micrograph unbinned with a sequential name specified in DM saving module (Figure V-5.) or with another button to discard the images. Simultaneous with saving of the digital micrograph the script also writes the statistic information of the saved micrograph in the results file as well as the timestamp and filename, in order to generate a record of the relative ice thickness and dosage of each micrograph saved.

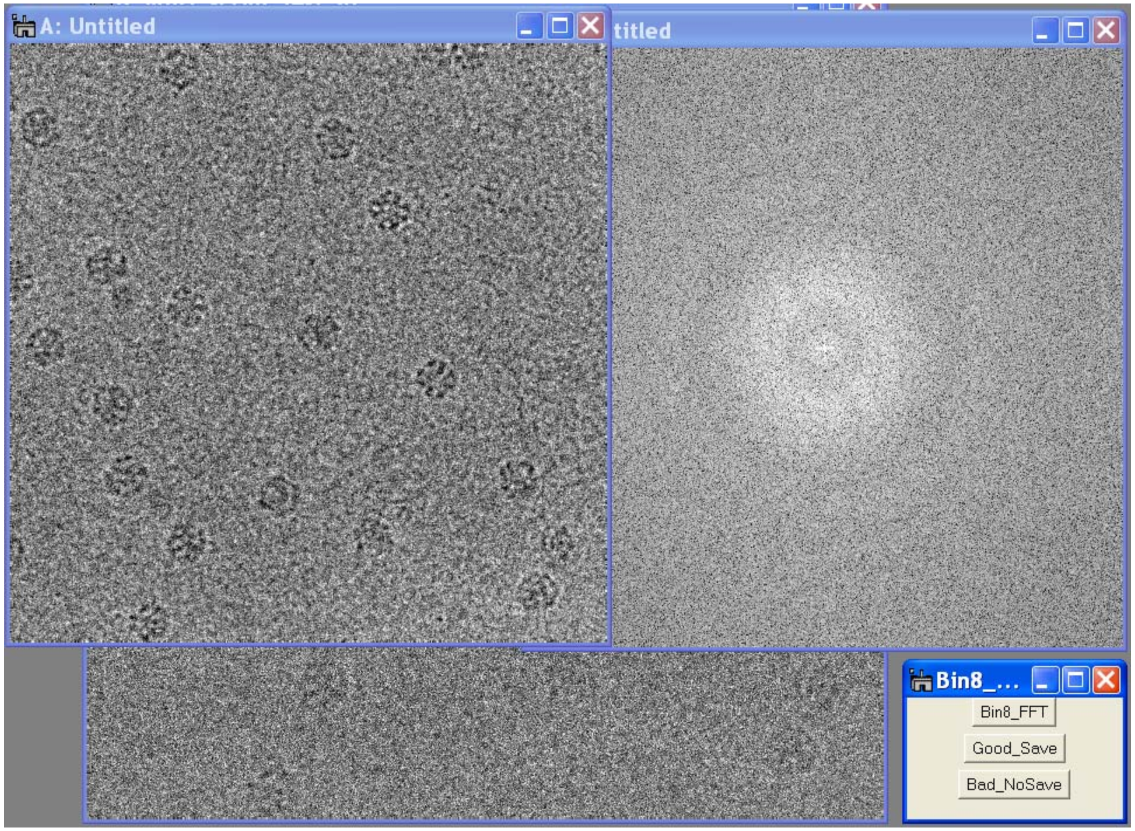

Figure V-5

The "Bin8_FFT_Save" module is shown at the bottom-right corner. By clicking on the "Bin8_FFT" button the original micrograph is binned by a factor of 8 (top left image) and is on top of the unbinned image for comparison for particle definition. Simultaneously an FFT is calculated(right top image). Following evaluation, the user may choose to save the image by clicking on the "Good Save" or discard the image by clicking on the "Bad Nosave" button .

Resolution Test

To test the effect beam/image shift has on resolution; we collected a series of images taken with beam/image shifts that varied in distance from the origin. The 100μm objective aperture of our TF-30 obstructs the field of view when a ±10μm beam/image shift is applied to the beam, while a smaller objective aperture would be expected to obstruct at an even smaller shift offset (Mastronarde, 2005). At 4μm shift, we found no decrease in the signal noise ratio (SNR) of images collected on a Pt-Ir holey carbon surface compared the unshifted image control (Fig5.6A). But in actual application, we rarely exceed 2 μm shifts. In order to test our shifting conditions under these conditions, we imaged amorphous carbon film at zero-shift and when the beam/image shift was set to + 2μms at magnifications of 200,000X and 310,000X. This data is plotted as the signal noise ratio (SNR) of each micrograph in Figure V-6B. We observed there is little affect on SNR by a +2 μm beam/image shift at both magnifications. Further, the plots also show that the 310,000X magnification yields a higher SNR than at 200,000X for the highest resolutions. We ascribe this to the smaller pixel size, which gives a higher Nyquist frequency limit. This result is consistent with the previous report portraying the performance characteristics of 4K*4K CCD cameras. (Booth et al., 2006; Booth et al., 2004; Liu et al., 2006; Sander et al., 2005)

(a)

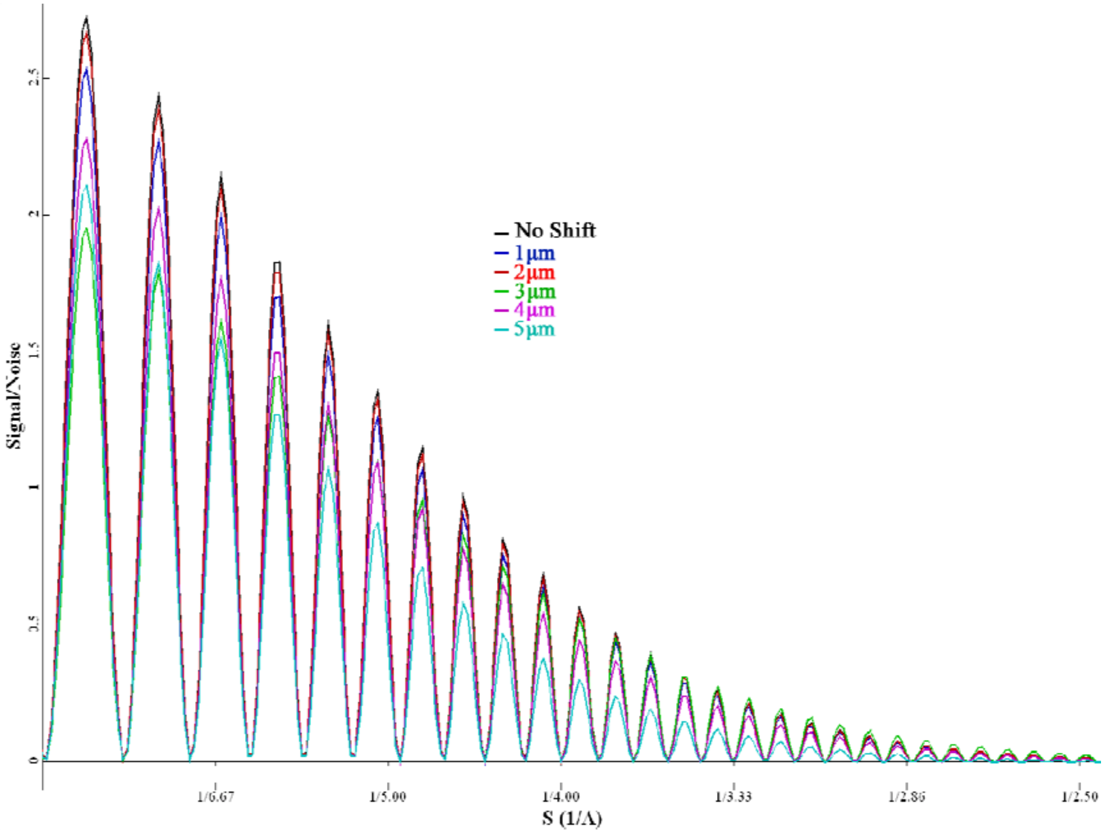

Figure V-6--continued

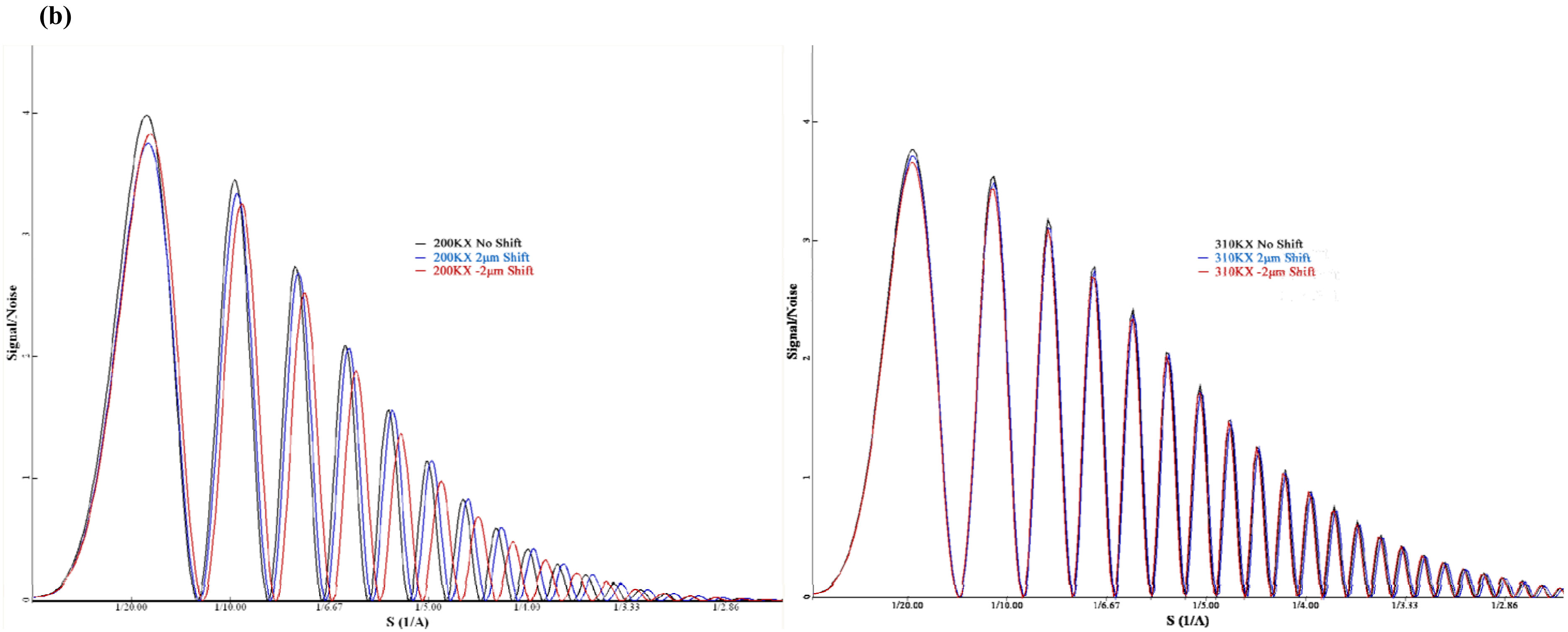

Figure V-6

(a) *Pt-Ir micrographs with a series of image shifts were recorded at 1µm defocus.* **(b)***Amorphous carbon film micrographs are recorded with no shift applies or ±2µm image shift at magnification of 200,000X (0.71µm defocus) and 310,000X (0.86µm defocus). The SNRs were plotted using ctfit in the EMAN package for quality assessment. No loss of signal is evident in the shifted conditions compared to the un-shifted.*

Efficiency

The SAM package currently operates on both our Tecnai TF30 polara and T12, which are equipped with Gatan Ultrascan 4000 and 1000 cameras, respectively. We have been able to obtain 1000 high-quality micrographs in 24 hours on the TF30 polara using SAM, whereas less than 200-300 micrographs were considered a good day with manual collection. Similarly, on the T12, SAM has allowed us to acquire ~100 micrographs per hour from regular C-Flat™ grids. This compares favorably to our usual 20 micrographs per hour without implementing SAM. Moreover, this efficiency is comparable to that of currently available automatic data collection software. It is important to note that by decreasing our delay time between image shifts, we are able to collect data at a rate that exceeds the stability of the computer-controlled microscope, suggesting we have achieved the maximal rate of data throughput for this generation of Tecnai microscopes. One of the greatest advantages of the SAM package is the maximization of image collection when using the Gatan 626 holders on our T12. The cryo-EM microscopy session is usually dominated by waiting for the cryo-holder to settle from drifting caused by temperature fluctuation upon insertion or dewar fill, which allows only a few hours at a time to collect micrographs. This time is maximized by SAMs improved throughput.

5.5 Discussion

The advantages of the slow-scan CCD camera over photographic film are its wide dynamic range, linearity, and instantaneous readout. Several studies suggest that the CCD camera gives comparable if not better signal to noise ratio than film up to 1/2 Nyquist frequency. (Booth et al., 2006; Booth et al., 2004; Liu et al., 2006; Sander et al., 2005) The major limiting factor of recording high-resolution information by CCD camera is its modulation transfer function (MTF), which is the Fourier transform of the point spread function for the electron scintillator coupled to the CCD (Downing & Hendrickson, 1999; Faruqi & Subramaniam, 2000). The fall-off of the CCD camera's MTF falls below 0.2 - 0.1 at the Nyquist frequency, which is a quarter of that for film (Sherman et al., 1996). One way to boost the MTF at high spatial frequencies if to capture CCD images at higher magnification, and then combine the low signal information of each pixel by binning (Booth et al., 2006; Sander et al., 2005; Sherman et al., 1996). Our lab has applied such a strategy for high-resolution cryo-EM structure study and achieved a 10 Å reconstruction of octahedral small heat shock protein oligomer, a 7Å resolution reconstruction of icosahedral adenovirus and a sub-nanometer reconstruction of the asymmetrical DNA-PKcs (Saban et al., 2006; Shi et al., 2006; Williams et al., 2007). Of course the great disadvantage associated with this approach is the incredibly small field of view compared to photographic film, thus necessitating a greater number of micrographs to be collected at extremely high targeting accuracy (Booth et al., 2004; Sander et al., 2005).

Thus, a high-throughput data collection method, which can precisely target areas of interest, becomes crucial to achieve sub-nanometer single particle reconstructions using a CCD camera.

Our SAM package improves the data collection throughput 5 fold over manual data collection without sacrificing, targeting accuracy or data quality. Faster data collection also means that we can pull more data from a good cryo-EM grid before in column ice growth destroys our imaging contrast (Liu et al., 2006). By leaving several processes, like the instrument alignment, focusing, good-area identification, compustage movement and micrograph evaluation, to the experienced microscopist; we have ensured the micrscopy session is maintained at optimal conditions. We believe this ultimately saves time, given that the largest investment of time is spent in image processing and structural refinement. With the improved microscope ergonomics the SAM package provides, a significant reduction in user tedium promotes a greater attention to quality control. In our experience over 30% of collected micrographs are rejected due to images containing ice contamination, inappropriate particle dispersion, charging/drift, etc. We have found the improved ergonomics greatly reduces the number of unsatisfactory micrographs in our final datasets, which consumes network transfer time, disk space and image processing time. The drawback of a semi-automatic data collection method is data-collection remains labor-intensive, but the advantages are the resulting data is of superior quality.

The current SAM package only consists of less than 500 lines of code. In the future, we plan to incorporate a stage position log that interacts with the new Tecnai stage2 atlas feature, so that the grid positions are automatically stored through the low dose session. In addition, square montages can be used to move from grid square to grid square in the search view by a single click instead of using the control pad dial. Hole annotation auto-placement is also desired the more regular C-flat or Quantifoil grids, and this can be easily achieve by storing templates of idealized search mode view windows with their annotaions. These additional script assisted activities would further reduce repetitive motion, and streamline session documentation making long data collection sessions less demanding. It also illustrates the flexibility of the modularized scripting approach to microscopy.

CHAPTER VI

SUMMARY AND CONCLUSIONS

6.1 Review of the function and therapeutic potential of sHSPs

The cell possesses elaborate and effective mechanisms to protect against chronic or acute disturbances of homeostasis, in which various molecular chaperones play key roles by promoting and maintaining correct protein folding. The sHSPs, as one of the canonical families of molecular chaperones, bind unfolded proteins and form soluble oligomers with substrates, thereby preventing irreversible aggregation caused by external stressors or genetic abnormalities. This property is best manifested by human α-crystallin in the lens, which prevents aggregation of unfolded lenticular crystallins and delays lens opacification. Over-expression of sHSPs protects cells against the deleterious effects induced by heat, oxidative stress, and exposure to cytotoxic drugs and apoptotic inducers. The sHSPs reduce and/or delay apoptosis by interacting with a variety of key components of the apoptotic pathways, including the cytoskeleton, cytochrome c, pro-caspase-3, p53 and proteasome components. In organisms, the transcriptions of sHSPs genes are spatio-temporally regulated for normal embryonic development, including normal lens development. The sHSPs are known to modulate cell growth, differentiation, intracellular redox state, and tumorigenicity. A decrease in proliferation and an increase in cell death are observed for lens cells derived from the αA-crystallin knockout mouse. However, more work is needed to better understand whether the classical chaperone function of sHSPs can provide a mechanistic basis for all their cellular activities in vivo. It is conceivable that, in addition to their chaperone function, other functions associated to sHSPs may be required (Andley, 2007; Arrigo, 2007; Arrigo et al., 2007; Bloemendal et al., 2004; Ellis, 2007; Haslbeck et al., 2005; Latchman, 2005; Sun & MacRae, 2005b).

The universal distribution and variety of functions related to sHSPs create a high probability that sHSPs may be involved in the initiation and progression of diseases. Abnormal sHSPs due to hereditary mutation or progressive modifications may become pathogenetic. This effect is evidenced by congenital cataract and DRM (desmin related myopathy), in which single site mutations disrupt the structure and the activity of human sHSPs; and age-related cataract, in which the progressive unfolding of proteins titrates all of the available cellular chaperone capacity and results in irreversible formation of protein deposits, leading to cell pathology or even cell death (Bloemendal et al., 2004; Goldfarb et al., 2004). A recent finding suggests that heart cells with DRM related to R120G αB-crystallin might be damaged through perturbation of the cellular redox state (Rajasekaran et al., 2007).

On the other hand, the therapeutic potential of sHSPs, utilizing their chaperone function, has been explored with great effort. The pathogenic effects due to deficient sHSPs might be treated by introducing normal, functional sHSPs. Clinical methods include gene delivery with viral vector, administration of exogenous chaperones and induction of endogenous chaperone genes. An good example is that disease progression in the ALS (amyotrophic lateral sclerosis) model mouse is significantly delayed through the treatment with arimoclomol, a activator of the heat shock response (Kieran et al., 2004). The expression of Hsp27 may be used as a biomarker for assessing the aggressiveness of some cancers and predicting the prognosis of cancer chemotherapy (Ciocca & Vargas-Roig, 2002). A better understanding of the mechanisms underlying the structural and functional regulation of human sHSPs would pave the road to the discovery and design of new therapeutic strategies for human diseases through modulating specific activities of human sHSPs (Andley, 2007; Arrigo et al., 2007; Latchman, 2005; Sun & MacRae, 2005a; Tabner et al., 2005).

6.2 Mechanism of sHSPs function revealed by cryoEM

CryoEM is gaining increasing importance in structural biology, especially for studies of large macromolecular assemblies, which are not accessible for X-ray crystallography and NMR. The resolutions achieved for cryoEM 3D reconstructions by the single particle approach have been improving steadily. Numerous structures have been determined in the sub-nanometer (<10Å) range (Frank et al., 2007; Saban et al., 2006; Williams et al., 2007). Henderson estimated that it would require a million asymmetric units to achieve 3Å resolution (Henderson, 1995). The high-end microscopes, which are equipped with coherent field emission guns and stable lens, are able to deliver 2D images containing structural information out to atomic resolution (1-3Å). Automation package, like Leginon (Suloway et al., 2005) and our scripts package, allow computer-controlled EM sessions and greatly improve the speed of data collection. Ultimately, the achievable resolution may be limited by heterogeneity of the specimen, which may be biochemical or conformational. Biochemical heterogeneity refers to compositional variations among the macromolecules in a specimen, including post-translational modifications, subunit composition, and ligand occupancy, as in the case of polydisperse human α-crystallin (Haley et al., 2000; Stewart et al., 1999). Conformational heterogeneity results from structural variability of the specimen molecules, and may include mixture of conformers or disordered regions due to structural flexibility. Multiple statistical approaches to address the issue of heterogeneity are being actively developed, as reviewed in (Leschziner & Nogales, 2007). Essential biological information can be gained from cryoEM reconstructions, even at moderate resolution. Additional constraints from other biophysical techniques, such as EPR, CD, fluorescence, and small angle X-ray scattering, as well as *in silica* modeling and density fitting with atomic resolution structures of domains or component molecules facilitates the interpretation of cryoEM structures. (Leschziner & Nogales, 2007; Mitra & Frank, 2006)

We have constructed a set of Hsp16.5 variants by mutagenesis, which display diverse quaternary structures and diverse chaperone activities. We used cryoEM and single particle 3D reconstruction to study the structures of these variants and their complexes with substrates. Combined with information from SDSL-EPR, fluorescence binding assay, light scattering and electron density fitting and modeling, we gained great insight into the structural features and the mechanism of sHSPs' chaperone function.

The oligomeric structures of Hsp16.5-P1 and Hsp16.5-TR were determined to resolutions of 10Å and 12Å respectively by cryo-EM reconstruction. Cryo-EM class-sum images were also generated for the polydisperse Hsp16.5-P1N variant. The Hsp16.5-P1 cryo-EM density map was interpreted by docking the X-ray crystal structure of the α-crystallin domain from Hsp16.5-WT as guided by the residue specific information from EPR experiments. Consequently, a pseudo-atomic model with 48 copies of the α-crystallin domain was built for the Hsp16.5-P1 oligomer. The cryoEM and SDSL-EPR analysis of Hsp16.5-P1 and Hsp16.5-P1N reveals the structural basis of oligomer plasticity within small heat-shock proteins. The binding characteristics of the Hsp16.5 variants for model substrate proteins, T4 lysozyme (T4L) mutants, were studied by a fluorescence assay. Our results indicate that polydispersity is associated with enhancement of binding ability.

We also studied the structure of complexes formed by the Hsp16.5 variants and model substrates by cryoEM. Our results show that homogenous Hsp16.5-WT assemblies are transformed into a continuum of oligomeric states upon T4L substrate binding. The structure of the Hsp16.5TR/T4L complex confirms that its oligomeric shell, which is formed by 24 copies of the α-crystallin domain, is able to bind substrate with low-affinity. We find differences between the unbound structures and the substrate bound structures that lead us to conclude that binding of T4L to Hsp16.5-P1 and Hsp16.5-WT induces a conformational change in the N-terminal region. Our data suggests that both the α-crystallin domain and N-terminal region serve to stabilize the substrate inside of the sHSP oligomer and that the dynamic oligomeric state of sHSPs contributes to its substrate binding ability.

Cellular protein structures are maintained by the sum of many weak forces, i.e. hydrophobic interactions, hydrogen bonds and van der Waals interactions. Folded proteins are marginally stable and exist in a thermodynamic equilibrium with unfolded states, which expose hydrophobic patches to solvent. Hydrophobic interactions between sHSPs and substrates underlie the chaperone activity of sHSPs, resulting in rather promiscuous actions like other chaperones, i.e. GroEL and Hsp70. However, the sHSP members of a single species have divergent sequences outside of the conserved α-crystallin domain, different temporal and spatial expression patterns, and a variety of oligomeric states, indicating possible substrate selectivity in specific cell types. The coupling of protein unfolding and the interaction between sHSPs and unfolded proteins help to maintain a delicate homeostasis of cellular proteins (Mchaourab et al., 2007). Environmental stresses and protein mutations could disrupt this fine balance and lead to a disease state.

For instance, we observe that the structure of the N-terminal region in Hsp16.5-R107G without substrate mimics the substrate bound state of the N-termini in WT+T4L and P1+T4L. We speculate that this mutation induces a conformational change and activation that would normally result from heat-shock treatment and substrate binding.

This would provide a mechanistic insight into the cataractogenesis related to an Arg mutation in human α-crystallin at the analogous site. The conformational changes induced by this Arg mutation may transform human α-crystallin into a hyperactive state, which has enhanced binding affinity to unfolded protein. Therefore, the protein equilibrium is shifted toward unfolding and stable α-crystallin-substrate complexes are formed. This causes the chaperone capacity of α-crystallin to be titrated out (Koteiche & Mchaourab, 2006). Finally, excess unfolded protein may interact with multiple α-crystallin-substrate complexes and start the nucleation of large aggregates, which will cause light scattering and result in a turbid lens.

In conclusion, this thesis has described structural studies of a sHSP from a hyperthermophile (Hsp16.5), engineered mutant variants of Hsp16.5, and substrate complexes by cryoEM and single particle reconstruction. Our result show that sequence divergence in the N-terminal region leads to the wide spectrum of quaternary structures in the sHSP family and that the dynamic and polydisperse nature of sHSPs is important for chaperone function. These studies would have been difficult or impossible to perform on the naturally heterogeneous mammalian sHSPs. Nevertheless the knowledge learned from these studies should be applicable to mammalian members of the sHSP family. Future directions will be to extrapolate our perception to human sHSPs and develop a more complete understanding of their structural regulation and functional mechanisms.

REFERENCES

ADRIAN, M., DUBOCHET, J., LEPAULT, J. & MCDOWALL, A. W. (1984). Cryo-electron microscopy of viruses. Nature, 308(5954), 32-36.

ANDLEY, U. P. (2006). Crystallins and hereditary cataracts: molecular mechanisms and potential for therapy. Expert Rev Mol Med, 8(25), 1-19.

ANDLEY, U. P. (2007). Crystallins in the eye: Function and pathology. Prog Retin Eye Res, 26(1), 78-98.

ANFINSEN, C. B. (1973). Principles that govern the folding of protein chains. Science, 181(96), 223-230.

ARRIGO, A. P. (2007). The cellular "networking" of mammalian Hsp27 and its functions in the control of protein folding, redox state and apoptosis. Adv Exp Med Biol, 594, 14-26.

ARRIGO, A. P., PAUL, C., DUCASSE, C., MANERO, F., KRETZ-REMY, C., VIROT, S., JAVOUHEY, E., MOUNIER, N. & DIAZ-LATOUD, C. (2002). Small stress proteins: novel negative modulators of apoptosis induced independently of reactive oxygen species. Prog Mol Subcell Biol, 28, 185-204.

ARRIGO, A. P., SIMON, S., GIBERT, B., KRETZ-REMY, C., NIVON, M., CZEKALLA, A., GUILLET, D., MOULIN, M., DIAZ-LATOUD, C. & VICART, P. (2007). Hsp27 (HspB1) and alphaB-crystallin (HspB5) as therapeutic targets. FEBS Lett, 581(19), 3665-3674.

AUGUSTEYN, R. C. (2004). Dissociation is not required for alpha-crystallin's chaperone function. Exp Eye Res, 79(6), 781-784.

BATSON, P. E., DELLBY, N. & KRIVANEK, O. L. (2002). Sub-angstrom resolution using aberration corrected electron optics. Nature, 418(6898), 617-620.

BAUMEISTER, W. (2005). From proteomic inventory to architecture. FEBS Lett, 579(4), 933-937.

BAUMEISTER, W., GRIMM, R. & WALZ, J. (1999). Electron tomography of molecules and cells. Trends Cell Biol, 9(2), 81-85.

BAXTER, W. T., LEITH, A. & FRANK, J. (2007). SPIRE: the SPIDER reconstruction engine. J Struct Biol, 157(1), 56-63.

BERENGIAN, A. R., PARFENOVA, M. & MCHAOURAB, H. S. (1999). Site-directed spin labeling study of subunit interactions in the alpha-crystallin domain of small heat-shock proteins. Comparison of the oligomer symmetry in alphaA-crystallin, HSP 27, and HSP 16.3. J Biol Chem, 274(10), 6305-6314.

BLOEMENDAL, H., DE JONG, W., JAENICKE, R., LUBSEN, N. H., SLINGSBY, C. & TARDIEU, A. (2004). Ageing and vision: structure, stability and function of lens crystallins. Prog Biophys Mol Biol, 86(3), 407-485.

BOOTH, C. R., JAKANA, J. & CHIU, W. (2006). Assessing the capabilities of a 4kx4k CCD camera for electron cryo-microscopy at 300kV. J Struct Biol, 156(3), 556-563.

BOOTH, C. R., JIANG, W., BAKER, M. L., ZHOU, Z. H., LUDTKE, S. J. & CHIU, W. (2004). A 9 angstroms single particle reconstruction from CCD captured images on a 200 kV electron cryomicroscope. J Struct Biol, 147(2), 116-127.

BOVA, M. P., DING, L. L., HORWITZ, J. & FUNG, B. K. (1997). Subunit exchange of alphaA-crystallin. J Biol Chem, 272(47), 29511-29517.

BOVA, M. P., HUANG, Q., DING, L. & HORWITZ, J. (2002). Subunit exchange, conformational stability, and chaperone-like function of the small heat shock protein 16.5 from Methanococcus jannaschii. J Biol Chem, 277(41), 38468-38475.

BOVA, M. P., MCHAOURAB, H. S., HAN, Y. & FUNG, B. K. (2000). Subunit exchange of small heat shock proteins. Analysis of oligomer formation of αA-crystallin and Hsp27 by fluorescence resonance energy transfer and site-directed truncations. J. Biol. Chem., 275(2), 1035-1042.

BOVA, M. P., YARON, O., HUANG, Q., DING, L., HALEY, D. A., STEWART, P. L. & HORWITZ, J. (1999). Mutation R120G in alphaB-crystallin, which is linked to a desmin-related myopathy, results in an irregular structure and defective chaperone-like function. Proc Natl Acad Sci U S A, 96(11), 6137-6142.

BOYLE, D. L., TAKEMOTO, L., BRADY, J. P. & WAWROUSEK, E. F. (2003). Morphological characterization of the Alpha A- and Alpha B-crystallin double knockout mouse lens. BMC Ophthalmol, 3, 3.

BRADY, J. P., GARLAND, D., DUGLAS-TABOR, Y., ROBISON, W. G., JR., GROOME, A. & WAWROUSEK, E. F. (1997). Targeted disruption of the mouse alpha A-crystallin gene induces cataract and cytoplasmic inclusion bodies containing the small heat shock protein alpha B-crystallin. Proc Natl Acad Sci U S A, 94(3), 884-889.

BRADY, J. P., GARLAND, D. L., GREEN, D. E., TAMM, E. R., GIBLIN, F. J. & WAWROUSEK, E. F. (2001). AlphaB-crystallin in lens development and muscle integrity: a gene knockout approach. Invest Ophthalmol Vis Sci, 42(12), 2924-2934.

BRUEY, J. M., DUCASSE, C., BONNIAUD, P., RAVAGNAN, L., SUSIN, S. A., DIAZ-LATOUD, C., GURBUXANI, S., ARRIGO, A. P., KROEMER, G., SOLARY, E. & GARRIDO, C. (2000). Hsp27 negatively regulates cell death by interacting with cytochrome c. Nat Cell Biol, 2(9), 645-652.

BRUGGELLER, P. & MAYER, E. (1980). Complete vitrification in pure liquid water and dilute aqueous solutions. Nature, 288(5791), 569-571.

BUCCIANTINI, M., GIANNONI, E., CHITI, F., BARONI, F., FORMIGLI, L., ZURDO, J., TADDEI, N., RAMPONI, G., DOBSON, C. M. & STEFANI, M. (2002). Inherent toxicity of aggregates implies a common mechanism for protein misfolding diseases. Nature, 416(6880), 507-511.

BUKAU, B., WEISSMAN, J. & HORWICH, A. (2006). Molecular chaperones and protein quality control. Cell, 125(3), 443-451.

BUTT, E., IMMLER, D., MEYER, H. E., KOTLYAROV, A., LAASS, K. & GAESTEL, M. (2001). Heat shock protein 27 is a substrate of cGMP-dependent protein kinase in intact human platelets: phosphorylation-induced actin polymerization caused by HSP27 mutants. J Biol Chem, 276(10), 7108-7113.

CAPLAN, A. J., MANDAL, A. K. & THEODORAKI, M. A. (2007). Molecular chaperones and protein kinase quality control. Trends Cell Biol, 17(2), 87-92.

CARVER, J. A. (1999). Probing the structure and interactions of crystallin proteins by NMR spectroscopy. Prog Retin Eye Res, 18(4), 431-462.

CHACON, P. & WRIGGERS, W. (2002). Multi-resolution contour-based fitting of macromolecular structures. J. Mol. Biol., 317(3), 375-384.

CHIU, W., CHEN, D. H., JIANG, W., LUDTKE, S. J. & BAKER, M. (2006). Visualization of Biological Nano-Machines at Subnanometer Resolutions. JOEL News, 41(1), 12-17.

CIOCCA, D. R. & VARGAS-ROIG, L. M. (2002). Hsp27 as a prognostic and predictive factor in cancer. Prog Mol Subcell Biol, 28, 205-218.

COBB, B. A. & PETRASH, J. M. (2000). Structural and functional changes in the alpha A-crystallin R116C mutant in hereditary cataracts. Biochemistry, 39(51), 15791-15798.

CROWTHER, R. A., AMOS, L. A., FINCH, J. T., DE ROSIER, D. J. & KLUG, A. (1970). Three dimensional reconstructions of spherical viruses by fourier synthesis from electron micrographs. Nature, 226(5244), 421-425.

DAS, K. P., CHOO-SMITH, L. P., PETRASH, J. M. & SUREWICZ, W. K. (1999). Insight into the secondary structure of non-native proteins bound to a molecular chaperone alpha-crystallin. An isotope-edited infrared spectroscopic study. J Biol Chem, 274(47), 33209-33212.

DAS, K. P., PETRASH, J. M. & SUREWICZ, W. K. (1996). Conformational properties of substrate proteins bound to a molecular chaperone alpha-crystallin. J Biol Chem, 271(18), 10449-10452.

DE CARLO, S., EL-BEZ, C., ALVAREZ-RUA, C., BORGE, J. & DUBOCHET, J. (2002). Cryo-negative staining reduces electron-beam sensitivity of vitrified biological particles. J Struct Biol, 138(3), 216-226.

DE JONG, W. W., CASPERS, G. J. & LEUNISSEN, J. A. (1998). Genealogy of the α-crystallin--small heat-shock protein superfamily. Int. J. Biol. Macromol., 22(3-4), 151-162.

DE ROSIER, D. J. & KLUG, A. (1968). Reconstruction of Three Dimensional Structures from Electron Micrographs. Nature, 217(5124), 130-134.

DEN ENGELSMAN, J., GERRITS, D., DE JONG, W. W., ROBBINS, J., KATO, K. & BOELENS, W. C. (2005). Nuclear import of {alpha}B-crystallin is phosphorylation-dependent and hampered by hyperphosphorylation of the myopathy-related mutant R120G. J Biol Chem, 280(44), 37139-37148.

DOWNING, K. H. & HENDRICKSON, F. M. (1999). Performance of a 2k CCD camera designed for electron crystallography at 400 kV. Ultramicroscopy, 75(4), 215-233.

DUBOCHET, J., ADRIAN, M., CHANG, J. J., HOMO, J. C., LEPAULT, J., MCDOWALL, A. W. & SCHULTZ, P. (1988). Cryo-electron microscopy of vitrified specimens. Q Rev Biophys, 21(2), 129-228.

EATON, P., FULLER, W., BELL, J. R. & SHATTOCK, M. J. (2001). AlphaB crystallin translocation and phosphorylation: signal transduction pathways and preconditioning in the isolated rat heart. Journal of Molecular & Cellular Cardiology., 33(9), 1659-1671.

EHRNSPERGER, M., GRABER, S., GAESTEL, M. & BUCHNER, J. (1997). Binding of non-native protein to Hsp25 during heat shock creates a reservoir of folding intermediates for reactivation. Embo J, 16(2), 221-229.

EL-BEZ, C., ADRIAN, M., DUBOCHET, J. & COVER, T. L. (2005). High resolution structural analysis of Helicobacter pylori VacA toxin oligomers by cryo-negative staining electron microscopy. J Struct Biol, 151(3), 215-228.

ELAD, N., FARR, G. W., CLARE, D. K., ORLOVA, E. V., HORWICH, A. L. & SAIBIL, H. R. (2007). Topologies of a substrate protein bound to the chaperonin GroEL. Mol Cell, 26(3), 415-426.

ELLIS, J. (1987). Proteins as molecular chaperones. Nature, 328(6129), 378-379.

ELLIS, R. J. (2007). Protein misassembly: macromolecular crowding and molecular chaperones. Adv Exp Med Biol, 594, 1-13.

ELLIS, R. J. & MINTON, A. P. (2003). Cell biology: join the crowd. Nature, 425(6953), 27-28.

ENDRES, N. F., YOSHIOKA, C., MILLIGAN, R. A. & VALE, R. D. (2006). A lever-arm rotation drives motility of the minus-end-directed kinesin Ncd. Nature, 439(7078), 875-878.

FARNSWORTH, P. N., GROTH-VASSELLI, B., GREENFIELD, N. J. & SINGH, K. (1997). Effects of temperature and concentration on bovine lens alpha-crystallin secondary structure: a circular dichroism spectroscopic study. Int J Biol Macromol, 20(4), 283-291.

FARUQI, A. R. & SUBRAMANIAM, S. (2000). CCD detectors in high-resolution biological electron microscopy. Q Rev Biophys, 33(1), 1-27.

FRANK, J. (2006). Three dimensional electron microscopy of macromolecular assemblies.

FRANK, J., GAO, H., SENGUPTA, J., GAO, N. & TAYLOR, D. J. (2007). The process of mRNA-tRNA translocation. Proc Natl Acad Sci U S A, 104(50), 19671-19678.

FRANK, J., RADERMACHER, M., PENCZEK, P., ZHU, J., LI, Y., LADJADJ, M. & LEITH, A. (1996). SPIDER and WEB: processing and visualization of images in 3D electron microscopy and related fields. J Struct Biol, 116(1), 190-199.

FRANZMANN, T. M., WUHR, M., RICHTER, K., WALTER, S. & BUCHNER, J. (2005). The activation mechanism of Hsp26 does not require dissociation of the oligomer. J Mol Biol, 350(5), 1083-1093.

GERNER, E. W. & SCHNEIDER, M. J. (1975). Induced thermal resistance in HeLa cells. Nature, 256(5517), 500-502.

GHOSH, J. G., ESTRADA, M. R. & CLARK, J. I. (2005). Interactive domains for chaperone activity in the small heat shock protein, human alphaB crystallin. Biochemistry, 44(45), 14854-14869.

GHOSH, J. G., SHENOY, A. K., JR. & CLARK, J. I. (2006). N- and C-Terminal motifs in human alphaB crystallin play an important role in the recognition, selection, and solubilization of substrates. Biochemistry, 45(46), 13847-13854.

GIESE, K. C., BASHA, E., CATAGUE, B. Y. & VIERLING, E. (2005). Evidence for an essential function of the N terminus of a small heat shock protein in vivo, independent of in vitro chaperone activity. Proc Natl Acad Sci U S A, 102(52), 18896-18901.

GOLDFARB, L. G., VICART, P., GOEBEL, H. H. & DALAKAS, M. C. (2004). Desmin myopathy. Brain, 127(Pt 4), 723-734.

GRIGORIEFF, N. (2007). FREALIGN: high-resolution refinement of single particle structures. J Struct Biol, 157(1), 117-125.

GUEX, N. & PEITSCH, M. C. (1997). SWISS-MODEL and the Swiss-PdbViewer: an environment for comparative protein modeling. Electrophoresis, 18(15), 2714-2723.

HAAS, I. G. & WABL, M. (1983). Immunoglobulin heavy chain binding protein. Nature, 306(5941), 387-389.

HALEY, D. A., BOVA, M. P., HUANG, Q. L., MCHAOURAB, H. S. & STEWART, P. L. (2000). Small heat-shock protein structures reveal a continuum from symmetric to variable assemblies. Journal of Molecular Biology, 298(2), 261-272.

HALEY, D. A., HORWITZ, J. & STEWART, P. L. (1998). The small heat-shock protein, alphaB-crystallin, has a variable quaternary structure. J Mol Biol, 277(1), 27-35.

HARDING, J. (2007). Protein Glycation and Cataract: A Conformational Disease. In Protein Misfolding, Aggregation, and Conformational Diseases, pp. 499-514.

HARRIS, R. (1997). Negative Staining and Cryoelectron microscopy.

HASLBECK, M. (2002). sHsps and their role in the chaperone network. Cell Mol Life Sci, 59(10), 1649-1657.

HASLBECK, M., FRANZMANN, T., WEINFURTNER, D. & BUCHNER, J. (2005). Some like it hot: the structure and function of small heat-shock proteins. Nat Struct Mol Biol, 12(10), 842-846.

HASLBECK, M., WALKE, S., STROMER, T., EHRNSPERGER, M., WHITE, H. E., CHEN, S., SAIBIL, H. R. & BUCHNER, J. (1999). Hsp26: a temperature-regulated chaperone. Embo J, 18(23), 6744-6751.

HAWKES, P. (2007). The electron microscopes as a structure projector. Electron Tomography Second Edition, 83-111.

HENDERSON, R. (1995). The potential and limitations of neutrons, electrons and X-rays for atomic resolution microscopy of unstained biological molecules. Q Rev Biophys, 28(2), 171-193.

HORWICH, A. L. (2004). Chaperoned protein disaggregation--the ClpB ring uses its central channel. Cell, 119(5), 579-581.

HORWITZ, J. (1992). Alpha-crystallin can function as a molecular chaperone. Proc Natl Acad Sci U S A, 89(21), 10449-10453.

HORWITZ, J. (2000). The function of alpha-crystallin in vision. Semin Cell Dev Biol, 11(1), 53-60.

HORWITZ, J. (2003). Alpha-crystallin. Exp Eye Res, 76(2), 145-153.

HORWITZ, J., BOVA, M. P., DING, L. L., HALEY, D. A. & STEWART, P. L. (1999). Lens alpha-crystallin: function and structure. Eye, 13(Pt 3b), 403-408.

HSU, A. L., MURPHY, C. T. & KENYON, C. (2003). Regulation of aging and age-related disease by DAF-16 and heat-shock factor. Science, 300(5622), 1142-1145.

INGOLIA, T. D. & CRAIG, E. A. (1982). Four small Drosophila heat shock proteins are related to each other and to mammalian alpha-crystallin. Proc Natl Acad Sci U S A, 79(7), 2360-2364.

JENSEN, G. J. & BRIEGEL, A. (2007). How electron cryotomography is opening a new window onto prokaryotic ultrastructure. Curr Opin Struct Biol, 17(2), 260-267.

JIAO, W., HONG, W., LI, P., SUN, S., MA, J., QIAN, M., HU, M. & CHANG, Z. (2007). The dramatically increased chaperone activity of small heat shock protein

IbpB is retained for an extended period of time after the stress condition is removed. Biochem J.

KAPPE, G., AQUILINA, J. A., WUNDERINK, L., KAMPS, B., ROBINSON, C. V., GARATE, T., BOELENS, W. C. & DE JONG, W. W. (2004). Tsp36, a tapeworm small heat-shock protein with a duplicated alpha-crystallin domain, forms dimers and tetramers with good chaperone-like activity. Proteins, 57(1), 109-117.

KAPPE, G., FRANCK, E., VERSCHUURE, P., BOELENS, W. C., LEUNISSEN, J. A. & DE JONG, W. W. (2003). The human genome encodes 10 alpha-crystallin-related small heat shock proteins: HspB1-10. Cell Stress Chaperones, 8(1), 53-61.

KAYED, R., HEAD, E., THOMPSON, J. L., MCINTIRE, T. M., MILTON, S. C., COTMAN, C. W. & GLABE, C. G. (2003). Common structure of soluble amyloid oligomers implies common mechanism of pathogenesis. Science, 300(5618), 486-489.

KENNAWAY, C. K., BENESCH, J. L., GOHLKE, U., WANG, L., ROBINSON, C. V., ORLOVA, E. V., SAIBIL, H. R. & KEEP, N. H. (2005). Dodecameric structure of the small heat shock protein Acr1 from Mycobacterium tuberculosis. J Biol Chem, 280(39), 33419-33425.

KIERAN, D., KALMAR, B., DICK, J. R., RIDDOCH-CONTRERAS, J., BURNSTOCK, G. & GREENSMITH, L. (2004). Treatment with arimoclomol, a coinducer of heat shock proteins, delays disease progression in ALS mice. Nat Med, 10(4), 402-405.

KIM, D. R., LEE, I., HA, S. C. & KIM, K. K. (2003a). Activation mechanism of HSP16.5 from Methanococcus jannaschii. Biochem. Biophys. Res. Commun., 307(4), 991-998.

KIM, K. K., KIM, R. & KIM, S. H. (1998a). Crystal structure of a small heat-shock protein. Nature, 394(6693), 595-599.

KIM, R., KIM, K. K., YOKOTA, H. & KIM, S. H. (1998b). Small heat shock protein of Methanococcus jannaschii, a hyperthermophile. Proc Natl Acad Sci U S A, 95(16), 9129-9133.

KIM, R., LAI, L., LEE, H. H., CHEONG, G. W., KIM, K. K., WU, Z., YOKOTA, H., MARQUSEE, S. & KIM, S. H. (2003b). On the mechanism of chaperone activity of the small heat-shock protein of Methanococcus jannaschii. Proc. Natl. Acad. Sci. USA, 100(14), 8151-8155.

KOSTER, A. J., CHEN, H., SEDAT, J. W. & AGARD, D. A. (1992). Automated microscopy for electron tomography. Ultramicroscopy, 46(1-4), 207-227.

KOTEICHE, H. A., BERENGIAN, A. R. & MCHAOURAB, H. S. (1998). Identification of protein folding patterns using site-directed spin labeling. Structural characterization of a beta-sheet and putative substrate binding regions in the conserved domain of alpha A-crystallin. Biochemistry, 37(37), 12681-12688.

KOTEICHE, H. A., CHIU, S., MAJDOCH, R. L., STEWART, P. L. & MCHAOURAB, H. S. (2005). Atomic models by cryo-EM and site-directed spin labeling: application to the N-terminal region of Hsp16.5. Structure, 13(8), 1165-1171.

KOTEICHE, H. A. & MCHAOURAB, H. S. (1999). Folding pattern of the alpha-crystallin domain in alphaA-crystallin determined by site-directed spin labeling. J Mol Biol, 294(2), 561-577.

KOTEICHE, H. A. & MCHAOURAB, H. S. (2002). The determinants of the oligomeric structure in Hsp16.5 are encoded in the alpha-crystallin domain. FEBS Lett, 519(1-3), 16-22.

KOTEICHE, H. A. & MCHAOURAB, H. S. (2003). Mechanism of chaperone function in small heat-shock proteins. Phosphorylation-induced activation of two-mode binding in alphaB-crystallin. Journal of Biological Chemistry, 278(12), 10361-10367.

KOTEICHE, H. A. & MCHAOURAB, H. S. (2006). Mechanism of a hereditary cataract phenotype. Mutations in alphaA-crystallin activate substrate binding. J Biol Chem, 281(20), 14273-14279.

KUNDU, M., SEN, P. C. & DAS, K. P. (2007). Structure, stability, and chaperone function of alphaA-crystallin: role of N-terminal region. Biopolymers, 86(3), 177-192.

LASKEY, R. A., HONDA, B. M., MILLS, A. D. & FINCH, J. T. (1978). Nucleosomes are assembled by an acidic protein which binds histones and transfers them to DNA. Nature, 275(5679), 416-420.

LATCHMAN, D. S. (2005). HSP27 and cell survival in neurones. Int J Hyperthermia, 21(5), 393-402.

LEE, G. J., POKALA, N. & VIERLING, E. (1995). Structure and in vitro molecular chaperone activity of cytosolic small heat shock proteins from pea. Journal of Biological Chemistry, 270(18), 10432-10438.

LEE, G. J., ROSEMAN, A. M., SAIBIL, H. R. & VIERLING, E. (1997). A small heat shock protein stably binds heat-denatured model substrates and can maintain a substrate in a folding-competent state. Embo J, 16(3), 659-671.

LEI, J. & FRANK, J. (2005). Automated acquisition of cryo-electron micrographs for single particle reconstruction on an FEI Tecnai electron microscope. J Struct Biol, 150(1), 69-80.

LESCHZINER, A. E. & NOGALES, E. (2007). Visualizing flexibility at molecular resolution: analysis of heterogeneity in single-particle electron microscopy reconstructions. Annu Rev Biophys Biomol Struct, 36, 43-62.

LI, Y., SCHMITZ, K. R., SALERNO, J. C. & KORETZ, J. F. (2007). The role of the conserved COOH-terminal triad in alphaA-crystallin aggregation and functionality. Mol Vis, 13, 1758-1768.

LINDNER, R. A., TREWEEK, T. M. & CARVER, J. A. (2001). The molecular chaperone alpha-crystallin is in kinetic competition with aggregation to stabilize a monomeric molten-globule form of alpha-lactalbumin. Biochem J, 354(Pt 1), 79-87.

LITT, M., KRAMER, P., LAMORTICELLA, D. M., MURPHEY, W., LOVRIEN, E. W. & WELEBER, R. G. (1998). Autosomal dominant congenital cataract associated with a missense mutation in the human alpha crystallin gene CRYAA. Hum Mol Genet, 7(3), 471-474.

LIU, J. P., SCHLOSSER, R., MA, W. Y., DONG, Z., FENG, H., LUI, L., HUANG, X. Q., LIU, Y. & LI, D. W. (2004). Human alphaA- and alphaB-crystallins prevent UVA-induced apoptosis through regulation of PKCalpha, RAF/MEK/ERK and AKT signaling pathways. Exp Eye Res, 79(6), 393-403.

LIU, Y., ZHANG, X., LUO, L., WU, M., ZENG, R., CHENG, G., HU, B., LIU, B., LIANG, J. J. & SHANG, F. (2006). A novel alphaB-crystallin mutation associated with autosomal dominant congenital lamellar cataract. Invest Ophthalmol Vis Sci, 47(3), 1069-1075.

LUDTKE, S. J., BALDWIN, P. R. & CHIU, W. (1999). EMAN: semiautomated software for high-resolution single-particle reconstructions. J Struct Biol, 128(1), 82-97.

LUDTKE, S. J. & ZHOU, Z. H. (2007). 3DEM Gordon Research Conference.

MALOYAN, A., SANBE, A., OSINSKA, H., WESTFALL, M., ROBINSON, D., IMAHASHI, K., MURPHY, E. & ROBBINS, J. (2005). Mitochondrial dysfunction and apoptosis underlie the pathogenic process in alpha-B-crystallin desmin-related cardiomyopathy. Circulation, 112(22), 3451-3461.

MASTRONARDE, D. N. (2005). Automated electron microscope tomography using robust prediction of specimen movements. J Struct Biol, 152(1), 36-51.

MCDOWALL, A. W., CHANG, J. J., FREEMAN, R., LEPAULT, J., WALTER, C. A. & DUBOCHET, J. (1983). Electron microscopy of frozen hydrated sections of vitreous ice and vitrified biological samples. J Microsc, 131(Pt 1), 1-9.

MCHAOURAB, H. S., DODSON, E. K. & KOTEICHE, H. A. (2002). Mechanism of chaperone function in small heat-shock proteins. Two-mode binding of the excited states of T4 lysozyme mutants by aA-crystallin. J. Biol. Chem., 277, 40557-40566.

MCHAOURAB, H. S., KUMAR, M. S. & KOTEICHE, H. A. (2007). Specificity of alphaA-crystallin binding to destabilized mutants of betaB1-crystallin. FEBS Lett, 581(10), 1939-1943.

MCHAOURAB, H. S., LIETZOW, M. A., HIDEG, K. & HUBBELL, W. L. (1996). Motion of spin-labeled side chains in T4 lysozyme. Correlation with protein structure and dynamics. Biochemistry, 35(24), 7692-7704.

MEHLEN, P., KRETZ-REMY, C., PREVILLE, X. & ARRIGO, A. P. (1996). Human hsp27, Drosophila hsp27 and human alphaB-crystallin expression-mediated increase in glutathione is essential for the protective activity of these proteins against TNFalpha-induced cell death. Embo J, 15(11), 2695-2706.

MERCK, K. B., DE HAARD-HOEKMAN, W. A., OUDE ESSINK, B. B., BLOEMENDAL, H. & DE JONG, W. W. (1992). Expression and aggregation of recombinant alpha A-crystallin and its two domains. Biochim Biophys Acta, 1130(3), 267-276.

MINDELL, J. A. & GRIGORIEFF, N. (2003). Accurate determination of local defocus and specimen tilt in electron microscopy. J. Struct. Biol., 142(3), 334-347.

MITRA, K. & FRANK, J. (2006). Ribosome dynamics: insights from atomic structure modeling into cryo-electron microscopy maps. Annu Rev Biophys Biomol Struct, 35, 299-317.

MOYANO, J. V., EVANS, J. R., CHEN, F., LU, M., WERNER, M. E., YEHIELY, F., DIAZ, L. K., TURBIN, D., KARACA, G., WILEY, E., NIELSEN, T. O., PEROU,

C. M. & CRYNS, V. L. (2006). AlphaB-crystallin is a novel oncoprotein that predicts poor clinical outcome in breast cancer. J Clin Invest, 116(1), 261-270.

NAKAMOTO, H. & VIGH, L. (2007). The small heat shock proteins and their clients. Cell Mol Life Sci, 64(3), 294-306.

NARBERHAUS, F. (2002). Alpha-crystallin-type heat shock proteins: socializing minichaperones in the context of a multichaperone network. Microbiol Mol Biol Rev, 66(1), 64-93; table of contents.

OHI, M., LI, Y., CHENG, Y. & WALZ, T. (2004). Negative Staining and Image Classification - Powerful Tools in Modern Electron Microscopy. Biol Proced Online, 6, 23-34.

PARSELL, D. A. & LINDQUIST, S. (1993). The function of heat-shock proteins in stress tolerance: degradation and reactivation of damaged proteins. Annu. Rev. Genet., 27, 437-496.

PASTA, S. Y., RAMAN, B., RAMAKRISHNA, T. & RAO CH, M. (2003). Role of the conserved SRLFDQFFG region of alpha-crystallin, a small heat shock protein. Effect on oligomeric size, subunit exchange, and chaperone-like activity. J Biol Chem, 278(51), 51159-51166.

PETTERSEN, E. F., GODDARD, T. D., HUANG, C. C., COUCH, G. S., GREENBLATT, D. M., MENG, E. C. & FERRIN, T. E. (2004). UCSF Chimera--a visualization system for exploratory research and analysis. J. Comput. Chem., 25(13), 1605-1612.

PULOKAS, J., GREEN, C., KISSEBERTH, N., POTTER, C. S. & CARRAGHER, B. (1999). Improving the positional accuracy of the goniometer on the Philips CM series TEM. J Struct Biol, 128(3), 250-256.

QUINLAN, R. (2002). Cytoskeletal competence requires protein chaperones. Prog Mol Subcell Biol, 28, 219-233.

RABENSTEIN, M. D. & SHIN, Y. K. (1995). Determination of the distance between two spin labels attached to a macromolecule. Proceedings of the National Academy of Sciences of the United States of America., 92(18), 8239-8243.

RADFORD, S. E. (2006). GroEL: More than Just a folding cage. Cell, 125(5), 831-833.

RAJASEKARAN, N. S., CONNELL, P., CHRISTIANS, E. S., YAN, L. J., TAYLOR, R. P., OROSZ, A., ZHANG, X. Q., STEVENSON, T. J., PESHOCK, R. M., LEOPOLD, J. A., BARRY, W. H., LOSCALZO, J., ODELBERG, S. J. &

BENJAMIN, I. J. (2007). Human alpha B-crystallin mutation causes oxido-reductive stress and protein aggregation cardiomyopathy in mice. Cell, 130(3), 427-439.

RAMAN, B. & RAO, C. M. (1997). Chaperone-like activity and temperature-induced structural changes of alpha-crystallin. J Biol Chem, 272(38), 23559-23564.

REDDY, G. B., KUMAR, P. A. & KUMAR, M. S. (2006). Chaperone-like activity and hydrophobicity of alpha-crystallin. IUBMB Life, 58(11), 632-641.

RITOSSA, F. M. (1964). Experimental Activation of Specific Loci in Polytene Chromosomes of Drosophila. Exp Cell Res, 35, 601-607.

RITOSSA, F. M. & VONBORSTEL, R. C. (1964). Chromosome Puffs in Drosophila Induced by Ribonuclease. Science, 145, 513-514.

RUSKA, E. (1986). The development of electron microscope and electon microscopy. In Nobel Lecture.

SABAN, S. D., SILVESTRY, M., NEMEROW, G. R. & STEWART, P. L. (2006). Visualization of alpha-helices in a 6-angstrom resolution cryoelectron microscopy structure of adenovirus allows refinement of capsid protein assignments. J Virol, 80(24), 12049-12059.

SANDER, B., GOLAS, M. M. & STARK, H. (2005). Advantages of CCD detectors for de novo three-dimensional structure determination in single-particle electron microscopy. J Struct Biol, 151(1), 92-105.

SATHISH, H. A., KOTEICHE, H. A. & MCHAOURAB, H. S. (2004). Binding of destabilized betaB2-crystallin mutants to alpha-crystallin: the role of a folding intermediate. J Biol Chem, 279(16), 16425-16432.

SATHISH, H. A., STEIN, R. A., YANG, G. & MCHAOURAB, H. S. (2003). Mechanism of chaperone function in small heat-shock proteins. Fluorescence studies of the conformations of T4 lysozyme bound to alphaB-crystallin. Journal of Biological Chemistry, 278(45), 44214-44221.

SCHAFFITZEL, C., OSWALD, M., BERGER, I., ISHIKAWA, T., ABRAHAMS, J. P., KOERTEN, H. K., KONING, R. I. & BAN, N. (2006). Structure of the E. coli signal recognition particle bound to a translating ribosome. Nature, 444(7118), 503-506.

SHARMA, K. K., KAUR, H., KUMAR, G. S. & KESTER, K. (1998a). Interaction of 1,1'-bi(4-anilino)naphthalene-5,5'-disulfonic acid with alpha-crystallin. J Biol Chem, 273(15), 8965-8970.

SHARMA, K. K., KUMAR, G. S., MURPHY, A. S. & KESTER, K. (1998b). Identification of 1,1'-bi(4-anilino)naphthalene-5,5'-disulfonic acid binding sequences in alpha-crystallin. J Biol Chem, 273(25), 15474-15478.

SHASHIDHARAMURTHY, R., KOTEICHE, H. A., DONG, J. & MCHAOURAB, H. S. (2005). Mechanism of chaperone function in small heat shock proteins: dissociation of the HSP27 oligomer is required for recognition and binding of destabilized T4 lysozyme. J Biol Chem, 280(7), 5281-5289.

SHERMAN, M. B., BRINK, J. & CHIU, W. (1996). Performance of a slow-scan CCD camera for macromolecular imaging in a 400 kV electron cryomicroscope. Micron, 27(2), 129-139.

SHI, J., KOTEICHE, H. A., MCHAOURAB, H. S. & STEWART, P. L. (2006). Cryoelectron microscopy and EPR analysis of engineered symmetric and polydisperse Hsp16.5 assemblies reveals determinants of polydispersity and substrate binding. J Biol Chem, 281(52), 40420-40428.

SHROFF, N. P., CHERIAN-SHAW, M., BERA, S. & ABRAHAM, E. C. (2000). Mutation of R116C results in highly oligomerized alpha A-crystallin with modified structure and defective chaperone-like function. Biochemistry, 39(6), 1420-1426.

SINGH, D., RAMAN, B., RAMAKRISHNA, T. & RAO CH, M. (2006). The cataract-causing mutation G98R in human alphaA-crystallin leads to folding defects and loss of chaperone activity. Mol Vis, 12, 1372-1379.

SINGH, R. J., FEIX, J. B., MCHAOURAB, H. S., HOGG, N. & KALYANARAMAN, B. (1995). Spin-labeling study of the oxidative damage to low-density lipoprotein. Arch Biochem Biophys, 320(1), 155-161.

SINGH, R. J., HOGG, N., MCHAOURAB, H. S. & KALYANARAMAN, B. (1994). Physical and chemical interactions between nitric oxide and nitroxides. Biochim Biophys Acta, 1201(3), 437-441.

STAGG, S. M., LANDER, G. C., PULOKAS, J., FELLMANN, D., CHENG, A., QUISPE, J. D., MALLICK, S. P., AVILA, R. M., CARRAGHER, B. & POTTER, C. S. (2006). Automated cryoEM data acquisition and analysis of 284742 particles of GroEL. J Struct Biol, 155(3), 470-481.

STAMLER, R., KAPPE, G., BOELENS, W. & SLINGSBY, C. (2005). Wrapping the alpha-crystallin domain fold in a chaperone assembly. J Mol Biol, 353(1), 68-79.

STEWART, P. L., CHIU, C. Y., HALEY, D. A., KONG, L. B. & SCHLESSMAN, J. L. (1999). Review: resolution issues in single-particle reconstruction. J Struct Biol, 128(1), 58-64.

STROMER, T., FISCHER, E., RICHTER, K., HASLBECK, M. & BUCHNER, J. (2004). Analysis of the regulation of the molecular chaperone Hsp26 by temperature-induced dissociation: the N-terminal domail is important for oligomer assembly and the binding of unfolding proteins. J Biol Chem, 279(12), 11222-11228.

STUDER, S., OBRIST, M., LENTZE, N. & NARBERHAUS, F. (2002). A critical motif for oligomerization and chaperone activity of bacterial alpha-heat shock proteins. Eur J Biochem, 269(14), 3578-3586.

SULOWAY, C., PULOKAS, J., FELLMANN, D., CHENG, A., GUERRA, F., QUISPE, J., STAGG, S., POTTER, C. S. & CARRAGHER, B. (2005). Automated molecular microscopy: the new Leginon system. J Struct Biol, 151(1), 41-60.

SUN, Y. & MACRAE, T. H. (2005a). The small heat shock proteins and their role in human disease. Febs J, 272(11), 2613-2627.

SUN, Y. & MACRAE, T. H. (2005b). Small heat shock proteins: molecular structure and chaperone function. Cell Mol Life Sci, 62(21), 2460-2476.

TABNER, B. J., EL-AGNAF, O. M., GERMAN, M. J., FULLWOOD, N. J. & ALLSOP, D. (2005). Protein aggregation, metals and oxidative stress in neurodegenerative diseases. Biochem Soc Trans, 33(Pt 5), 1082-1086.

TANG, Y. C., CHANG, H. C., ROEBEN, A., WISCHNEWSKI, D., WISCHNEWSKI, N., KERNER, M. J., HARTL, F. U. & HAYER-HARTL, M. (2006). Structural features of the GroEL-GroES nano-cage required for rapid folding of encapsulated protein. Cell, 125(5), 903-914.

THAMPI, P. & ABRAHAM, E. C. (2003). Influence of the C-terminal residues on oligomerization of alpha A-crystallin. Biochemistry, 42(40), 11857-11863.

THAMPI, P., HASSAN, A., SMITH, J. B. & ABRAHAM, E. C. (2002). Enhanced C-terminal truncation of alphaA- and alphaB-crystallins in diabetic lenses. Invest Ophthalmol Vis Sci, 43(10), 3265-3272.

TISSIERES, A., MITCHELL, H. K. & TRACY, U. M. (1974). Protein synthesis in salivary glands of Drosophila melanogaster: relation to chromosome puffs. J Mol Biol, 84(3), 389-398.

TREWEEK, T. M., REKAS, A., LINDNER, R. A., WALKER, M. J., AQUILINA, J. A., ROBINSON, C. V., HORWITZ, J., PERNG, M. D., QUINLAN, R. A. & CARVER, J. A. (2005). R120G alphaB-crystallin promotes the unfolding of reduced alpha-lactalbumin and is inherently unstable. Febs J, 272(3), 711-724.

TRUSCOTT, R. (2007). Eye Lens Proteins and Cataracts. In Protein Misfolding, Aggregation, and Conformational Diseases, pp. 435-447.

VAN DE KLUNDERT, F. A. & DE JONG, W. W. (1999). The small heat shock proteins Hsp20 and alphaB-crystallin in cultured cardiac myocytes: differences in cellular localization and solubilization after heat stress. European Journal of Cell Biology, 78(8), 567-572.

VAN DE KLUNDERT, F. A., GIJSEN, M. L., VAN DEN, I. P. R., SNOECKX, L. H. & DE JONG, W. W. (1998). αB-crystallin and hsp25 in neonatal cardiac cells--differences in cellular localization under stress conditions. European Journal of Cell Biology, 75(1), 38-45.

VAN HEEL, M. (1987). Angular reconstitution: a posteriori assignment of projection directions for 3D reconstruction. Ultramicroscopy, 21(2), 111-123.

VAN HEEL, M., GOWEN, B., MATADEEN, R., ORLOVA, E. V., FINN, R., PAPE, T., COHEN, D., STARK, H., SCHMIDT, R., SCHATZ, M. & PATWARDHAN, A. (2000). Single-particle electron cryo-microscopy: towards atomic resolution. Q Rev Biophys, 33(4), 307-369.

VAN HEEL, M., HARAUZ, G., ORLOVA, E. V., SCHMIDT, R. & SCHATZ, M. (1996). A new generation of the IMAGIC image processing system. J Struct Biol, 116(1), 17-24.

VAN HEEL, M. & SCHATZ, M. (2005). Fourier shell correlation threshold criteria. J Struct Biol, 151(3), 250-262.

VAN MONTFORT, R., SLINGSBY, C. & VIERLING, E. (2001a). Structure and function of the small heat shock protein/alpha-crystallin family of molecular chaperones. Adv Protein Chem, 59, 105-156.

VAN MONTFORT, R. L., BASHA, E., FRIEDRICH, K. L., SLINGSBY, C. & VIERLING, E. (2001b). Crystal structure and assembly of a eukaryotic small heat shock protein. Nat Struct Biol, 8(12), 1025-1030.

VICART, P., CARON, A., GUICHENEY, P., LI, Z., PREVOST, M. C., FAURE, A., CHATEAU, D., CHAPON, F., TOME, F., DUPRET, J. M., PAULIN, D. & FARDEAU, M. (1998). A missense mutation in the alphaB-crystallin chaperone gene causes a desmin-related myopathy. Nat Genet, 20(1), 92-95.

WADE, R. H. (1992). A brief look at imaging and contrast transfer. Ultramicroscopy, 46(1-4), 145-156.

WHITE, H. E., ORLOVA, E. V., CHEN, S., WANG, L., IGNATIOU, A., GOWEN, B., STROMER, T., FRANZMANN, T. M., HASLBECK, M., BUCHNER, J. & SAIBIL, H. R. (2006). Multiple distinct assemblies reveal conformational flexibility in the small heat shock protein Hsp26. Structure, 14(7), 1197-1204.

WILLIAMS, D., LEE, K., SHI, J., CHEN, D. & STEWART, P. (2007). Sub-nanometer structure of DNA-PK catalytic subunit by single particle cryo-EM. (Manuscript in preparation).

XU, Z. & SIGLER, P. B. (1998). GroEL/GroES: structure and function of a two-stroke folding machine. J. Struct. Biol., 124(2-3), 129-141.

YONEKURA, K., MAKI-YONEKURA, S. & NAMBA, K. (2003). Complete atomic model of the bacterial flagellar filament by electron cryomicroscopy. Nature, 424(6949), 643-650.

YOUNG, J. C., AGASHE, V. R., SIEGERS, K. & HARTL, F. U. (2004). Pathways of chaperone-mediated protein folding in the cytosol. Nat Rev Mol Cell Biol, 5(10), 781-791.

ZHANG, P., BEATTY, A., MILNE, J. L. & SUBRAMANIAM, S. (2001). Automated data collection with a Tecnai 12 electron microscope: applications for molecular imaging by cryomicroscopy. J Struct Biol, 135(3), 251-261.

ZHENG, S. Q., KOLLMAN, J. M., BRAUNFELD, M. B., SEDAT, J. W. & AGARD, D. A. (2007). Automated acquisition of electron microscopic random conical tilt sets. J Struct Biol, 157(1), 148-155.

ZHOU, Z. H. & CHIU, W. (2003). Determination of icosahedral virus structures by electron cryomicroscopy at subnanometer resolution. Adv Protein Chem, 64, 93-124.

ZIESE, U., JANSSEN, A. H., MURK, J. L., GEERTS, W. J., VAN DER KRIFT, T., VERKLEIJ, A. J. & KOSTER, A. J. (2002). Automated high-throughput electron tomography by pre-calibration of image shifts. J Microsc, 205(Pt 2), 187-200.